University of Miami
Scholarly Repository

2014-07-30

Fluorescence Photoactivation Based on 2-Nitrobenzyl Derivatives

Subramani Swaminathan

University of Miami, dream0709subu@gmail.com

Follow this and additional works at: https://scholarlyrepository.miami.edu/oa_dissertations

UNIVERSITY OF MIAMI

FLUORESCENCE PHOTOACTIVATION BASED ON 2-NITROBENZYL
DERIVATIVES

By

Subramani Swaminathan

A DISSERTATION

Submitted to the Faculty
of the University of Miami
in partial fulfillment of the requirements for
the degree of Doctor of Philosophy

Coral Gables, Florida

August 2014

UNIVERSITY OF MIAMI

A dissertation submitted in partial fulfillment of
the requirements for the degree of
Doctor of Philosophy

FLUORESCENCE PHOTOACTIVATION BASED ON 2-NITROBENZYL
DERIVATIVES

Subramani Swaminathan

Approved:

_____
Françisco M. Raymo, Ph.D.
Professor of Chemistry

_____
James N. Wilson, Ph.D.
Professor of Chemistry

_____
Roger M. Leblanc, Ph.D.
Professor of Chemistry

_____
M. Brian Blake, Ph.D.
Dean of the Graduate School

_____
James D. Baker, Ph.D.
Professor of Biology

SWAMINATHAN, SUBRAMANI   (Ph.D., Chemistry)

<u>Fluorescence Photoactivation Based on 2-Nitrobenzyl Derivatives</u>   (August 2014)

Abstract of a dissertation at the University of Miami.

Dissertation supervised by Professor Françisco M. Raymo.

No. of pages in text (122)

Fluorescence microscopy offers a non-invasive way to image biological species in real time. The phenomenon of diffraction, however, restricts the resolution of the conventional fluorescent microscopes to submicrometer dimensions in both the horizontal and vertical directions. This limitation can be overcome with the aid of photoactivatable fluorophores. Photoactivatable fluorophores switch from a nonemissive state to an emissive one under irradiation at an activation wavelength and then emit light in form of fluorescence upon illumination at an excitation wavelength. Such a concatenation of activation and excitation events translates into the possibility to switch fluorescence on within a defined region of space at a given interval of time. In turn, the spatiotemporal control of fluorescence offers the opportunity to monitor dynamic processes in real time as well as to reconstruct images with resolution at the nanometer level. As a result, these photoresponsive molecular switches are becoming invaluable analytical tools to probe the structures and dynamics of a diversity of materials relying on the noninvasive character of fluorescence imaging. In this context, I explored ways to photoactivate fluorescence based on 2-nitrobenzyl derivatives. To begin with, fluorescence photoactivation of a coumarin fluorophore with the aid of an appended halochromic auxochrome was designed and its photophysical and photochemical

properties were investigated in organic and aqueous environments. Using this strategy, we were able to activate fluorescence in liquid solutions, within rigid matrices and inside micellar assemblies. Furthermore, it is possible to imprint fluorescent patterns on polymer films, to monitor proton diffusion within such materials in real time on a millisecond timescale and acquire images with spatial resolution at the nanometer level. Besides, a mechanism was devised to open the ring of an oxazine auxochrome irreversibly under the influence of light acting on the 2-nitrobenzyl group. The photochemical and electrochemical properties of this compound were also explored. To improve the brightness of the photoactivatable probes employed to obtain super-resolution images, strategies for fluorescence activation of borondipyrromethene (BODIPY) chromophores were explored. In addition, a protocol was designed to study the guest exchange between dynamic supramolecular assemblies inside cells.

To my family and friends

ACKNOWLEDGEMENTS

TABLE OF CONTENTS

CHAPTER 7

INTRACELLULAR GUEST EXCHANGE BETWEEN DYNAMIC SUPRAMOLECULAR HOSTS

CHAPTER 8

EXPERIMENTAL PROCEDURES

LIST OF FIGURES

540–640 nm. Image *c* was recorded with two-photon excitation at 720 nm and detection at 420–450 nm. Image *d* is an overlay of images *b* and *c*   95

Figure 7.14. Brightfield (*a*) and fluorescence (*b–d*) images of HeLa cells recorded after incubation with a PBS dispersions of nanoparticles of **10** (125 µg mL^{-1}), loaded with **26** (1.25 µg mL^{-1}), for 3 hours, addition of indocyanine green (50 µM) 30 min prior to termination of incubation and washing. Image *b* was acquired with excitation at 458 nm and detection at 540–640 nm. Image *c* was recorded with excitation at 628 nm and detection at 780–800 nm. Image *d* is an overlay of images *b* and *c*   95

Figure 7.15. Brightfield (*a*) and fluorescence (*b–d*) images of HeLa cells recorded after incubation with a PBS dispersions of nanoparticles of **10** (125 µg mL^{-1}), loaded with **23** (1.25 µg mL^{-1}), for 3 hours, addition of indocyanine green (50 µM) 30 min prior to termination of incubation and washing. Image *b* was acquired with excitation at 458 nm and detection at 540–640 nm. Image *c* was recorded with excitation at 628 nm and detection at 780–800 nm. Image *d* is an overlay of images *b* and *c*   95

Figure 7.16. Brightfield (*a*) and fluorescence (*b–d*) images of HeLa cells recorded after incubation with a mixture (1:1, v/v) of two PBS dispersions of nanoparticles of **10** (125 µg mL^{-1}), loaded with **26** (1.25 µg mL^{-1}) and **23** (1.25 µg mL^{-1}) respectively, for 3 hours, addition of indocyanine green (50 µM) 30 min prior to termination of incubation and washing. Image *b* was acquired with excitation at 458 nm and detection at 540–640 nm. Image *c* was recorded with excitation at 628 nm and detection at 780–800 nm. Image *d* is an overlay of images *b* and *c*   96

LIST OF TABLES

CHAPTER 1

PHOTOACTIVATABLE FLUOROPHORES

1.1. Introduction

Organic chromophores can be designed to switch from a nonemissive state to an emissive one (Figure 1.1) under optical control with the aid of chemical synthesis.[1-7] Such photoresponsive molecular systems permit the activation of fluorescence within a defined region of space at a given interval of time. Indeed, significant emission occurs only after illumination of the initial species at an activating wavelength (λ_{Ac}) and irradiation of the photogenerated one at an exciting wavelength (λ_{Ex}). In turn, the interplay of activating and exciting beams translates into a spatiotemporal control of fluorescence that is otherwise impossible with conventional fluorophores. This unique behavior offers the opportunity to monitor dynamic processes in real time. In fact, the diffusion of biomolecular systems labeled with photoactivatable fluorophores as well as the flow of liquids containing these switchable probes, can be monitored in real time with the aid of a microscope and a pair of lasers operating at λ_{Ac} and λ_{Ex}.[1,2,8-13] In both instances, a pulse at λ_{Ac} can induce the photochemical transformation responsible for fluorescence activation at a given interval of time in a specific location in space, while continuous illumination at λ_{Ex} can probe the spatial redistribution of fluorescence in time. Quantitative information on molecular diffusion in biological specimens and flow dynamics in microstructured channels can then be extracted from the analysis of the collected data. Similarly, the interplay of space and time, associated with fluorescence photoactivation, can be exploited to overcome the limitations that diffraction imposes on the resolution of conventional fluorescence microscopes.[14-21] Specifically, closely-spaced photoactivatable

fluorophores can be resolved in time by activating sequentially their emission. In particular, multiple iterations of illumination steps at λ_{Ac} and λ_{Ex} permit the stochastic activation of distinct subpopulations of probes at different intervals of time and the localization of the activated emitters at the single-molecule level respectively. The spatial coordinates of the probes localized sequentially can then be compiled into a single map to reconstruct an image of the sample with resolution at the nanometer level.
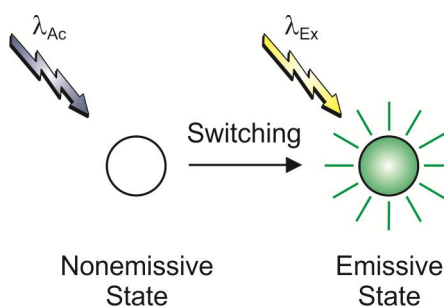
Figure 1.1. Photoactivatable fluorophores switch from a nonemissive to an emissive state upon illumination at an activating wavelength (λ_{Ac}) and then emit light in the form of fluorescence under irradiation at an exciting wavelength (λ_{Ex}).

The imaging strategies possible on the basis of fluorescence photoactivation can be implemented with appropriate fluorescent proteins[22-25] or specific synthetic dyes.[3,5-7,26,27] Both can be engineered to switch either irreversibly or reversibly between distinct states in response to λ_{Ac} and then emit light upon illumination at λ_{Ex}. The physical dimensions of the former probes are significantly larger than those of the latter ones and prevent high labeling densities. Nonetheless, fluorescent proteins can conveniently be introduced into biological samples relying on genetic encoding. Instead, synthetic dyes require labeling protocols based on tedious covalent modifications, often in combination with supramolecular association, but can be introduced in a diversity of materials other than biological preparations. In fact, both families of photoactivatable probes are very much

complementary and the choice of one versus the other is generally dictated by the nature of the sample under investigation. A significant advantage of synthetic probes over their biomolecular counterparts, however, lies in the power of chemical synthesis to deliver molecules with engineered properties. Subtle structural manipulations can be invoked to tailor their dimensions, polarity, shapes and spectroscopic response. Thus, synthetic fluorophores with better photochemical and photophysical properties than natural ones can, in principle, be accessed with appropriate synthetic strategies. This chapter highlights the main mechanisms developed so far to activate the emission of synthetic dyes, illustrates representative examples of structural designs for fluorescence photoactivation and discusses their promising applications in fluorescence imaging.

1.2. Activation Mechanisms

The electronic transition responsible for the fluorescence of most organic chromophores originates from the first singlet excited state (S_1) to produce the corresponding singlet ground state (S_0).[28] This radiative photophysical process can be suppressed either by preventing the population of S_1 altogether or by promoting competitive nonradiative pathways. In fact, the nonemissive state of a photoactivatable fluorophore can be designed around either one of these two strategies. In the first instance, the switching process responsible for activation must be engineered to enable excitation (*a* in Figure 1.2). Specifically, the molar extinction coefficient at λ_{Ex} must be negligible before switching and become significant only after the photochemical transformation. This requirement is generally satisfied by imposing a decrease on the energy gap between S_1 and S_0 with switching. Under these conditions, the $S_0 \rightarrow S_1$ absorption shifts bathochromically with switching and an appropriate λ_{Ex} can be selected to excite

exclusively the photochemical product with concomitant emission. In the second instance, the switching process responsible for activation must be designed to suppress the nonradiative deactivation of S_1 in favor of its radiative decay to S_0 (**b** in Figure 1.2). In particular, the fluorescence quantum yield must be negligible before switching and become significant only after the photochemical transformation. This requirement is generally satisfied by ensuring the physical separation of a quencher from the emissive chromophore with switching. Under these conditions, the quenching pathway responsible for the nonradiative deactivation of S_1 is prevented with concomitant emission. Thus, both switching mechanisms eventually translate into fluorescence activation. Indeed, they have both been adapted successfully to activate the emission of several members of many families of synthetic dyes, including borondipyrromethenes,[29] coumarins,[30-34] diarylethenes,[35,36] dihydrofurans,[37] fluoresceins,[38-45] rhodamines[46-49] and spiropyrans.[50]
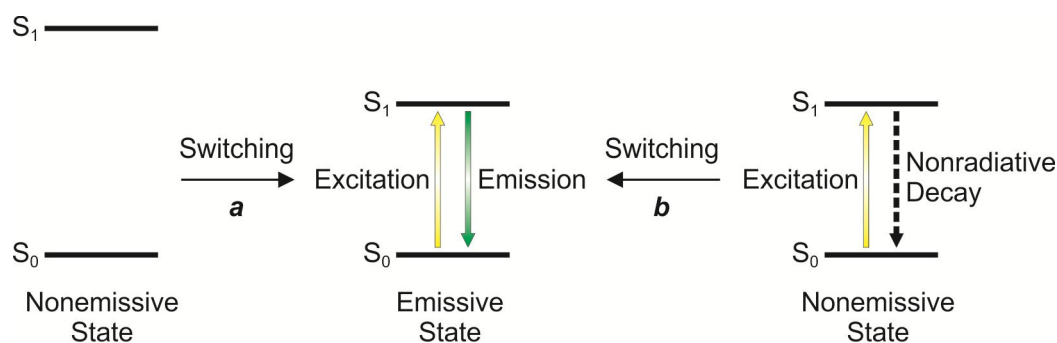
Figure 1.2. The transformation responsible for switching the nonemissive form of a photoactivatable fluorophore into the emissive one can be designed to (**a**) narrow the energy gap between the first singlet excited state (S_1) and the singlet ground state (S_0) to permit the exclusive excitation of the product or (**b**) suppress the nonradiative deactivation of S_1 to allow the radiative generation of S_0.

Table 1.1 Photochemical and photophysical parameters[a] associated with representative examples of photoactivatable fluorophores.

	$^a\lambda_{Ab}$ (nm)	$^a\varepsilon$ (mM^{-1} cm^{-1})	λ_{Ac} (nm)	ϕ_{Ac} (10^{-3})	$^b\lambda_{Ab}$ (nm)	$^b\varepsilon$ (mM^{-1} cm^{-1})	λ_{Ex} (nm)	λ_{Em} (nm)	ϕ_{Em} (10^{-2})
1	424	29	407	5.9	570	54	594	613	2.5
2	526	—	350	8.9	522	—	—	539	66
3	336	17	313	420	456	46	456	550	87
4	412	36	355	20	570	83	532	650	9

[a]The absorption wavelength ($^a\lambda_{Ab}$), molar extinction coefficient ($^a\varepsilon$) and activation quantum yield (ϕ_{Ac}) of the nonemissive state as well as the absorption wavelength ($^b\lambda_{Ab}$), molar extinction coefficient ($^b\varepsilon$), emission wavelength (λ_{Em}) and emission quantum yield (ϕ_{Em}) of the emissive state were measured in EtOH for **1**, PBS for **2**, 1,4-dioxane for **3** and MeCN for **4**.

Compounds **1a** and **2a** (Figure 1.3) are representative examples of photoactivatable fluorophores designed around the two activation mechanisms highlighted in Figure 1.2. The absorption spectrum of **1a** shows a band centered at a wavelength ($^a\lambda_{Ab}$ in Table 1.1) of 424 nm in ethanol.[37a,b,d] Upon illumination at a λ_{Ac} positioned within this band, **1a** releases molecular nitrogen to form a nitrene intermediate. This reactive species then generates a mixture of compounds, including **1b**. The activation quantum yield (ϕ_{Ac} in Table 1.1) for the photochemical conversion of **1a** into **1b** is 5.9×10^{-3} under these conditions. The transformation of the electron-withdrawing azide substituent of **1a** into the electron donating primary amine of **1b** shifts the absorption band of the dihydrofuran chromophore to a wavelength ($^b\lambda_{Ab}$ in Table 1.1) of 570 nm. As a result, irradiation at a λ_{Ex} positioned within the shifted absorption band excites selectively **1b** and produces an emission band at a wavelength (λ_{Em} in Table 1.1) of 613 nm in the corresponding spectrum with an emission quantum yield (ϕ_{Em} in Table 1.1) of 2.5×10^{-2}. Thus, the photoinduced decrease in the energy gap separating S_1 and S_0 (***a*** in Figure 1.2) is responsible for fluorescence activation in this switchable system.

The three carboxylate groups of **2a** ensure optimal solubility in phosphate buffer saline (PBS).[29] Under these conditions, the absorption spectrum of this compound shows a band at a $^a\lambda_{Ab}$ of 526 nm for the borondipyrromethene (BODIPY) chromophore. Excitation at a λ_{Ex} positioned within this band, however, translates into negligible emission. Indeed, the transfer of an electron from the excited BODIPY to the adjacent 2,6-dinitrobenzyl appendage provides an efficient pathway for nonradiative deactivation and suppresses fluorescence effectively. Illumination at a λ_{Ac} of 350 nm cleaves the 2,6-dinitrobenzyl quencher away from the BODIPY chromophore to generate **2b** with a ϕ_{Ac} of 8.9×10^{-3}. This photochemical transformation has negligible influence on the BODIPY absorption, but a dramatic effect on its emissive behavior. Specifically, the absorption band of **2b** is centered at a $^b\lambda_{Ab}$ of 522 nm and excitation at a λ_{Ex} positioned within this absorption produces an intense emission band at a λ_{Em} of 539 nm in the corresponding spectrum with a ϕ_{Em} of *ca.* 0.7. Thus, the photoinduced separation of a quencher from an emissive chromophore prevents the nonradiative deactivation of the latter (***b*** in Figure 1.2) and is responsible for fluorescence activation in this switchable system.

The photochemical reactions responsible for the switching of **1a** to **1b** and of **2a** to **2b** are both irreversible. As a result, the photogenerated states of both systems cannot revert back to the original ones. In fact, the emission of photoactivatable fluorophores, based on irreversible transformations, cannot be switched off, unless the emissive state is permanently bleached. Specifically, prolonged illumination at λ_{Ex} after activation, to promote the degradation of the emissive state, is the only viable mechanism to suppress the fluorescence of these systems. Alternatively, the inherent reversibility of

photochromic transformations[51-59] can be exploited to photoactivate fluorescence reversibly. Indeed, one of the two interconvertible states of many photochromic compounds is often fluorescent.[60] Therefore, the photoinduced and reversible conversion of one state into the other translates into fluorescence switching. Nonetheless, the quantum yields of these emissive processes tend to be significantly lower than those associated with the main families of synthetic fluorophores. The diarylethene **3a** (Figure 1.4) is one of the few remarkable exceptions to this general trend.[36] Its absorption spectrum shows a band centered at a $^a\lambda_{Ab}$ of 336 nm in 1,4-dioxane. Upon illumination at a λ_{Ac} positioned within this band, **3a** switches to **3b** with a ϕ_{Ac} of 0.42. This structural transformation brings the two halves of the molecule in conjugation and shifts bathochromically the $S_0 \rightarrow S_1$ absorption to a $^b\lambda_{Ab}$ of 456 nm. As a result, irradiation at a λ_{Ex} positioned within this band excites **3b** selectively and is accompanied by the appearance of a band a λ_{Em} of 550 nm in the corresponding emission spectrum. Thus, the mechanism responsible for fluorescence activation involves, once again, a photoinduced decrease in the energy gap between S_1 and S_0 (*a* in Figure 1.2). Remarkably, ϕ_{Em} approaches a value of 0.9 in this instance and is significantly greater than those of the dihydrofuran **1b** and BODIPY **2b** (Table 1.1). However, the excitation of **3b** is also accompanied by the photochemical regeneration of **3a** with a quantum efficiency of 4×10^{-4}. Thus, the fluorescence of this particular system can be activated and then deactivated for multiple cycles relying exclusively on optical control.
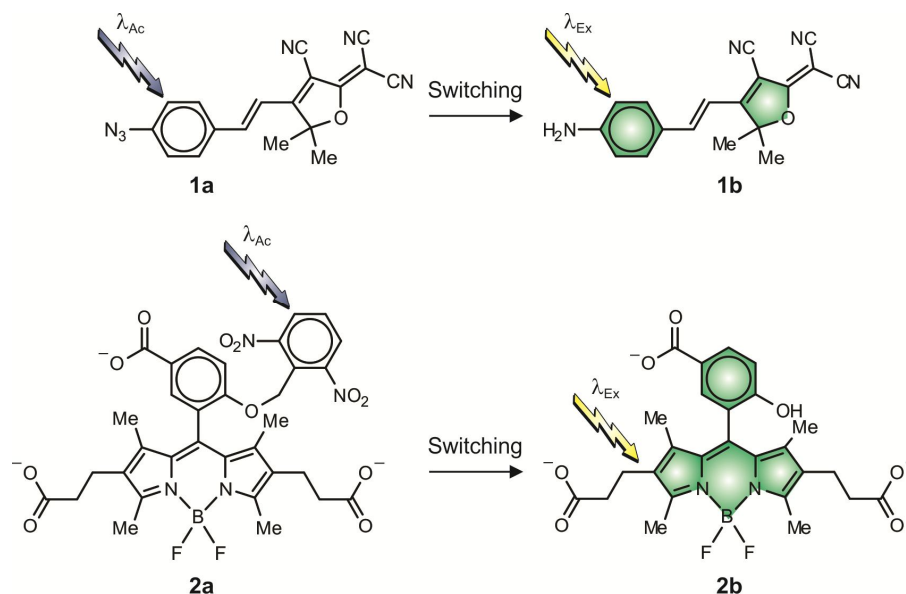
Figure 1.3. The photoinduced conversion of **1a** into **1b** shifts the $S_0 \rightarrow S_1$ absorption of the dihydrofuran chromophore bathochromically and permits the selective excitation of the product with concomitant emission. The photochemical transformation of **2a** into **2b** separates the 2,6-dinitrobenzyl quencher from the borondipyrromethene chromophore and permits the radiative deactivation of the latter upon excitation
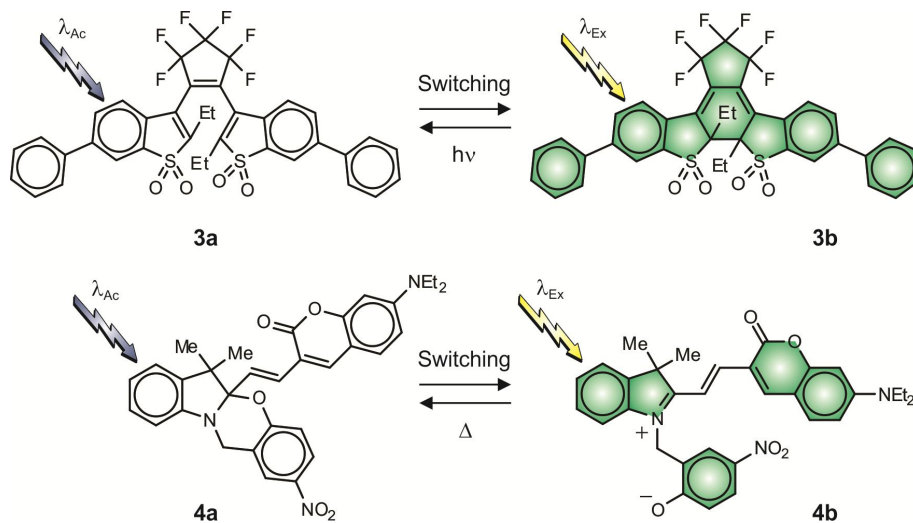
Figure 1.4. The photoinduced transformations of **3a** into **3b** and of **4a** into **4b** shift the corresponding $S_0 \rightarrow S_1$ absorptions bathochromically and permit the selective excitation of the products with concomitant emission. Both switching processes are reversible and the initial nonemissive states are regenerated after photoinduced, in one instance, and thermal, in the other, re-isomerizations.

Photochromic compounds can also be employed in combination with complementary emissive chromophores to photoswitch fluorescence.[61-63] Generally, fluorescent and photochromic components are integrated within the same molecular skeleton or supramolecular construct. The photoinduced and reversible interconversion of the latter can then be employed to control the emission of the former. Specifically, only one of the two interconvertible states of the photochromic component is designed to quench the excited state of the fluorescent component on the basis of electron or energy transfer processes. Under these conditions, the emissive chromophore deactivates nonradiatively, when the switchable component is in the quenching state, and radiatively, in the other instance. These operating principles are reminiscent of the mechanism (*b* in Figure 1.2) governing the behavior of **2a**, but they are mostly employed to deactivate, rather than activate, fluorescence. Indeed, the initial state of the interconvertible system is generally the emissive one and fluorescence turns off after photoinduced switching.

In alternative to controlling the excitation dynamics of the fluorescent component with the photochromic one, it is also possible to manipulate the absorption properties of the former with the latter. In these systems, the photochromic component is essentially a switchable auxochrome able to regulate reversibly the energy gap between the S_1 and S_0 of the fluorescent component. For example, compound **4a** (Figure 1.4) joins a coumarin fluorophore to an oxazine photochrome through a vinylene spacer.[33a,c] Its absorption spectrum shows a band centered at a $^a\lambda_{Ab}$ of 412 nm in acetonitrile for the coumarin component. Irradiation at a $^a\lambda_{Ac}$ of 355 nm excites the 4-nitrophenoxy chromophore and results in the opening of the adjacent oxazine ring to form the zwitterionic isomer **4b** with a ϕ_{Ac} of 2×10^{-2}. This structural transformation brings the coumarin appendage in

conjugation with the photogenerated 3H-indolium cation and shifts its absorption band to a $^b\lambda_{Ab}$ of 570 nm. Illumination at a λ_{Ex} positioned within this band excites exclusively the coumarin fluorophore of the photogenerated isomer. In fact, the corresponding emission spectrum shows a band at a λ_{Em} of 650 nm with a ϕ_{Em} of 9×10^{-2}. Thus, the photoinduced control of the $S_0 \rightarrow S_1$ transition (*a* in Figure 1.2) is, yet again, responsible for activating fluorescence. The photogenerated isomer **4b**, however, reverts spontaneously back to the original species **4a**. This thermal process occurs with first-order kinetics on a microsecond timescale and the lifetime of **4b** is only 0.2 μs. As a result, the fluorescence of this system can be modulated for multiple cycles, on a relatively short timescale, simply by turning on and off a light source operating at λ_{Ac}, while illuminating the sample with another source centered at λ_{Ex}.

1.3. Monitoring Dynamics

The dynamics of emissive molecules can be probed conveniently with the aid of fluorescence measurements in combination with appropriate illumination protocols.[28] These spectroscopic techniques can be extended to the investigation of the translational diffusion of biomolecules and macromolecular constructs, labeled with fluorescent tags. In particular, fluorescence recovery after photobleaching[64] (FRAP) has become an invaluable analytical tool to monitor a diversity of dynamic events. In a FRAP experiment, a defined area within a labeled sample is first illuminated at the excitation wavelength of the fluorescent probes with relatively high intensities. These harsh irradiation conditions ensure the bleaching of the fluorophores positioned within the illuminated area and turn their emission off permanently. The subsequent diffusion of

intact fluorophores inside the bleached area result in a gradual emission increase within this particular region at a rate that is directly related to the translational diffusion coefficient of the emissive species. Thus, sequential measurements of the emission intensity offer the opportunity to assess diffusion quantitatively. Alternatively, an inverse illumination protocol can be employed to monitor these dynamic events. In inverse FRAP, the entire labeled sample is illuminated with a bleaching beam with the exception of a defined area. Intact fluorophores can then diffuse out of the unexposed region, leading to a gradual decrease in emission intensity within this particular area of the sample. Once again, the rate of fluorescence change is directly related to the translational diffusion coefficient of the emissive species and, therefore, this parameter can be determined simply by monitoring the emission intensity in time.
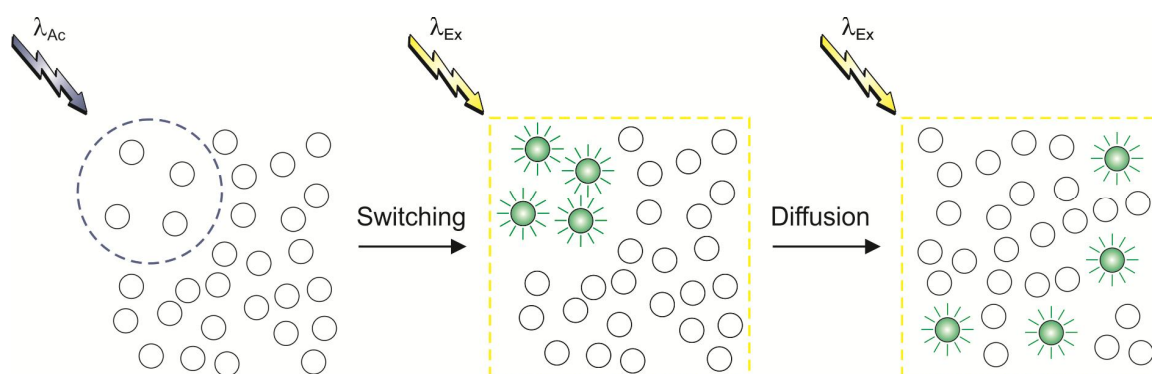
Figure 1.5. Illumination at λ_{Ac} of a region of interest within a sample labeled with photoactivatable fluorophores activates fluorescence. The subsequent acquisition of images under irradiation at λ_{Ex} can then probe the diffusion of the fluorophores out of the activated region.

Photoactivatable fluorophores can be exploited to replicate the sequence of events associated with inverse FRAP.[1,2,4,8-13] Indeed, a sample of interest can be labeled with these switchable compounds in their nonemissive state. Illumination of a defined area within the sample at λ_{Ac} switches the probes to their emissive state (Figure 1.5). The

subsequent acquisition of a fluorescence image under illumination at λ_{Ex} is then expected to reveal significant fluorescence exclusively within the activated area. If the emissive species are able to diffuse out of this particular region, however, the emission intensity will gradually decrease. Therefore, images recorded in sequence, after activation, can provide quantitative information on the diffusion process, in analogy to inverse FRAP. Furthermore, most photoactivatable fluorophore require only moderate illumination intensities to switch from their nonemissive state to the emissive one. As a result, their use offers the opportunity to avoid the harsh irradiation conditions that are, instead, needed for the bleaching step of FRAP experiments. In fact, the mild illumination doses required for this imaging protocol are particularly convenient for the investigation of the translational diffusion of species in living cells.[29,39,43,44,47,65-69]
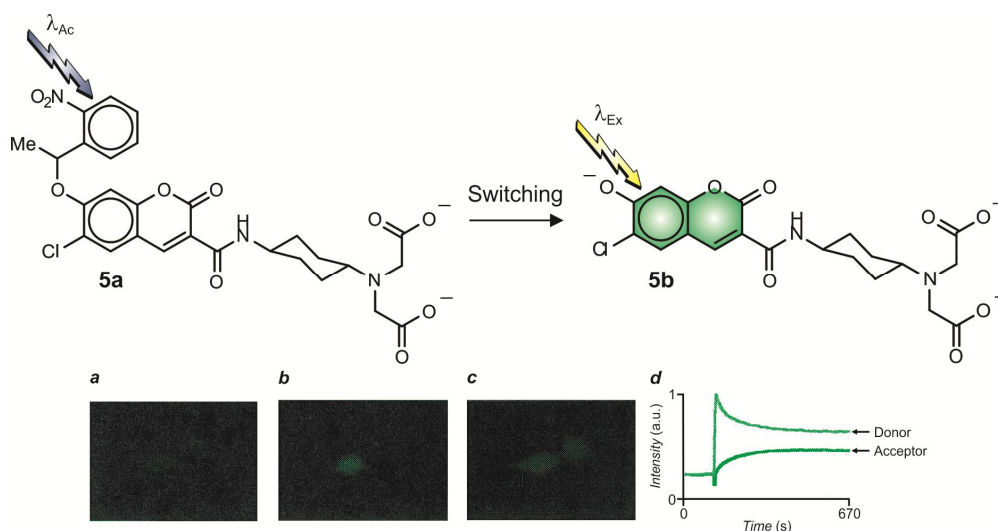
Figure 1.6. Images of two coupled primary human fibroblasts, incubated with a photoactivatable coumarin, were recorded, under irradiation at λ_{Ex}, before (*a*) and after (*b*) illumination of one cell at λ_{Ac} to reveal the appearance of fluorescence exclusively in the activated region. The activated fluorophores, however, can transfer from one cell to the other and after 400 s both show significant fluorescence (*c*). Consistently, the emission intensity (*d*) of the donor cell decreases over time with a concomitant increase in the fluorescence of the acceptor cell [Reproduced from ref. 67a with permission].
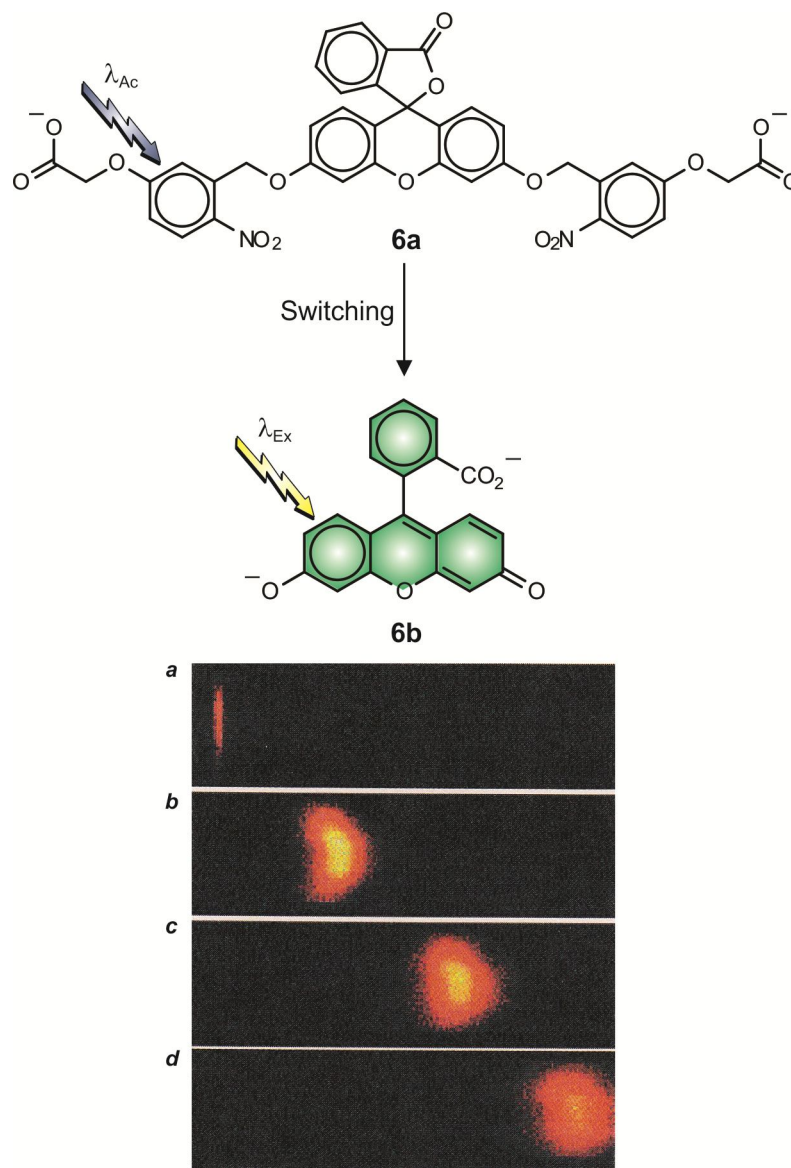
Figure 1.7. Images of a microchannel, imprinted within a poly(methyl methacrylate) matrix and filled with a solution of a photoactivatable fluorescein in carbonate buffer, were recorded under the influence of an electric field and irradiation at λ_{Ex}. A laser pulse at λ_{Ac} was focused on the sample to activate fluorescence exclusively within a rectangular area (*a*). Consecutive frames (*b–d*) were acquired after activation with a delay of 50 ms between them to monitor the translation of the activated fluorophores along the direction of the electroosmotic flow [Reproduced from ref. 73b with permission].

A remarkable example of these operating principles to monitor dynamic events is illustrated in Figure 1.6.[67a] In this experiment, the diffusion of a fluorophore from a donor

cell to an acceptor cell was probed in real time. Specifically, the transfer of a photoactivatable coumarin across the gap junction of two primary human fibroblasts was followed by measuring the fluorescence changes in both cells after the photoinduced switching of **5a** to **5b**. An image (*a* in Figure 1.6) of the pair of cells, recorded under irradiation at λ_{Ex} after incubation with the photoactivatable probes but before activation, does not reveal any significant emission. Illumination at λ_{Ac} of one of the two cells activates the fluorophores exclusively in the irradiated region, producing fluorescence in the corresponding image (*b* in Figure 1.6). The activated fluorophores can then migrate from one cell to the other over the course of several seconds. In fact, an image (*c* in Figure 1.6) recorded after 400 s clearly reveals fluorescence in both cells. The temporal evolution (*d* in Figure 1.6) of the emission intensities in the two cells further confirms the spatial redistribution of fluorescence and indicates that the activated fluorophores migrate across the gap junction with a transfer rate of 1.2×10^{-2} s^{-1}. Indeed, the decrease of the emission intensity measured in the donor cell, after an activation pulse, is paralleled by a concomitant increase in the acceptor cell.

Similar illumination protocols, in combination with the activation and excitation events characteristic of photoactivatable fluorophores, can also be exploited to monitor the flow dynamics of liquids.[70-75] A representative example of this imaging strategy to probe electroosmotic flow is illustrated in Figure 1.7.[73b] In this experiment, a microstructured channel, imprinted within a poly(methyl methacrylate) matrix, was filled with a solution of a photoactivatable fluorescein in carbonate buffer. Platinum electrodes were placed in contact with the solution and an appropriate voltage was applied to induce electroosmotic flow. A stripe orthogonal to the main axis of the channel was illuminated

at λ_{Ac} to convert the nonemissive species **6a** to the emissive one **6b** (*a* in Figure 1.7), while imaging a relatively large section of the substrate under irradiation at λ_{Ex}. Consecutive images (***b–d*** in Figure 1.7) were then recorded with a delay of 50 ms between them. The overall sequence of frames clearly reveals the translation of the activated fluorophores across the channel in the direction of the electroosmotic flow.

1.4. Superresolution Imaging

Fluorescence imaging permits the noninvasive visualization of samples, labeled with emissive species, in real time.[76] The acquisition of these images requires first the excitation of the fluorescent labels at an appropriate wavelength with a light source and then the collection of the emitted radiation on a detector. Both processes demand the use of a lens to focus the exciting and emitted radiation. In turn, the phenomenon of focusing is accompanied by that of diffraction and the latter ultimately dictates the minimal size of the focal spot. Specifically, a point source of light appears on the focal plane of a lens in the form of an Airy pattern of concentric rings with an inner disk (Figure 1.8). The physical dimensions of the pattern are mostly defined by the wavelength of the emitted light, rather than by the actual size of the emission source. In fact, the radius of the inner disk is approximately equal to half of the wavelength. As a result, even a single fluorophore of subnanometer dimensions, emitting light in the visible region, can only appear in the form of a pattern of hundreds of nanometers in size. Thus, two molecules emitting light simultaneously can be distinguished only if they are hundreds of nanometers apart. Indeed, the spatial resolution of conventional fluorescence images, acquired with visible light, is limited to such length scale and, therefore, prevents the visualization of structural factors at the molecular level.
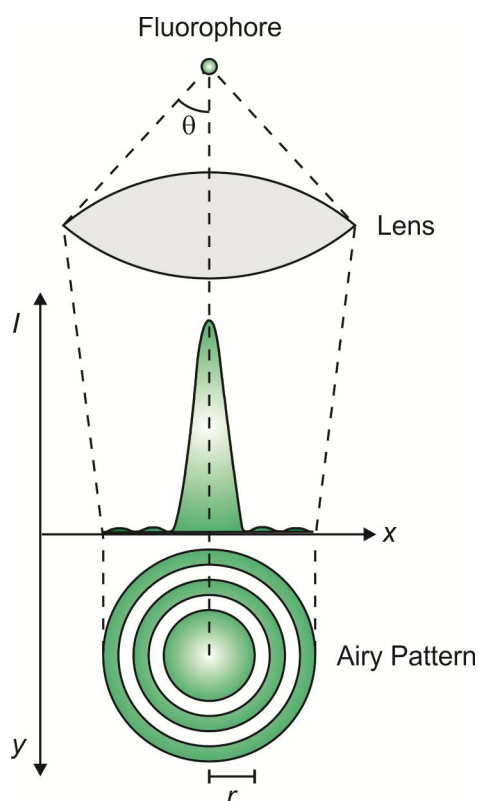
Figure 1.8. The objective lens of a fluorescence microscope projects the light emitted by a fluorophore on the focal plane in the form of an Airy pattern with most of the focused light concentrated in the central disk

The stringent limitations imposed by diffraction on the spatial resolution of fluorescence images can be overcome with the aid of switching events.[14-21,77] In particular, fluorescence can be confined within a volume of subdiffraction dimensions relying on patterned illumination of an emissive sample with a pair of lasers designed to switch on and off fluorescence respectively. Specifically, one of the two lasers can be engineered to produce a diffraction limited spot on the focal plane of the sample at the wavelength required to excite the fluorescent labels. The second laser can be designed to generate a concentric doughnut-shaped spot at a wavelength able to deplete the excited state of the labels on the basis of stimulated emission. Under these conditions, emission is

restricted exclusively within a region of subdiffraction dimensions in the hole of the doughnut. In fact, the intensities of the exciting and depleting beams together with the rates of the associated electronic transitions ultimately define the size of the fluorescent spot, rather than the actual phenomenon of diffraction. Therefore, the scanning of the two concentric luminous patterns across the labeled sample allows the point-by-point acquisition of a complete image with a spatial resolution that is otherwise impossible to achieve with conventional illumination. Indeed, these operating principles for subdiffraction imaging have eventually evolved into an established technique, termed stimulated emission depletion[16,78] (STED), for the investigation of a diversity of samples.
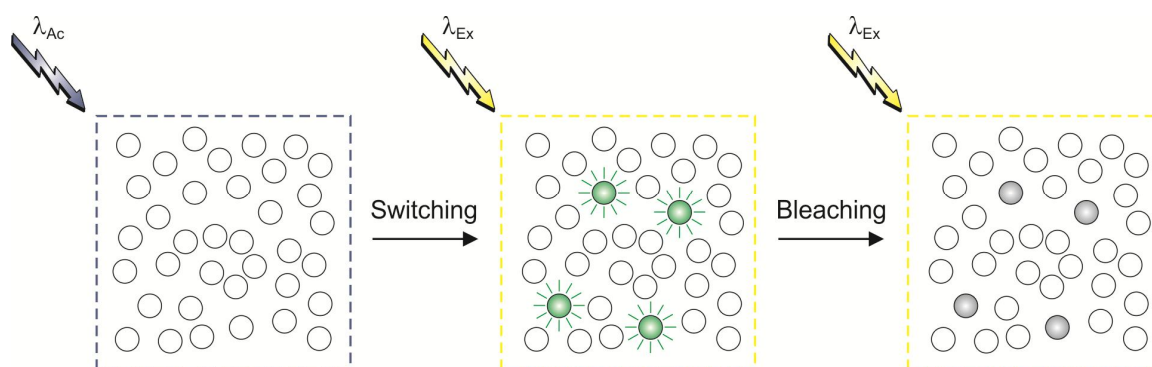
Figure 1.9. Sequential illumination at λ_{Ac} and λ_{Ex} of a sample, labeled with photoactivatable fluorophores, permits the activation and localization respectively of individual probes. Further irradiation at λ_{Ex} bleaches the localized probes and turns their fluorescence off permanently. Reiterations of this sequence of events permit the sequential mapping of multiple fluorescent labels and the reconstruction of an image with nanoscaled resolution.

In alternative to the synchronous scanning of exciting and depleting beams, images with subdiffraction resolution can be reconstructed on the basis of wide-filed illumination and single-molecule detection in combination with, once again, switching events.[14-21] Specifically, multiple fluorophores at subdiffraction separations can be distinguished if they are designed to emit individually at different intervals of time.

Under these conditions, the sequential acquisition of images offers the opportunity to map the position of independent fluorescent labels with spatial resolution at the nanometer level. The crucial requirement for the implementation of these operating principles, however, is the need to turn on and off independently the emission of fluorophores positioned within the same subdiffraction area. The concatenation of activation and excitation events associated with photoactivatable fluorophores provides this opportunity. In fact, representative examples [33c,f,37c,48-50,79-84] of such compounds have already been exploited to reconstruct images with subdiffraction resolution on the wake of three seminal reports.[85-87] In this imaging protocol, termed photoactivation localization microscopy (PALM),[85,87] a sample of interest is labeled with photoactivatable probes in their nonemissive state (Figure 1.9). The specimen is then illuminated at λ_{Ac} with moderate intensities to ensure the switching of a sparse population of species to their emissive state. This crucial condition is necessary to maximize the probability of finding a single emissive species per subdiffraction area. Subsequent irradiation at λ_{Ex} excites the activated probes and, if they are sufficiently bright, permits their localization at the single-molecule level. Each localized probe is visualized in the form of a diffraction pattern and the center of the latter can be approximated to the position of the molecule. The coordinates of each localized probe can then be stored and the sample can be illuminated at λ_{Ex}, until the activated and localized probes bleach. Once their fluorescence is permanently suppressed, a new subset of fluorophores can be activated, localized and bleached. This sequence of events can be reiterated multiple times, until enough coordinates become available to reconstruct a complete image of the sample. Under these conditions, the spatial resolution of the final image is not limited by

diffraction. Instead, it is mostly defined by the number of emitted photons collected per probe and the background noise. If the former parameter is large and the latter one is small, then the lateral resolution of the final image can be squeezed down to the nanometer level.

Essentially the same operating principles for image reconstruction can be implemented with switchable probes that are initially in an emissive state and then are deactivated transiently to a nonemissive form under irradiation. In this imaging protocol, termed stochastic optical reconstruction microscopy (STORM),[86] the switching events ensure fluorescence intermittency and permit, once again, the temporal separation of closely-spaced emissive species. The mechanisms responsible for deactivation in STORM, however, are significantly different from those governing activation in PALM. Generally, reactions of the probes with appropriate reagents, present in the sample under investigation, are exploited to convert the emissive species into nonemissive ones under illumination at an appropriate wavelength. The nonemissive and photogenerated species can revert to the original state spontaneously or upon irradiation at a different wavelength. Under these conditions, the irradiation intensities and the concentrations of the reactants can be adjusted to maintain only a sparse population of probes in the emissive state at any given time, during the image reconstruction sequence. In particular, the photoinduced addition of nucleophiles along the polymethyne bridge of cyanines[88] and the photoinduced exchange of electrons between conventional fluorophores and complementary acceptors/donors[89-94] have been employed successfully to implement these operating principles and acquire STORM images of a diversity of specimens.
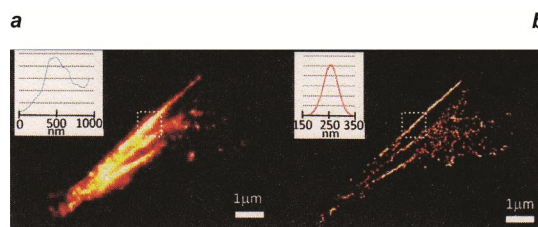
Figure 1.10. Diffraction-limited (*a*) and PALM (*b*) images of fixed BS-C-1 cells, labeled with a photoactivatable dihydrofuran, reveal the tubulin structure in both instances. However, the image reconstruction protocol associated with the latter ensures an enhancement in spatial resolution. Consistently, the cross-sections of the highlighted areas show the microtubules to appear with a width of 450 nm in the diffraction-limited image and only 85 nm in the PALM counterpart [Reproduced from ref. 37c with permission].

The remarkable enhancement in spatial resolution possible with PALM is evident from the images in Figure 1.10.[37c] Both reveal the tubulin structure of fixed BS-C-1 cells labeled with a derivative of the photoactivatable dihydrofuran **1a**. The microtubules in one, however, are significantly less resolved than in the other. Specifically, they appear to have a width of 450 nm in the conventional diffraction-limited image (*a* in Figure 1.10) and only 85 nm in the corresponding PALM map (*b* in Figure 1.10). The latter image was reconstructed from a sequence of frames acquired under illumination with ambient light, to activate the probes, and a laser, to excite the activated fluorophores. The doses of the two light sources were regulated to ensure similar activation and bleaching rates in order to maintain a sparse subset of emissive species at any given time. Under these conditions, independent fluorophores activate stochastically and eventually turn off in the course of the frame acquisition sequence. As a result, evolving populations of fluorophores can be mapped sequentially to reconstruct gradually the profile of the labeled microtubules with subdiffraction resolution.
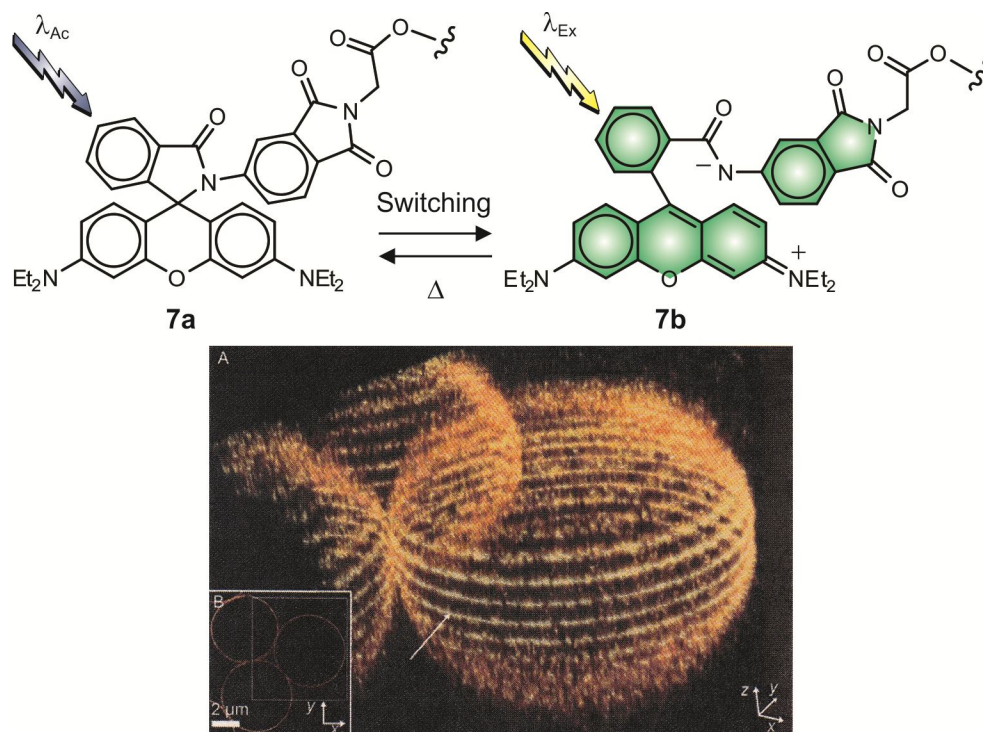
Figure 1.11. Two-photon activation of photoactivatable rhodamines, attached to silica beads, permit the reconstruction of a PALM map (*a*) in three-dimensions after the sequential imaging of 17 individual planes (*b*) with a spacing of 330 nm in the vertical direction [Reproduced from ref. 48a with permission].

The operating principles of this powerful technique can also be adapted to record superresolution images with two detection channels in parallel.[79] Indeed, the labeling of a sample with a pair of photoswitchable fluorophores with resolved emission bands permits the simultaneous two-color visualization of features with subdiffraction dimensions. For example, the keratin and microtubule networks of PtK2 cells, immunolabeled with two photoactivatable rhodamines, could be imaged in parallel relying on this strategy.[79a] The two sets of probes employed in this experiment can be activated at the very same λ_{Ac} and then excited at the very same λ_{Ex}, but emit at sufficiently different wavelengths to permit the detection of their fluorescence in two independent channels. Furthermore, the resolution of these images in the horizontal plane can be increased even further by

mounting the sample between two opposing objectives lenses.[79b, 95] This configuration doubles the number of photons collected from the sample and results in a significant increase in localization precision. In addition, this setup enhances the resolution in the vertical direction and enables the reconstruction of images in three dimensions.[79b]

In alternative to engineering the point-spread function with manipulations in the illumination configuration,[79b,96] PALM imaging can be extend to the third dimension relying on two-photon activation.[48a] The three-dimensional map in Figure 1.11 is a clear demonstration of the potential of this imaging technique, although the spatial resolution in the vertical direction of this representation remains diffraction limited. In this experiment, silica beads of micrometer size were labeled with the photoactivatable rhodamine **7a**. This particular compound has a relatively large two-photon absorption cross section and can be switched to **7b** with near-infrared radiations. This choice of wavelengths offers the opportunity to avoid the ultraviolet radiations that are generally required to switch most photoactivatable synthetic fluorophores and, as a result, the deleterious consequence that relatively short illumination wavelengths might have on biological samples. In addition, the stringent spatial and temporal requirements for two-photon absorption translate into the possibility of sectioning a sample in the vertical direction. In fact, the image in Figure 1.11 was reconstructed after imaging sequentially 17 parallel sections of the sample with a spacing between them of 330 nm.

1.5. Photochemical and Photophysical Parameters

The mechanisms responsible for fluorescence switching in photoactivatable fluorophores require the coupling of a photochemical reaction (activation) with a photophysical

process (emission). The former demands the absorption of activating radiations at λ_{Ac} and the transformation of the nonemissive state into the emissive one. The latter requires the photochemical product to absorb exciting radiations at λ_{Ex} and emit light in the form of fluorescence. Therefore, the molar extinction coefficient (ε_{Ac}) of the nonemissive species at λ_{Ac} and ϕ_{Ac} are the two main parameters in control of activation. Similarly, the molar extinction coefficient (ε_{Ex}) of the emissive species at λ_{Ex} and ϕ_{Em} are the two main parameters in control of emission.

Applications aimed at monitoring dynamic processes demand the formation of the emissive product on timescales significantly shorter than those of the dynamic process under investigation. As a result, ε_{Ac} and ϕ_{Ac} should ideally be as large as possible to ensure fast activation at moderate illumination intensities. In addition, the photogenerated species must persist in the emissive state over the entire course of the dynamic event under analysis. Therefore, irreversible photoactivatable fluorophores with good photobleaching resistances are generally employed in these investigations.

Applications aimed at the reconstruction of superresolution images require instead the activation of only a sparse population of fluorophores at a given time. As a consequence, moderate ε_{Ac} and ϕ_{Ac} can be sufficient for these imaging strategies. In fact, excessive photosensitivity might translate in the need to protect specimens from ambient light, complicating labeling procedures and sample manipulation.[37c] Furthermore, the photochemical transformation responsible for activation does not necessarily need to be irreversible in these instances. Reversibility might actually offer the opportunity to avoid the bleaching step required in the reiterative sequence of events for image reconstruction.

However, the emissive species must be able to persist in this form for a sufficient period of time to permit detection at the single-molecule level before switching back to the nonemissive state. Specifically, the number of emitted photons detected per active probe should be as large as possible to ensure a localization precision at the nanometer level. Therefore, the emissive species must be as bright as possible and must survive in this form for a sufficient amount of time to enable multiple excitation/emission cycles before either switching back to the nonemissive state or bleaching permanently. Thus, the brightness of this species, which is the product of ε_{Ex} and ϕ_{Em}, and its photobleaching resistance must be as large as possible. In addition, the kinetics of its reactivation, if at all happening, must be compatible with the temporal response of the detector.

The spatial resolution of superresolution images, reconstructed on the basis of activation and excitation events, is also related to the background noise. Indeed, negligible background is an essential condition to achieve localization precision at the nanometer level. In turn, the noise level is related to the ratio between the emission intensity of the activated fluorophores and any residual fluorescence that might be coming from probes in their initial form. As a result, activation mechanisms based on a photoinduced bathochromic shift in the $S_0 \rightarrow S_1$ absorption are generally more appropriate for these imaging strategies. Under these conditions, only the photogenerated product can absorb exciting radiations of λ_{Ex}, ensuring a minimal contribution of the initial species to the overall emission intensity and a virtually infinite contrast ratio. In addition, these mechanisms also prevent the undesired photodegradation of the probes prior to activation. In fact, the bleaching step, required in the reiterative image reconstruction sequence, demands prolonged irradiation at λ_{Ex} to turn the emission of the

activated fluorophores off permanently. Therefore, the initial state of the photoactivatable probes should not absorb the bleaching radiations at λ_{Ex}.

1.6. Conclusions

The fluorescence of synthetic chromophores can be engineered to switch on in the response to illumination on the basis of two main mechanisms. In one instance, a photochemical transformation is designed to control the ability of a chromophore to absorb exciting radiations. In the other, the photochemical event facilitates the radiative decay of the excited chromophore. Both result in fluorescence activation after illumination at activating and exciting wavelengths. Such concatenation of activation and excitation events can be exploited to probe dynamic processes in real time. In fact, the diffusion of molecules in a diversity of media as well as the flow of liquids in microstructured channels can both be probed effectively with this general strategy. In addition, operating principles for fluorescence activation, based on the photoinduced manipulation of absorption properties, can be exploited to overcome the limitations that diffraction imposes on the spatial resolution of conventional microscopes. Indeed, biological specimens, labeled with photoactivatable fluorophores, can be visualized with resolution at the nanometer level on the basis of this imaging protocol. Thus, these photoresponsive molecular switches can be particularly valuable in the investigation of a diversity of samples with spatial and temporal resolution that are otherwise impossible to achieve with conventional fluorophores. Therefore, fundamental investigations aimed at improving their photochemical and photophysical properties, with the aid of chemical synthesis and spectroscopic analysis, can ultimately provide invaluable analytical tools for biomedical research and materials science.

CHAPTER 2

FLUORESCENCE PHOTOACTIVATION BY INTERMOLECULAR PROTON TRANSFER

2.1. Overview

Fluorescence microscopy[76] is an invaluable analytical tool for the structural investigation of materials at the micrometer level. It is based on the introduction of appropriate fluorescent labels[28] within a sample of interest and the subsequent acquisition of images, after the excitation of the probes and the collection of their emission. The development of fluorophores with optimal photochemical and photophysical properties, as well as of efficient and versatile labeling protocols, is therefore of central importance for the further advancement of this convenient imaging technique. In particular, the identification of mechanisms to photoactivate fluorescence[3,97] can facilitate the elucidation of dynamic processes in real time[1,2] and the visualization of structural features with subdiffraction resolution.[16,18,78,99] Indeed, probes able to switch from a nonemissive state to a fluorescent one under optical control offer the opportunity to monitor the translocation of labeled species within a material.

Most photoactivatable fluorophores are designed around the ability of one or more photocleavable groups to dissociate from an emissive chromophore, upon illumination at an appropriate wavelength.[3,5-7,11,97] This photochemical transformation alters the electronic structure of the chromophore and either enables its absorption of an exciting radiation or discourages the nonradiative decay of its excited state. Both mechanisms translate into fluorescence activation. Inspired by earlier work on photoinduced proton transfer[104] in the group, I designed an alternative strategy to photoinduce the activation of

fluorescence. Specifically, I envisaged the possibility of combining a molecule capable of releasing acid upon illumination with an emissive halochromic compound. In the resulting bimolecular system, the photoinduced transfer of a proton from the former to the latter can be exploited to control the electronic structure of the emissive species and activate its fluorescence. Indeed, such a mechanism to activate fluorescence demands the intermolecular communication of two independent components, rather than the dissociation of a single molecular species. Therefore, it offers the unique opportunity to probe the signal (*i.e.*, a proton) propagating from one component to the other with fluorescence measurements. Herein, I report the implementation of these operating principles for fluorescence photoactivation in liquid solutions, within rigid matrices as well as the application of this strategy to monitor the diffusion of protons within polymer films in real time.

2.2. Results and Discussion

2.2.1. Absorption and Emission Spectroscopy

The covalent backbone of **4a** (Figure 2.1) incorporates a coumarin fluorophore and an oxazine switch and can be assembled in a single synthetic step from known precursors.[33a,c] The absorption spectrum (*a* in Figure 2.1) of an acetonitrile solution of this compound shows a band centered at 412 nm for the coumarin appendage. Upon addition of a single equivalent of trifluoroacetic acid (TFA), this band decreases in intensity and a new one appears at 593 nm in the corresponding spectrum (*b* in Figure 2.1). This pronounced spectral change is a result of the opening of the oxazine ring with the formation of **4c**. Indeed, such structural transformation brings the coumarin

fluorophore in conjugation with the adjacent 3*H*-indolium cation and shifts its main absorption bathochromically. In turn, the illumination of the resulting solution at an excitation wavelength (λ_{Ex}) comprised within this band excites selectively the coumarin fragment of **4c** with concomitant fluorescence. In fact, the corresponding emission band (*c* in Figure 2.1) can be observed at 685 nm only after the addition of acid, demonstrating that the halochromic transformation of **4a** into **4c** can be exploited to activate fluorescence.
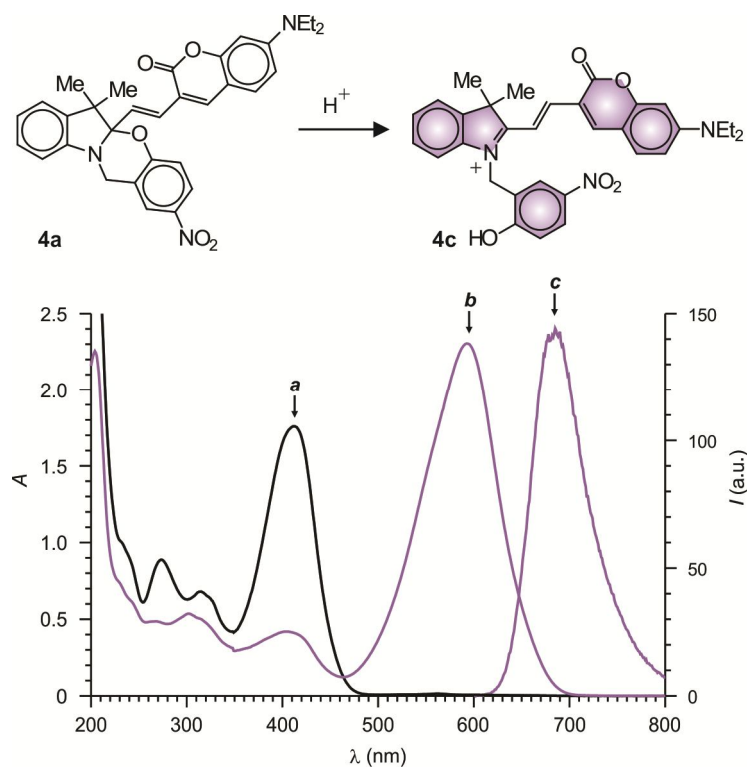
Figure 2.1. Absorption spectra of a solution (0.1 mM, MeCN, 25 °C) of **4a** recorded before (*a*) and after (*b*) the addition of TFA (1 equiv). Emission spectrum (λ_{Ex} = 590 nm) of the acidified solution (*c*).

The halochromic conversion of **4a** into **4c** can be encouraged with the assistance of a compound able to release acid under illumination at an appropriate activation wavelength (λ_{Ac}). Indeed, a molecule capable of transferring a proton to **4a** upon irradiation can

mediate the photochemical formation of **4c** and activate fluorescence. For example, the established photochemistry of the 2-nitrobenzyl group[11,97] can be adapted to photogenerate acid.[105] Specifically, the photolysis of **8** (Figure 2.2) results in the formation of **9** and hydrogen bromide. Consistently, the absorption spectra, recorded before (*a* in Figure 2.2) and during (*b–f* in Figure 2.2) the course of irradiation at λ_{Ac} in acetonitrile, reveal a decrease in the absorbance associated with **8** at 249 nm and the concomitant appearance of a new band for **9** at *ca.* 400 nm.
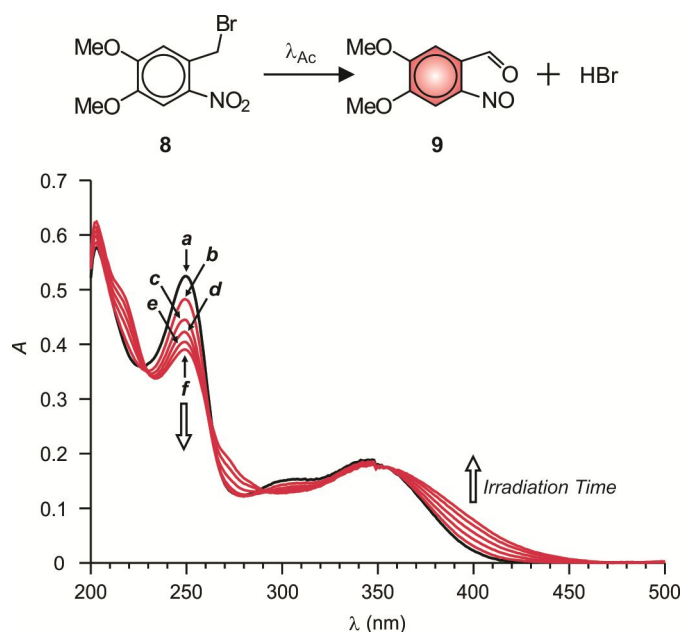
Figure 2.2. Absorption spectra of a solution (0.1 mM, MeCN, 25 °C) of **8** recorded before (*a*) and after irradiation (λ_{Ac} = 365 nm, 0.4 mW cm^{-2}) for 1 (*b*), 2 (*c*), 3 (*d*), 4 (*e*) and 5 min (*f*).

In the presence of equimolar amounts of **4a** and under otherwise identical conditions, the photolysis of **8** causes essentially the same bathochromic shift observed for **4a** after the addition of TFA.[106] Once again, the initial absorption spectrum (*a* in Figure 2.3) shows a band at 412 nm for the coumarin appendage of **4a**. After illumination at λ_{Ac} (*b* in Figure 2.3), the absorbance of this band decreases with the concomitant

appearance of a new band at 595 nm for the extended cationic chromophore of **4c**. Irradiation of the resulting solution at λ_{Ex} excites selectively the coumarin fragment of the protonated species and is accompanied by the appearance of characteristic emission band (*c* in Figure 2.3) of **4c** at 687 nm. Thus, the acid released during the course of the photochemical conversion of **8** into **9** encourages the protonation of **4a** with the formation of **4c** and activates fluorescence.
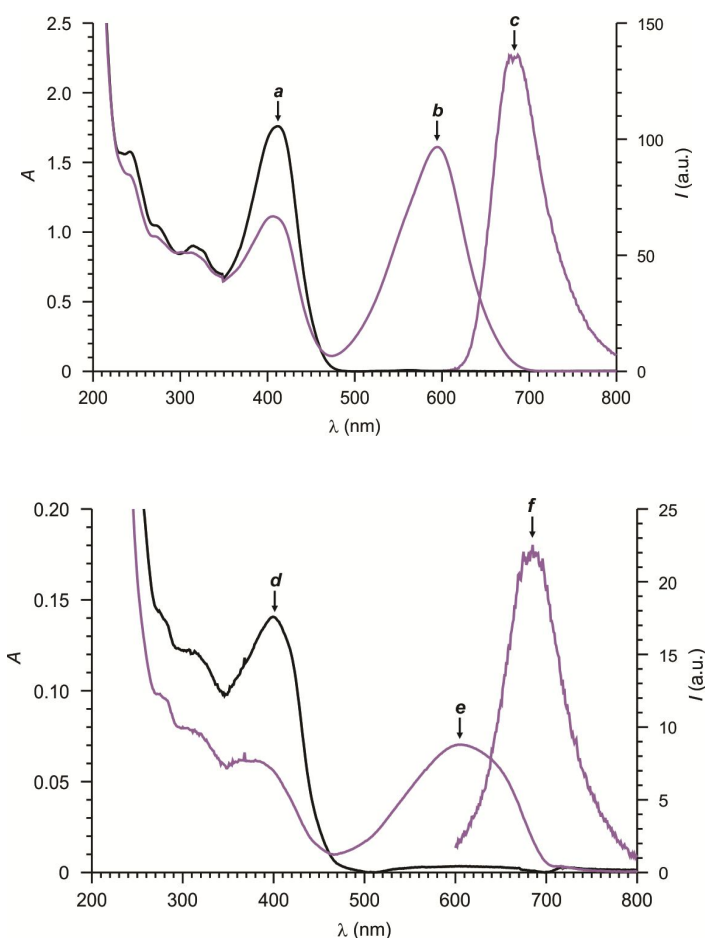
Figure 2.3. Absorption spectra of an equimolar solution (0.1 mM, MeCN, 25 °C) of **4a** and **8** recorded before (*a*) and after (*b*) irradiation (λ_{Ac} = 365 nm, 0.4 mW cm^{-2}, 5 min). Emission spectrum (λ_{Ex} = 590 nm) of the irradiated solution (*c*). Absorption spectra of a PBMA film, doped with **4a** (2% w/w) and **8** (1% w/w) and spin-coated on a quartz slide, recorded before (*d*) and after (*e*) irradiation (λ_{Ac} = 365 nm, 0.4 mW cm^{-2}, 5 min). Emission spectrum (λ_{Ex} = 590 nm) of the irradiated film (*f*).

The photoinduced transformation of **4a** into **4c** can be reproduced within a rigid polymer matrix, once again, under the assistance of **8**. As observed in acetonitrile, the absorption spectrum (**d** in Figure 2.3) of a poly(*n*-butyl methacrylate) (PBMA) film, doped with equimolar amounts of **4a** and **8** and spin-coated on quartz, shows a band at 399 nm for the coumarin chromophore of **4a**. After irradiation at λ_{Ac} (**e** in Figure 2.3), the absorbance of this band decreases and a new one develops at 606 nm in agreement with the formation of **4c**.[106] Irradiation at λ_{Ex} excites the coumarin appendage of the protonated species and results in the appearance of the characteristic emission band (**f** in Figure 2.3) of **4c** at 685 nm. Thus, the acid generated during the photochemical conversion of **8** into **9** can diffuse within the relatively rigid and hydrophobic polymer matrix to encourage the halochromic transformation of **4a** into **4c** with concomitant fluorescence activation.

2.2.2. Ensemble Imaging

Confocal laser-scanning fluorescence images of PBMA films doped with **4a** and **8** reveal the appearance of fluorescent patterns only after photoinduced activation. In particular, the image (**a** in Figure 2.4) recorded with a λ_{Ex} of 514 nm, where neither **4a** nor **8** absorb, does not show any significant fluorescence. After illumination at a λ_{Ac} of 405 nm exclusively within a circular spot at the center of the imaging field, however, the image (**b** in Figure 2.4) recorded with the same λ_{Ex} clearly reveals fluorescence activation.[107] Indeed, the beam at λ_{Ac} induces first the transformation of **8** into **9** and then that of **4a** into **4c** within the illuminated spot, while that at λ_{Ex} excites selectively the photogenerated species **4c** and produces fluorescence in the activated area. Furthermore, the very same fluorescent pattern can be observed again in the image (**c** in Figure 2.4)

recorded after 5 min from activation, demonstrating that **4c** cannot diffuse within the polymer film.
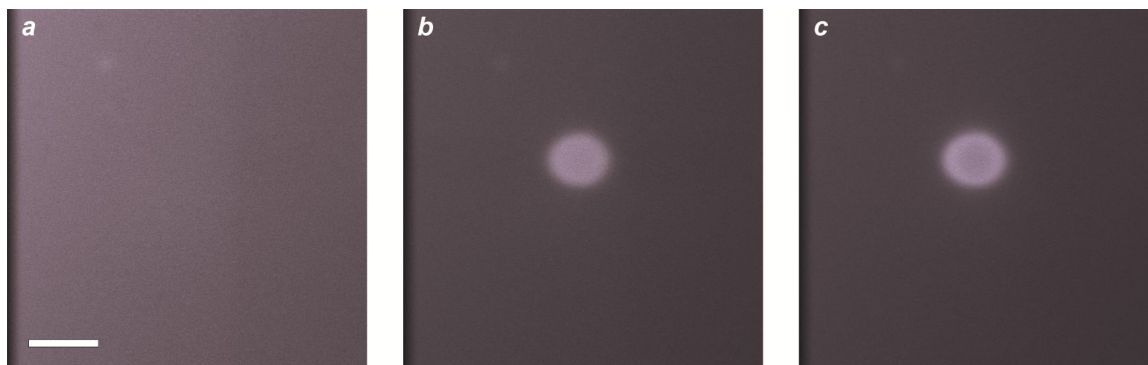
Figure 2.4. Confocal laser-scanning fluorescence images (λ_{Ex} = 514 nm, 40 µW, λ_{Em} = 600–800 nm, scale bar = 5 µm) of a PBMA film, doped with **4a** (2% w/w) and **8** (1% w/w) and spin-coated on a glass slide, recorded before (*a*), immediately after (*b*) and 5 min after (*c*) laser illumination (λ_{Ac} = 405 nm, 1 mW, 1 s) of a circular spot within the imaging field.

The observed activation of fluorescence is indicative of proton diffusion within the polymer matrix. Indeed, the hydrogen bromide released from **8** upon irradiation must be able to travel within the film and reach **4a** in order to encourage the formation of the fluorescent species **4c**. In fact, proton diffusion can be monitored in real time with the sequential acquisition of frames under simultaneous illumination at λ_{Ac} and λ_{Ex} to activate **8** and excite **4c** respectively. Specifically, the irradiation at λ_{Ac} of a rectangular area at the top edge of the imaging field generates acid only within the illuminated region. As a result, the simultaneous irradiation of the entire imaging field at λ_{Ex} reveals fluorescence only within the activated area in the initial frame (*a* in Figure 2.5). The subsequent acquisition of frames (*b* and *c* in Figure 2.5) at intervals of 50 ms under these illumination conditions, however, shows a gradual increase in fluorescence outside the activated area (Figure 2.5). This behavior suggests that a fraction of the photogenerated

hydrogen bromide eventually diffuses out of the activated area and encourages the formation of the fluorescent species **4c** along its path, until it is completely consumed over the course of a few seconds.
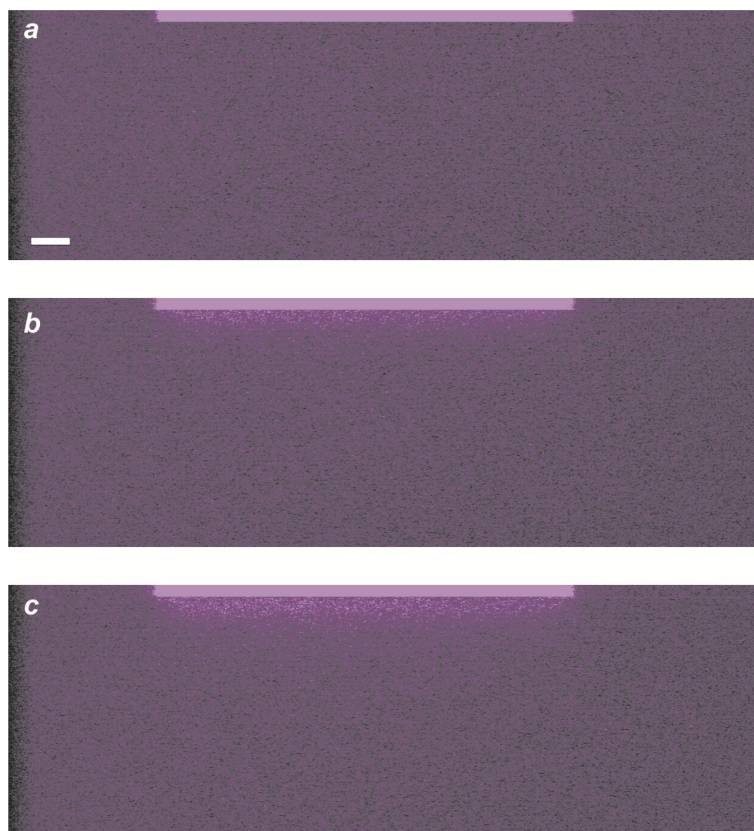
Figure 2.5. Confocal laser-scanning fluorescence images (λ_{Ex} = 514 nm, 7 µW, λ_{Em} = 600–800 nm, scale bar = 5 µm) of a PBMA film, doped with **4a** (2% w/w) and **8** (1% w/w) and spin-coated on a glass slide, recorded during laser illumination (λ_{Ac} = 405 nm, 1 mW) of a rectangular area at the top edge of the imaging field with a frame interval of 50 ms (*a* = frame 1, *b* = frame 250 and *c* = frame 500).

2.3. Conclusions

These results demonstrate that the release of acid from a 2-nitrobenzyl derivative, upon irradiation at an activating wavelength, can be exploited to induce a halochromic transformation within a coumarin–oxazine dyad. The coumarin appendage within the

halochromic product can then be excited selectively with concomitant fluorescence, under illumination at an appropriate excitation wavelength. In fact, this bimolecular system offers the opportunity to photoactivate fluorescence in liquid solutions and within rigid matrices, relying on the interplay of activating and exciting beams. Furthermore, fluorescent patterns can be imprinted permanently in PBMA films doped with both the photoacid generator and the emissive halochromic compound. This choice of functional components permits also the monitoring of proton diffusion from one component to the other within the relatively rigid and hydrophobic polymer matrix in real time. Thus, our operating principles for fluorescence activation can ultimately lead to the development of valuable probes for the investigation of proton transport in a diversity of materials.

CHAPTER 3

SUPERRESOLUTION IMAGING WITH SWITCHABLE FLUOROPHORES BASED ON OXAZINE AUXOCHROMES

3.1. Overview

Far-field fluorescence microscopy is a widely applied and powerful tool for biological imaging that provides noninvasive 3D visualization of cells and tissues with a unique combination of high selectivity and sensitivity, and fast temporal resolution. A conventional fluorescence microscope is a system of several lenses that produce a magnified image of the observation object, usually of micrometer or even submicrometer size.[76] It relies on the excitation of intrinsic or extrinsic fluorescent markers, introduced through proper labeling protocols, and the collection of the signal they produce. Both the illumination and the imaging paths work by focusing light through regular lenses, a process restricted by diffraction that imposes a limit to the spatial resolution (Δr_{DL}), the minimal distance that two identical objects can be distinguished. This is the so-called diffraction barrier, and it is related to the wavelength of the light (λ) and the numerical aperture of the imaging lens (NA) by equation (1).

$$\Delta r_{DL} \approx \frac{0.61\lambda}{NA} \qquad (1)$$

The visible wavelengths involved in the fluorescence process and the best objective lenses available (NA ~ 1.4) set a value for Δr_{DL} to about half of the wavelength (*ca.* 200–300 nm). Thus, typical subcellular compartments with sizes below Δr_{DL} remain unresolved in conventional microscopies and important biological processes are impossible to be observed at the (bio) molecular level.
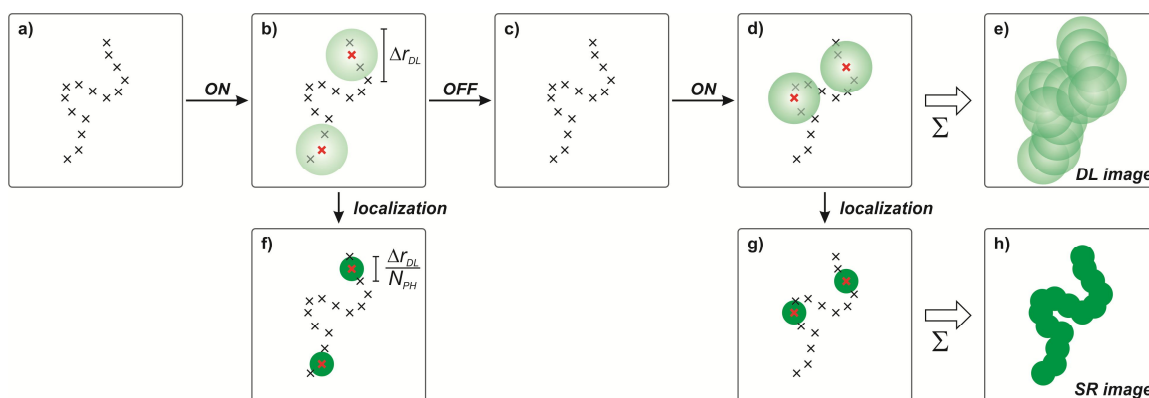
Figure 3.1. Superresolution imaging with SMLM. The crosses represent a series of markers labeling an object. Initially (*a*) all are driven to a dark state, and a few switched on to record a camera frame (*b*). Each emitting molecule appears with a size determined by the standard resolution of the microscope Δr_{DL}. Then, those molecules are switched off (*c*), to repeat the process and acquire the next frame (*d*). Software analysis is applied to each frame (*f*, *g*) to determine the position of the probes in the bright state, with a localization accuracy improved. The superresolution image is obtained by mapping the position of all localized markers (*h*). Superposition of all frames renders a wide-field image with diffraction limited resolution (*e*).

Modern and emerging techniques, such as STED,[109] PALM,[87] STORM,[86] GSDIM[110] and dSTORM,[89a] have taken advantage of the molecular states of the fluorescent probes not only for signal generation but also for overcoming the limits set by diffraction.[16,78] From the first successful realizations[111] to the present day, all the different techniques share in common the concept of switching the markers between an emissive and a dark state ($E\leftrightarrow D$).[78] The key is to switch the signal of the fluorescent probes on and off to achieve a temporal discrimination of subdiffraction-separated objects, *i.e.* features within a diffraction spot in the sample. One of these methods is based upon the detection and localization of single molecules (SMLM, single-molecule localization microscopies).[15] The imaging process consists of a simple sequence of steps (Figure 3.1). Initially all markers should be in the dark state (*D*) or switched off with light of an

appropriate wavelength (λ_{OFF}). Then a few of them are switched on ($D\rightarrow E$) in random

positions, usually by illumination with light of a defined wavelength λ_{ON}, to produce a

sparse subset of molecules in the bright state. It is critical at this stage that each emitter

can be resolved with a conventional wide-field (WF) microscope (*i.e.* average distance

between emitters found simultaneously in the bright state >> Δr_{DL}). An image is recorded

under illumination with λ_{EX} to elicit fluorescence, from which the position of each emitter

can be precisely obtained after proper image analysis with an accuracy

Δxy (equation (2)).[112]

$$\Delta xy = \sqrt{\frac{(\Delta r_{DL})^2}{N_{PH}} + \frac{a^2}{12N_{PH}} + \frac{8\pi(\Delta r_{DL})^4 b^2}{a^2(N_{PH})^2}} \approx \Delta r_{DL} \times (N_{PH})^{-1/2} \qquad (2)$$

N_{PH} is the number of detected photons, a is the pixel size in nanometers and b is the

background noise in photons. If an adequate pixelation is selected (*i.e.* $\approx \Delta r_{DL}$), and the

background is low, Δxy can be approximated with the right term in equation (2),

depending only on the detected number of photons and the resolution of the microscope.

Then, those markers are switched off again ($E\rightarrow D$) so the process is repeated by

switching on other markers. The superresolution image is reconstructed by mapping the

position of a large number of localized events, typically from several tens of thousands of

frames. It must be remarked that the transition from a diffraction-limited image of

resolution Δr_{DL} to a subdiffraction one with a resolution Δr_{SR} (equal to Δxy), is achieved

solely by the use of photoswitchable fluorophores instead of conventional ones. The

modulation of the fluorescence signal can also be performed with a three-state

irreversible molecular system. In this case, makers in the bright state are switched off to

another dark state (*i.e.* different from the initial one) through a photoinduced bleaching process ($D{\rightarrow}E{\rightarrow}D^*$). To distinguish these kinds of probes, reversible systems are usually referred to as photoswitchable markers and irreversible ones as photoactivatable markers.

The imaging scheme outlines the critical role of the molecular switches used as fluorescent probes,[113] in particular the photophysical properties of both states and the processes responsible for the control of signal modulation. Moreover, it also highlights the importance of finding different and alternative switching mechanisms at the molecular level, to expand the application range to varied samples and particular imaging case problems. The most remarkable qualities required for a suitable molecular switch are brightness and photostability of the emissive state, extremely high signal contrast between states, reliable photocontrol of the transitions involved and the ability to drive and maintain virtually all the ensemble of markers in the field of view to the dark state during the course of measurement.

Fluorescent proteins, both photoswitchable and photoactivatable, are a common family of markers for SMLM.[14] Their unique advantage is that they are genetically encoded. However, many of them exhibit low brightness or slow switching kinetics, and improvement of these key properties may require an arduous work of molecular cloning and engineering.[114] In contrast, the power of chemical synthesis can be extended with relative simplicity to organic fluorophores to prepare molecular switches with superior qualities.[21] Properly designed organic markers are brighter, present faster, more reliable switching and negligible cross-talk (defined as inducing activation with excitation light and vice versa).[14] Moreover, the size of the probe is becoming an additional issue to take

into account because resolutions on the order of the size of biomolecules are now at reach. In this regard, the average size of organic dyes is considerably smaller compared with that of fluorescent proteins, leading to higher labeling densities and thus to a better spatial resolution. To reach a certain resolution value, at least two labels should be placed within that distance, according to the Nyquist criterion.[102a] Despite several organic markers have been used in single-molecule localization microscopies, producing excellent images with high resolution (<20 nm), most of them rely on a few switching mechanisms.[14,102a,113] A frequent mechanism is the reversible interconversion between the emissive first singlet excited state and the corresponding nonemissive triplet state,[110] or radicals formed from the triplet,[90c] under illumination. These photoinduced transformations arise from the transient population of the ground singlet state and are observed as fluorescence blinking. A clear disadvantage of blinking microscopy is the need of higher light intensities and the use of chemical additives, usually a cocktail of redox species (e.g. ascorbic acid, methyl viologen and thiols such as cysteamine or β-mercaptoethanol) and oxygen scavengers (e.g. enzymatic systems). A cumbersome optimization is usually required for each dye, and they may be incompatible with many samples and measuring conditions. Another mechanism is the use of caged fluorescent compounds.[37a,48e,80] These molecules switch irreversibly from a nonemissive to an emissive state after the photoinduced cleavage of a protecting group. Such irreversible photoactivation events, however, prevent the localization of the same marker more than once. In addition, markers that are activated, but failed to be localized during the data analysis step, do not contribute to the superresolution image. Moreover, long time sequences or dynamic imaging are impossible. Nonetheless, uncaging reactions are

independent of environmental conditions, do not require the presence of additives (*i.e.* oxygen scavengers or thiols) and usually present a high contrast between the dark and the emissive state. A few examples of probes used in SML microscopies rely instead on photochromic transformations as the switching mechanism.[48a,50a] They are in fact the most promising markers because of their reversible character, the possibility to lower the irradiation intensities needed for the on- and off-switching processes and the opportunity to control and tune the properties of their interconvertible states independently.

In this chapter, I present successful application of two different triggering events, based on the photochromic[33c] and halochromic[33h] properties of **4a**, to achieve images with a spatial resolution beyond the diffraction limit. In the first one, photoisomerization of the oxazine is induced by direct irradiation of the chromophore. In the second one, the changes are indirectly triggered by the photoinduced uncaging of a proton from an auxiliary group. I demonstrate the potential of our approach by imaging polymer micelles, incorporating these photoswitchable compounds, *in vitro* as well as in cells.

3.2. Results and Discussions

3.2.1. Fluorescence Switching Strategies

Application of **4a** as a dual emission switch, either by direct photoisomerization or by indirect photoinduced proton transfer, requires readout with blue and green light, and two-channel detection. However, the complete absence of absorption of the closed isomer allows its simplified use as an on/off switch by readout excitation with *ca.* 530–580 nm, and detection only in a red channel ($\lambda > 660$ nm). An advantage of this readout strategy is that a virtually infinite contrast between states is achieved. In addition, markers that are in

the dark state do not contribute to the background signal, and unnecessary bleaching of them is avoided.
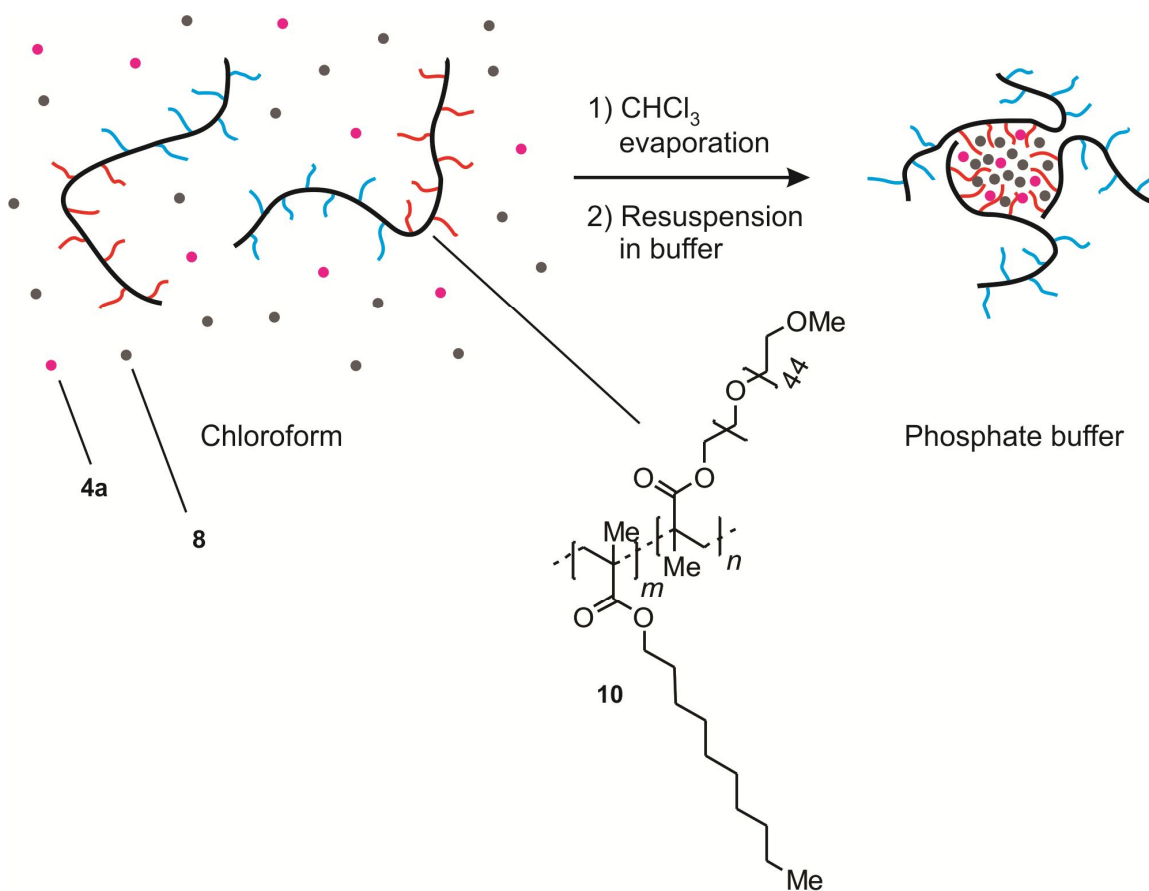
Figure 3.2. Schematic representation of the process used for the preparation of micelles, used as test object in SMLM, and the embedding of the photoactive markers in their core.

Modulation in the reversible strategy is achieved with UV light (≤355 nm) and the thermal natural recovery of the back isomerization. In the irreversible proton-induced one, photoactivation is achieved by irradiation at the absorption band of the cage compound (peaking at 355 nm), whereas bleaching with the same light source used for excitation accounts for the off-switching process. A key feature of both strategies is that the three driving processes can be tuned with a high degree of independence: (1) the rate

of the dark to bright transition is regulated by the intensity (or the dose) of UV or blue light irradiation; (2) photon extraction rate by the intensity of the green light used for excitation; (3) the rate of the bright to dark transition is fixed by the thermal reaction rate in the photochromism method, and by the pseudo–first-order constant of the bleaching process at the saturation intensity. Although the latter cannot be regulated, typical average times of residence in the bright state are on the order of a few tens of milliseconds. This imposes frame exposure times that are perfectly compatible with SMLM measurements (commonly used times range from 10 to 100 ms).[37a,80,89a,110]

There are some differences between the two strategies that must be evaluated for each particular application. The one based on photochromism has the advantage of being reversible, but requires the use of ultraviolet light, which may be phototoxic. Nevertheless, the relatively high isomerization efficiency of our compound (2%) demands very low intensities. The one based on the intermolecular proton transfer, is irreversible and requires an environment that allows proton diffusion (*i.e.* it does not work in a rigid matrix). However, it has the advantage that UV light can be avoided. The photoacid presents a considerable absorption in the violet region of the visible spectrum (the edge of the band), and, combined with a high uncaging efficiency, allows the use of a 405 nm diode laser at low intensities.

3.2.2. Superresolution Imaging

To implement the two switching strategies for imaging acquisition with a single-molecule localization approach, objects of nanoscale dimensions are necessary. Neither **4a** nor **8** have reactive groups to couple them with antibodies *via* immunolabeling protocols, or

surface staining polymer or silica nanoparticles. In addition, polar environments affect the emission of the coumarin, the photochromic behavior of the oxazine **4a**, and thermochromism can also compete with the photoinduced switching mechanism of the second. Therefore, I decided to incorporate the markers into an amphiphilic copolymer (**10**) that forms micellar structures in aqueous solvents (Figure 3.2).[108] The macromolecule used was copolymerized from two methacrylate monomers, decyl methacrylate and the other containing hydrophilic poly(ethylene glycol) side chains. In buffered (pH = 7.4) aqueous solutions, globular constructs are formed. These micellar structures have an average diameter of 15 nm, and thus are probably an assembly of three to four chains. Their hydrophobic core is capable of hosting different hydrophobic guests, in this case compounds **4a** or a mixture of **4a** and **8**, and is relatively permeable to facilitate proton diffusion between the two components involved in the intermolecular transfer.

A drop of buffer suspension of the micelles was spin coated onto coverslips, previously cleaned for 20–30 min in a commercial UV ozone cleaner and imaged in our home-made microscope. Imaging conditions were slightly varied depending on the sample. Micelles doped only with the photochrome–fluorophore marker were excited with green light with an intensity 5 kW cm^{-2}, activated with UV light of 10 W cm^{-2} in pulses of 100 μs–5 ms, and the exposure time of each frame was 10 ms. Micelles doped in addition with the caged compound were excited with an intensity 7 kW cm^{-2} and activated with violet light of 100 W cm^{-2} in pulses of 20 μs–2.5 ms, and the exposure time of each frame was 30 ms. The increment on the dose of light to induce switching was determined for each particular region of a sample. Typically 30,000–90,000 frames

were acquired; measurements were stopped when very few events were observed in a frame.
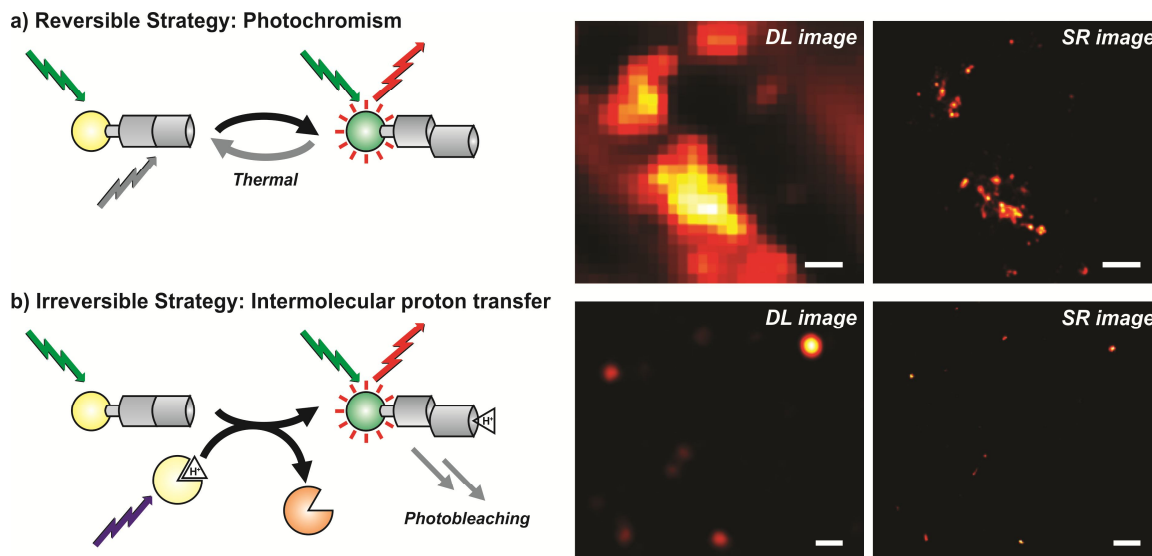
Figure 3.3. SMLM with switchable oxazines. Images obtained with the two proposed strategies are shown in the right panel. The resolution enhancement can be appreciated by comparing the diffraction-limited (*DL*) image with that obtained by localization (*SR*). All image bars are 500 nm.

Representative images obtained with the two different strategies are presented in Figure 3.3, showing the resolution enhancement obtained with both of them. Diffraction-limited images have a measured resolution of *ca.* 280–300 nm, estimated from line profiles of the WF image of single emitters. On the contrary, SMLM images have resolving powers of *ca.* 30 nm, calculated in the same manner, a value that is in agreement with equation (2). The 10-fold resolution increase allows the identification of features, even single micelles that are blurred in the conventional image.
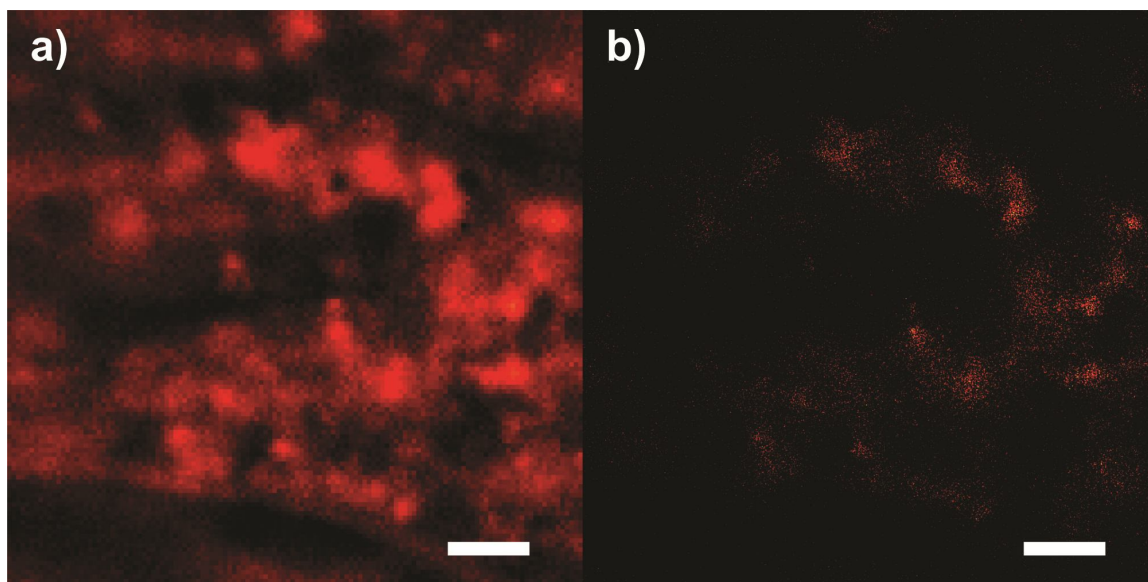
Figure 3.4. Wide-field (*a*) and superresolution (*b*) images of BHK cells that were fixed under identical conditions as cells used in Figure 3.5, but they were not incubated with the suspension containing the micelles. The intensity scale in the superresolution image is reduced (0-7 events) compared with *b* in Figure 3.5 (0-40 events), because there are few activation events in this case, as the switchable dye is absent. These few detected events correspond to nonspecific activation or spontaneous emission of other molecules present in the sample. Bars are 1 μm (*a*, *b*)

The micellar structures prepared here have been used as efficient supramolecular assemblies for intracellular delivery of insoluble and potentially toxic compounds. In fact, Trypan Blue staining showed that cell viability after exposure to the structures remains unaltered, confirming their lack of cytotoxicity.[108] To test the feasibility of our approach in model biological samples, baby hamster kidney cells (BHK) were incubated in complete culture medium containing a suspension of the micelles, loaded only with **4a**; in parallel, control cells (Figure 3.4) were kept in complete medium in absence of micelles. After overnight incubation and three cycles of media exchange to remove micelles free in solution, cells were fixed with MeOH to reduce the background signal

and to prevent cell movement during image acquisition. Figure 3.5 shows one image obtained with the reversible switching strategy.
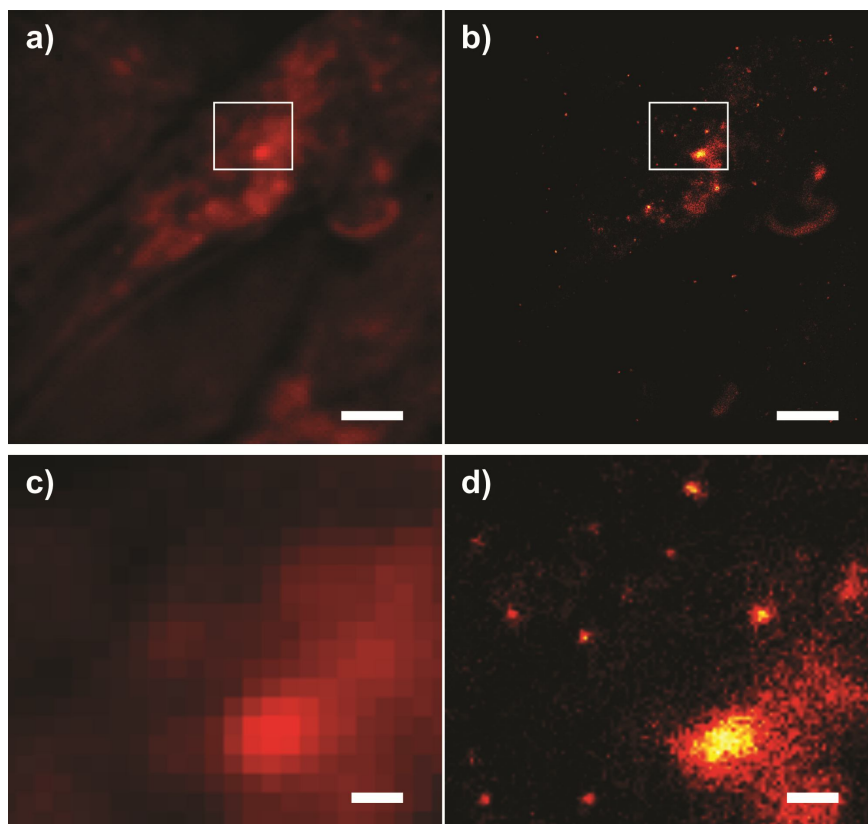
Figure 3.5. Wide-field (*a*, *c*) and superresolution (*b*, *d*) images of BHK cells treated with a suspension of water-compatible micelles containing the oxazine. The enlarged areas (*c*, *d*) show the resolution enhancement achieved by SMLM, allowing the detection of discrete structures where the micelles are trapped inside the cells. Bars are 2 µm (*a*, *b*) and 300 nm (*c*, *d*).

The wide-field images show a rather homogeneously distributed signal inside the cells that is attributable to **4a**, whereas control cells lack any significant signal. In contrast, the subdiffraction images reveal the presence of discrete, punctuate structures; most of these features are inside the cells, although a few are also present outside, possibly because of unspecific micelle attachment to the glass surface. The punctuate

structures are consistent with the uptake of the micelles in the cellular milieu *via* the endocytic pathway,[115] and they provide a means to estimate the dimensions of the intracellular vesicles in which they are confined. The size of the features is well below the diffraction limit, within the 65–80 nm range, proving a significant resolution enhancement with the oxazine system in cell imaging applications.

3.3. Conclusions

The signal modulation of a fluorescent coumarin dye, induced by electronic changes of a [1,3]oxazine, was implemented to achieve far-field images with a resolution well beyond the diffraction limit. Two different switching strategies were applied, based on distinct phototriggering, both requiring low light intensities. Spatial resolutions down to 30 nm were achieved *in vitro* and inside cells. The principle is straightforward and can be extended to other fluorophores to increase the emission efficiency of the bright isomer as a means to improve the spatial resolution even further. Indeed, this would be mandatory for this type of markers to work in similar superresolution microscopies in three dimensions, or in samples presenting larger background signals. The switchable oxazine **4a** can be incorporated into live cells with the aid of the polymer micelles, and provides an effective way to investigate drug delivery and intracellular trafficking at the subdiffraction level. In addition, dye functionalization with reactive groups can be implemented in the future for alternative labeling or targeting strategies, in particular for biological applications.

CHAPTER 4

SYNTHESIS AND PROPERTIES OF AN OXAZINE AUXOCHROME BASED ON 2-NITROBENZYL GROUP

4.1. Overview

Organic molecules can be designed to undergo pronounced structural changes in response to external stimulations.[116] In turn, these switching events can be exploited to control motion at the molecular level as well as to regulate the electrochemical and spectroscopic signatures of multicomponent assemblies.[117] Indeed, molecular switches are becoming valuable building blocks for the construction of a diversity of functional materials with controllable properties. In particular, photochromic switches offer the opportunity to implement such structural transformations reversibly under the influence of light.[51-56] Specifically, molecular switches containing 2*H*,3*H*-indole and 2*H*,4*H*-benzo[1,3]oxazine heterocycles in their molecular skeletons, have attracted particular attention. Upon ultraviolet illumination, the [C–O] bond at the junction of the two heterocycles cleaves on a subnanosecond timescale. The photoinduced bond cleavage opens the oxazine ring and generates a phenolate chromophore and a *3H-* indolium cation. As a result, this photochemical process is accompanied by the appearance of an absorption band in the visible region of the electromagnetic spectrum. The photogenerated isomer, however, reverts spontaneously to the original one on a submicrosecond timescale. Indeed, these molecules can be switched back and forth between their two interconvertible states hundreds of times with no sign of degradation, even in the presence of molecular oxygen. In fact, the ability to photoregulate this isomerization has already translated into the realization of photoresponsive molecular constructs based on photochromic components.[118-121]

The photoinduced opening (from *a* to *b* in Figure 4.1) of the oxazine ring of our photochromic compounds generates a zwitterionic isomer incorporating a phenolate anion and a 3*H*-indolium cation.[33a,b,122,123] This transformation can be exploited to perturb the electronic structure of a chromophoric appendage attached to the chiral center at the junction of the two heterocycles (R in Figure 4.1). As a result, it is possible to modulate the absorption, emission and redox properties of a chromophore attached to it. However, strategies to mimic these results irreversibly, under the influence of light are not explored. Such irreversible photoactivation events can be highly complementary to the existing photochromic triggering events. Furthermore, it provides the user the choice to pick the one that is suitable for the application under consideration. Indeed, this chapter reports the implementation of a mechanism for irreversible ring opening of an oxazine auxochrome based on 2-nitrobenzyl group and presents a representative example for fluorescence activation.
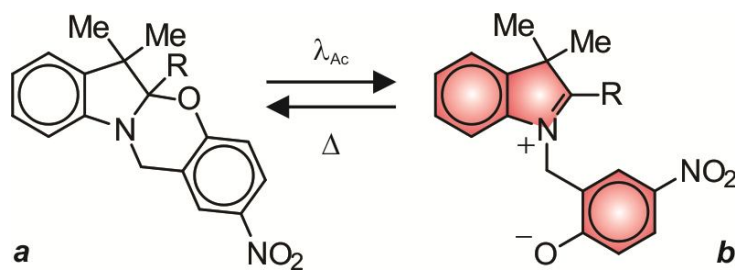
Figure 4.1. Reversible opening of an oxazine ring (*a*) to form a zwitterionic isomer (*b*) under illumination at an activating wavelength (λ_{Ac}).

4.2. Results and Discussions

4.2.1. Design and Synthesis

Literature data suggest that 2-nitrobenzyl groups have been widely used as photoremovable protecting groups (PPG) for many years.[27] Upon illumination at an appropriate wavelength, (usually, 365nm) they get converted into 2-nitrosobenzaldehyde with concomitant release of a proton.[33f] They are usually employed to release important bioactive reagents upon illumination at the right wavelength. However, the established photochemistry of 2-nitrobenzyl groups can be used to our advantage to open the ring of an oxazine auxochrome irreversibly under the influence of light, by careful structural design. Therefore, I designed compound **11** (Figure 4.2) in such a way that the irradiation of **11** at an activation wavelength (λ_{Ac}) will result in the formation of **12** and **13** (Figure 4.2). This structural transformation is analogous to the one seen in the reversible strategy in that both of them generates a carbon nitrogen double bond. Once again, this can be exploited to modulate the absorption, emission and redox properties of a chromophore attached to it. Therefore, I developed a synthetic protocol to prepare compounds **11** and **16** (Figure 4.3). Specifically, reaction of 2-methyl-3-nitroanisole with *N*-bromosuccinimide resulted in the formation of the corresponding benzyl bromide (**14**) which upon treatment with BBr$_3$ yielded the corresponding phenol (**15**). The treatment of **15** with **12** resulted in the formation of the desired oxazine **11** (Figure 4.3). X-Ray diffraction analysis (Table 4.1) of single crystals of the product clearly indicates the oxazine core of this molecule together with the nitro substituent in the *ortho*-position, relative to the benzyl group (Figure 4.4). Compound **16** was obtained by condensing the aldehyde **17** with **11** in acetonitrile in the presence of TFA to envisage the possibility of

activating the fluorescence of the coumarin appendage using the photoinduced ring opening of **11**.
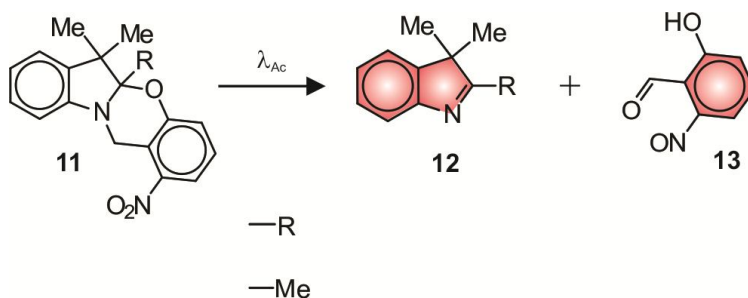
Figure 4.2. Irreversible opening of the oxazine ring of **11** to form **12** and **13** under illumination at an activating wavelength (λ_{Ac}).
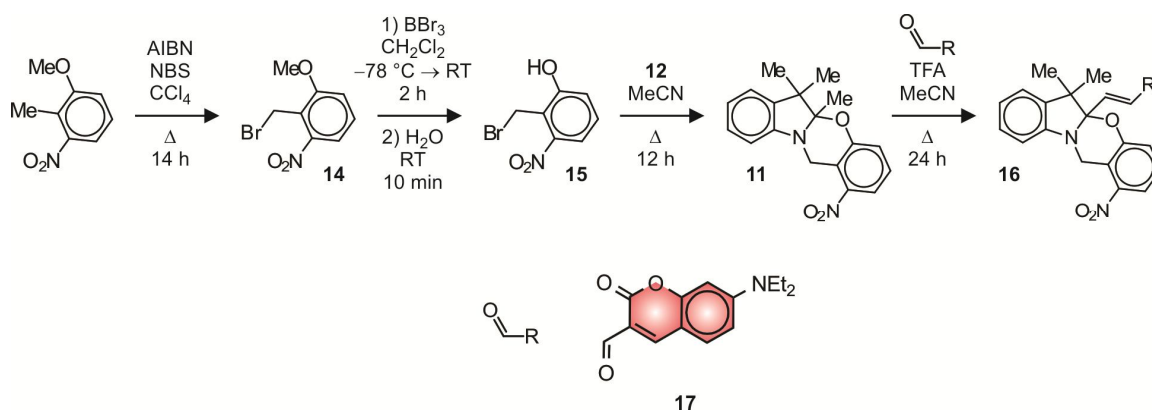
Figure 4.3. Synthesis of **11** and **16**.
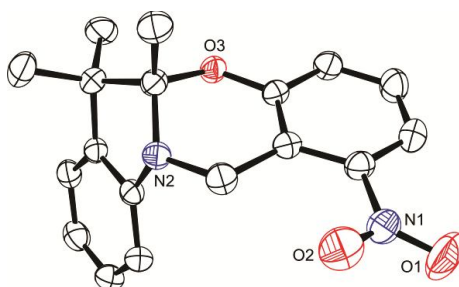
Figure 4.4. ORTEP representation of the geometry adopted by **11** in single crystals, showing 40% thermal ellipsoid probability.

Table 4.1. Crystallographic Data for **11**.

Empirical Formula	$C_{18}H_{18}N_2O_3$
Formula Weight	310.34
Crystal System	Monoclinic
Lattice Parameters:	
a (Å)	8.2502(3)
b (Å)	17.5045(6)
c (Å)	11.1549(4)
β (°)	105.933(1)
V (Å^3)	1549.05(10)
Space Group	$P2_1/n$ (# 14)
Z Value	4
ρ_{calc} (g cm^{-3})	1.331
μ (Mo Kα) (mm^{-1})	0.092
T (K)	296
$2\Theta_{max}$ (°)	54.0
No. Obs. (*I* > 2σ(*I*))	3046
No. Parameters	212
Goodness of Fit	1.043
Max. Shift in Cycle	0.001
Residuals*: R1; wR2	0.0392; 0.1063
Absorption Correction,	Multi-scan
Max/min	0.9819/0.9556
Largest Peak in Final Diff. Map (e$^-$ Å^{-3})	0.201

* $R = \Sigma_{hkl}(||F_{obs}| - |F_{calc}||)/\Sigma_{hkl}|F_{obs}|$; $R_w = [\Sigma_{hkl}w(|F_{obs}| - |F_{calc}|)^2/\Sigma_{hkl}wF_{obs}^2]^{1/2}$,

$w = 1/\sigma^2(F_{obs})$; $GOF = [\Sigma_{hkl}w(|F_{obs}| - |F_{calc}|)^2/(n_{data} - n_{vari})]^{1/2}$.

4.2.2. Absorption Spectroscopy and HPLC Analysis

The absorption spectra of **11** recorded before and during the course of irradiation at λ_{Ac} in acetonitrile, reveal a decrease in the absorbance associated with the 3-nitrophenol group of **11** at 240 nm and the concomitant appearance of new bands at *ca*. 260 nm and at *ca*. 400 nm (Figure 4.5). The very same band at 260 nm is present in the absorption spectrum recorded in acetonitrile for a pure sample of **12** purchased from commercial sources (*a* in Figure 4.5). Thus, irradiation of **11** at λ_{Ac} results in the formation of **12** and the byproduct **13**. Indeed, the band at 260 nm indicates the formation of **12** while that at 400 nm corresponds to **13**. Our interpretation was further confirmed by the HPLC analysis of solutions of **11** in acetonitrile before and after irradiation at λ_{Ac} (Figure 4.6). Specifically, samples of **11** in acetonitrile before and during the course of irradiation were injected along with a benzophenone standard into an Agilent Microsorb 100-5 BDS column (4.6 × 250 mm) with a flow rate of 1mL/min and a mobile phase containing MeCN/H_2O (60:40, v/v). The chromatograms obtained for the sample before irradiation, displayed a peak for the benzophenone standard and **11** at retention times (RT) 6.6 min and 13 min respectively. The chromatograms obtained after subsequent injections of samples during the course of irradiation (Figure 4.6, 5-20 min) indicate a decrease in the intensity of the peak at 13 min and an increase in the intensity of a new peak at 4.3 min. The HPLC chromatogram of **12** obtained from commercial sources also shows the very same peak at RT 4.3 min (not shown). This, once again, is in agreement with our interpretation that the irradiation of **11** results in the formation of **12.** However, a peak for the byproduct **13** could not be found. Presumably, its molar extinction coefficient at 250 nm is too low to be detected. The HPLC analysis also reveals that the quantum yield for the

photochemical conversion of **11** to **12** is 0.043, which is consistent with the literature

findings for similar 2-nitrobenzyl derivatives.[27]
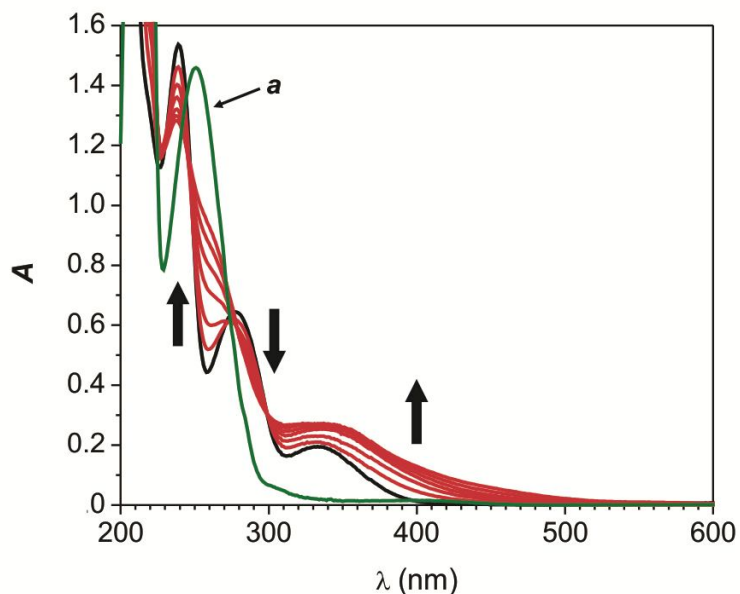
Figure 4.5. Absorption spectra recorded sequentially with a delay of 5 min before and during the photolysis (350 nm, 4.88 mW cm^{-2}) of a solution of **11** (0.1 mM, MeCN, 25 °C) for 30 min. Absorption spectrum (*a*) of a solution of **12** (0.1mM, MeCN, 25°C).
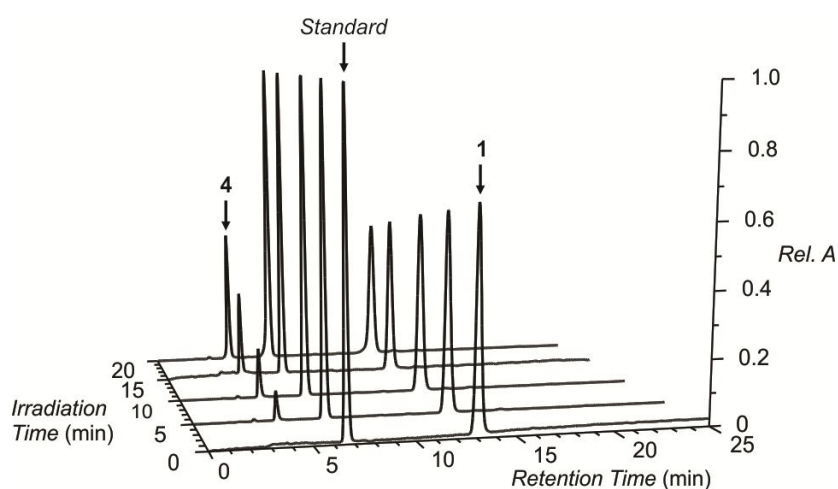
Figure 4.6. HPLC traces [1.0 mL min^{-1}, BDS, MeCN/H$_2$O (60:40, v/v), 250 nm] recorded before and during the photolysis (350 nm, 4.88 mW cm^{-2}) of a solution of **11** (0.1 mM, MeCN, 25 °C).

The absorption spectra of **16** recorded before (*a* in Figure 4.7) and during (*b-e* in Figure 4.7) the course of irradiation at λ_{Ac} in acetonitrile, reveal a significant decrease in the absorbance associated with the coumarin appendage at *ca.* 410 nm and a concomitant appearance of a new band, albeit very small, at *ca.* 600 nm (Figure 4.7). This indicates that the resulting photoproduct is not stable enough under the employed conditions and that it decomposes considerably. Presumably, the byproduct **13** (nitrosobenzaldehyde) of the photolysis of **11** undergoes a [2+2] cycloaddition with the double bond of the coumarin appendage. These results suggest that the coumarin fluorophore is not the ideal one for this system and that other fluorophores need to be explored.
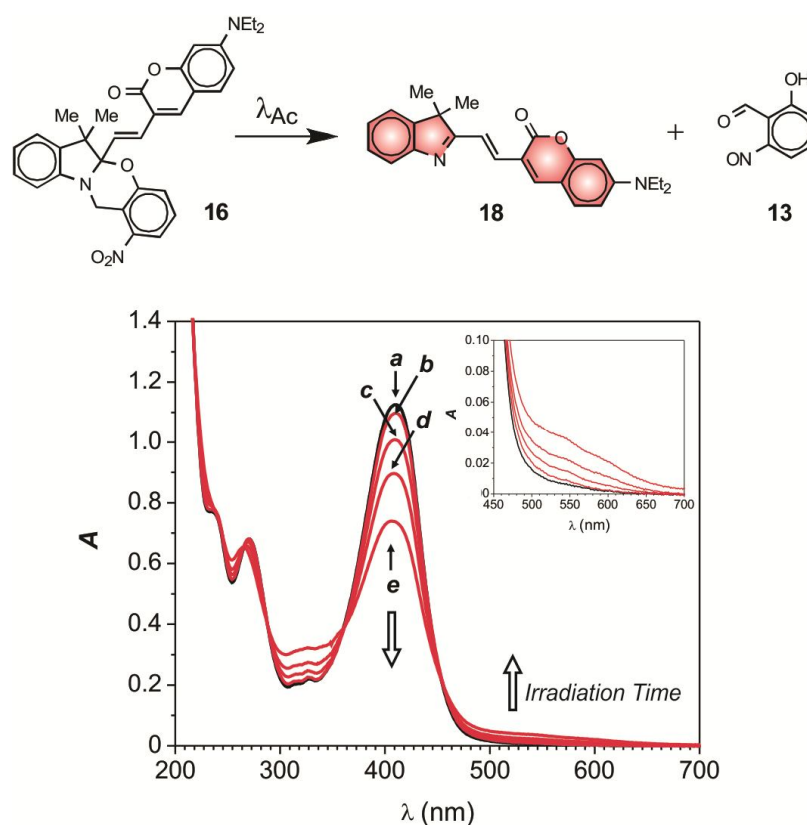
Figure 4.7. Absorption spectra of a solution of **16** (0.1 mM, MeCN, 25 °C) recorded before (*a*) and after irradiation (λ_{Ac} = 350 nm, 4.88 mW cm^{-2}) for 5 (*b*), 15 (*c*), 30 (*d*) and 60 min (*e*).

4.2.3. Square Wave Voltammetry

The photochemical transformation of **11** to **12** also offers the opportunity to develop molecular constructs whose redox potentials can be altered based on the photoinduced ring opening reaction of the oxazine auxochrome. Therefore, the photochemical reaction was monitored through electrochemical measurements. Specifically, the square wave voltammogram of **11** in acetonitrile before irradiation has an oxidation potential at +0.83 V corresponding to the oxidation of the N atom of the oxazine ring. However, the very same peak decreases in intensity and disappears completely with an appearance of a new peak at +0.55 V after 10 min and 20 min of irradiation at λ_{Ac} respectively (Figure 4.8). The decrease in potential is consistent with the removal of the nitro group from the oxazine auxochrome after irradiation. Nitro group, being an electron withdrawing group makes it difficult to remove an electron from the N atom of the oxazine ring at lower potentials. However, after irradiation, the photochemical conversion results in the loss of the nitro group, resulting in a lesser oxidation potential (+0.55 V). Furthermore, an additional oxidation peak at +1.30 V was found, corresponding to the oxidation of the phenol group of the byproduct **13**. The square wave voltammogram of **11** before irradiation has a reduction potential at −1.42 V corresponding to the reduction potential of the nitro group of the oxazine moiety (Figure 4.8). Upon irradiation at $\lambda_{Ac,}$ the reduction peak at −1.42 V disappears completely and a new peak appears at −1.17 V. This peak corresponds to the reduction of the nitroso group present in the byproduct **13**.[124-127] Once again, these results confirms the photoinduced generation of **12** and **13** from **11**.
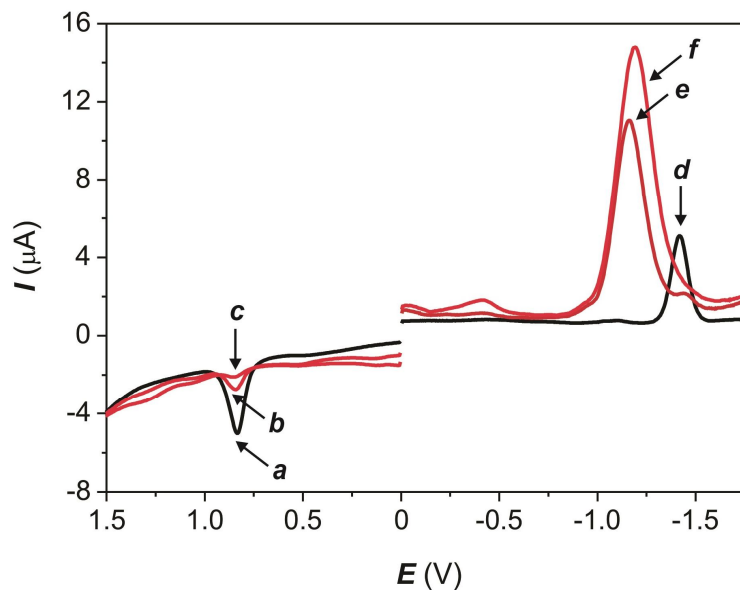
Figure 4.8. Square wave voltammograms of **11** (100 μM, MeCN, 25 °C, [TBAPF$_6$] = 0.1 M, v = 100 mV s^{-1}) before (***a*** and ***d***) and after irradiation (λ_{Ac} = 350 nm ,4.88 mW·cm^{-2}) for 10 (***b*** and ***e***) and 20 min (***c*** and ***f***)

4.3. Conclusions

A strategy for the irreversible opening of an oxazine auxochrome was designed based on the photochemistry of 2-nitrobenzyl group. The photoinduced ring opening of the oxazine was monitored by absorption spectroscopy, HPLC and electrochemistry. The very same ring opening reaction can also be exploited to manipulate the redox potentials of the auxochrome and can possibly lead to the development of novel photoresponsive molecular constructs. A fluorophore-auxochrome dyad was also synthesized and the fluorescence activation of the appended fluorophore was explored. The results indicate that the byproduct generated from the photolysis of the oxazine auxochrome reacts with the appended fluorophore under the conditions employed leading to undesired results. Currently, other fluorophores are being explored.

CHAPTER 5

ACTIVATION OF BODIPY FLUORESCENCE BY THE PHOTOINDUCED DEALKYLATION OF A PYRIDINIUM QUENCHER

5.1. Overview

The borondipyrromethene (BODIPY) platform offers outstanding photophysical properties in conjunction with long-term stability and synthetic versatility.[128-132] In fact, established synthetic protocols permit the manipulation of the substituents on the two pyrrole rings as well as on the boron and carbon atoms joining the two heterocycles. In turn, such structural modifications can be exploited to regulate the spectroscopic signature of the BODIPY chromophore and produce molecules able to emit light across the visible region with quantum efficiencies approaching unity. In addition, the synthetic accessibility of these derivatives permits the integration of the BODIPY skeleton into a diversity of multicomponent molecular and supramolecular constructs. Indeed, BODIPY chromophores have become valuable building blocks for the assembly of electroluminescent materials, fluorescent probes, laser dyes, light harvesters and sensitizing agents.

In spite of the remarkable combination of attractive properties associated with the BODIPY platform, mechanisms to photoactivate its fluorescence remain limited to one representative example.[29] Molecules able to switch from a nonemissive to an emissive state under illumination at an activating wavelength, however, offer the opportunity to switch fluorescence on exclusively within a defined region of space at a given interval of time. Such spatiotemporal control of fluorescence can translate into the possibility of monitoring dynamic events in real time[1,2,4,8-13] as well as recording images with

resolution at the nanometer level.[14-21] Indeed, these attractive prospects are stimulating the identification of photochemical strategies to activate the emission of organic dyes.[3,5-7,26,27] In fact, several examples of photoactivatable coumarins,[30-34] diarylethenes,[35-36] dihydrofurans,[37a,b,d] fluoresceins,[38-45] rhodamines[44,46-49] and spiropyrans[50] have been developed already, relying on either photocleavable protecting groups or photochromic transformations. Structural designs to extend these operating principles for fluorescence switching also to BODIPY chromophores can be a valuable addition to this emerging field of study and might lead to the realization of versatile photoactivatable probes with improved photophysical properties. This chapter presents the implementation of operating principles for BODIPY photoactivation with a representative example.

5.2. Results and Discussion

5.2.1. Design and Synthesis

Literature data demonstrate that the introduction of a 1-alkylpyridinium-4-yl substituent on the *meso* position of the BODIPY skeleton results in fluorescence suppression.[133,134] In these molecular constructs, the excitation of the BODIPY chromophore is followed by the transfer of one electron to the pyridinium appendage. This process deactivates nonradiatively the excited BODIPY platform and quenches its fluorescence effectively. By contrast, the presence of a pyrid-4-yl ring in the very same position has negligible influence on the emissive behavior of the BODIPY chromophore, which retains its fluorescence with high quantum efficiency. These observations suggest that the photoinduced dealkylation of a pyridinium quencher can be exploited to activate

the fluorescence of a BODIPY chromophore under optical control. Therefore, I decided to synthesize compounds **19** and **20** (Figure 5.1).

Compound **20** has a photocleavable 2-nitrobenzyl group on the pyridinium-4-yl quencher attached to the *meso* position of a BODIPY chromophore. Its hexafluorophosphate salt can be isolated in a yield of 17%, after the *N*-alkylation of the pyrid-4-yl appendage of **19** with (1-bromomethyl)-4,5-dimethoxy-2-nitrobenzene (Figure 5.1) and counterion exchange.
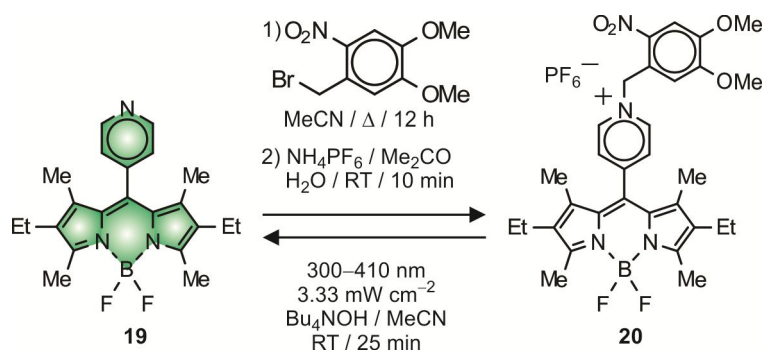
Figure 5.1. Synthesis of the hexafluorophosphate salt of **20** from **19** and photoinduced generation of the latter from the former.

5.2.2. Absorption and Emission Spectroscopy

The steady-state absorption spectrum (*a* in Figure 5.2) of compound **19** shows a band for the BODIPY chromophore at 526 nm in acetonitrile at 25 °C. Upon illumination at an excitation wavelength positioned within this band, the characteristic BODIPY fluorescence appears in the emission spectrum (*b* in Figure 5.2) at 545 nm with a quantum yield of 0.50, in agreement with literature data.[133a]
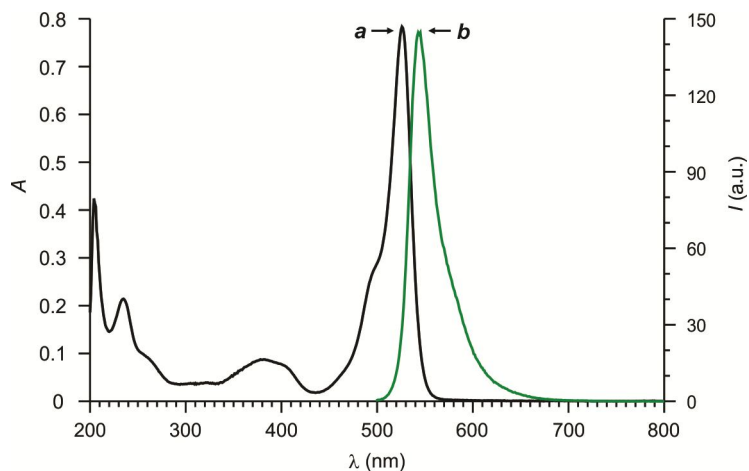
Figure 5.2. Absorption (*a*) and emission (*b*) spectra of **19** (10 μM, MeCN, 25 °C, λ_{Ex} = 470 nm).

The absorption spectrum (*a* in Figure 5.3) of the hexafluorophosphate salt of **20** reveals a band for the BODIPY chromophore at 534 nm. In contrast to the behavior of **19**, however, illumination at an excitation wavelength positioned within this band does not produce any significant fluorescence (*b* in Figure 5.3). The drastic difference between the emission spectra of the two compounds demonstrates that the cationic pyridinium-4-yl appendage of **20** quenches the excited state of the adjacent BODIPY component, in agreement with literature observations on similar compounds.[133,134] Nonetheless, the characteristic emission band (*c–g* in Figure 5.3) of **19** develops upon ultraviolet illumination of **20**.[135] The photoinduced enhancement in fluorescence is indicative of the cleavage of the 2-nitrobenzyl group from the nonemissive species **20** (Figure 5.1) with the concomitant formation of its emissive counterpart **19**. The temporal evolution of the integrated emission intensity (*a* in Figure 5.4) under irradiation, in the presence of a proton scavenger, indicates the quantum yield for this photochemical transformation to be 0.001. This value is consistent with the quantum efficiencies reported in the literature for the photoinduced cleavage of the very same 2-nitrobenzyl group from a diversity of

compounds.[27] By contrast, the emission intensity (*b* in Figure 5.4) of an identical solution maintained in the dark over the very same period of time does not change, demonstrating that irradiation is essential to activate fluorescence.
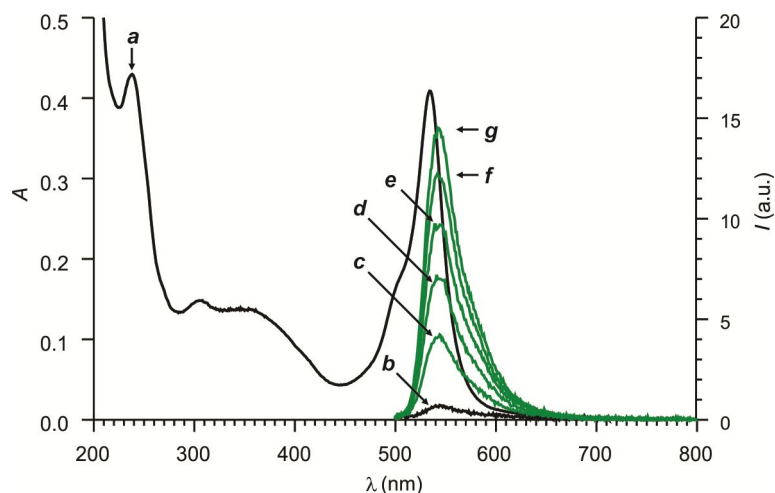
Figure 5.3. Absorption (*a*) and emission (*b*) spectra of an equimolar solution of the hexafluorophosphate salt of **20** and Bu$_4$NOH (10 μM, MeCN, 25 °C, λ_{Ex} = 470 nm). Emission spectra of the same solution after irradiation (350 nm, 3.33 mW cm^{-2}) for 5 (*c*), 10 (*d*), 15 (*e*), 20 (*f*) and 25 min (*g*).

The photochemical transformation of the 2-nitrobenzyl group of **20** into the corresponding 2-nitrosobenzaldehyde is accompanied by the release of a proton.[33f] In turn, the protonation of the pyrid-4-yl appendage of **19** is known to quench the emission of the adjacent BODIPY fluorophore.[133b] Furthermore, the literature value (2.8 × 10^5 M^{-1}) of the association constant for the protonation of **19** in acetonitrile indicates that *ca.* 50% of this compound is protonated at the concentration of the photolysis experiment, in the absence of a proton scavenger. Indeed, the evolutions of the integrated emission intensity during the photolysis of **20** in the presence (*a* in Figure 5.4) and absence (*c* in Figure 5.4) of one equivalent of tetrabutylammonium hydroxide are significantly different. Specifically, this particular base scavenges the photogenerated

protons and prevents the protonation of the emissive species, ensuring a twofold increase in fluorescence.[136] Furthermore, identical solutions with (***b*** in Figure 5.4) and without (***d*** in Figure 5.4) base, maintained in the dark, do not reveal any change in the integrated emission intensity over the same period of time of the photolysis experiments. These observations confirm, once again, that ultraviolet irradiation is essential to activate fluorescence and that the presence of base alone has no influence of the emission behavior.
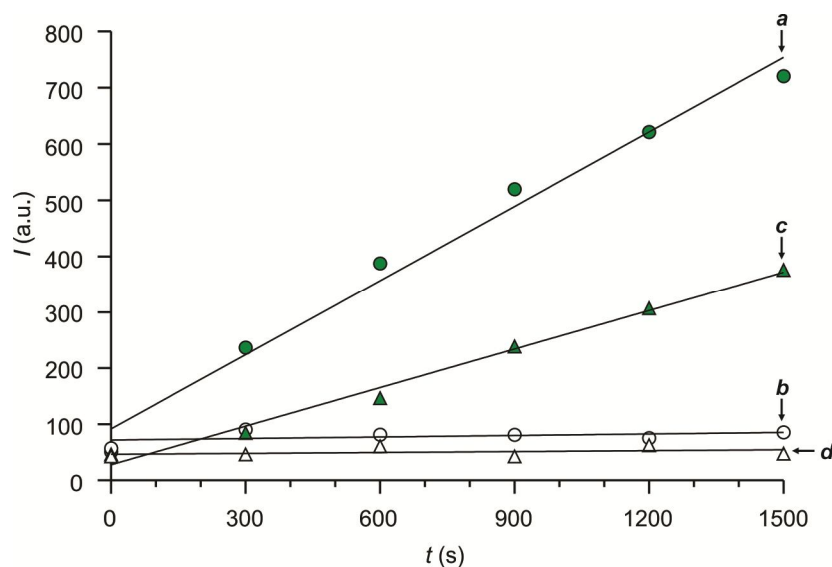
Figure 5.4. Evolution of the integrated emission intensity detected for solutions of the hexafluorophosphate salt of **20** (10 µM, MeCN, 25 °C, λ_{Ex} = 470 nm) with (***a*** and ***b***) or without (***c*** and ***d***) Bu$_4$NOH (1 eq) under irradiation (***a*** and ***c***, 350 nm, 3.33 mW cm^{-2}) or in the dark (***b*** and ***d***).
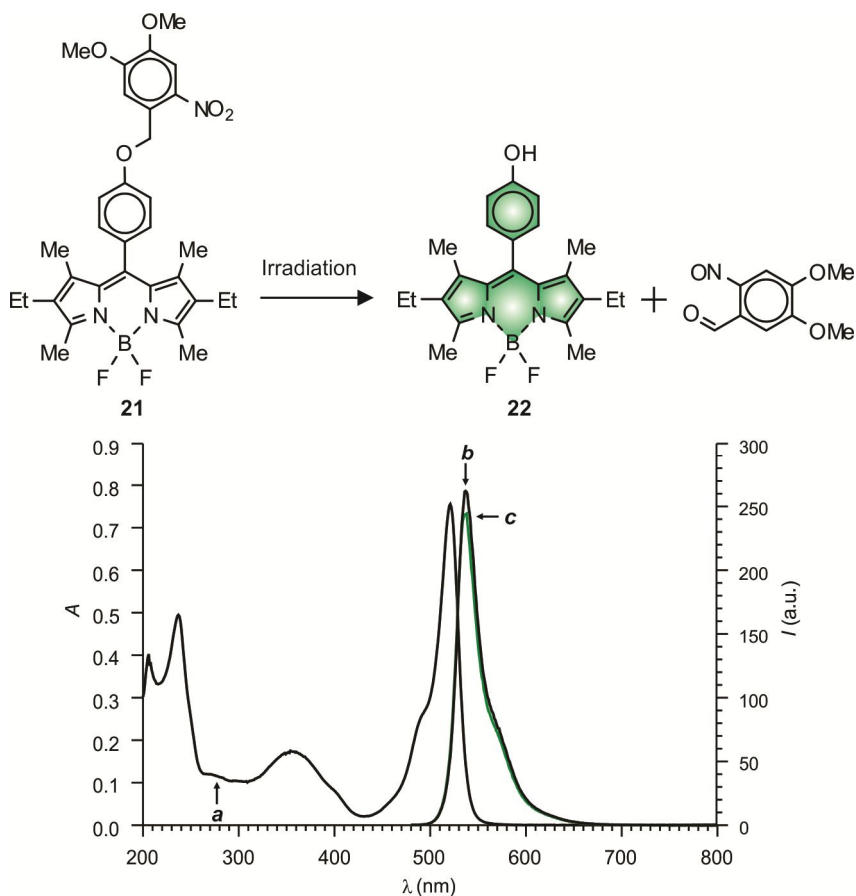
Figure 5.5. Absorption (*a*) and emission (*b*) spectra of a solution of **21** (10 μM, MeCN, 25 °C, λ_{Ex} = 470 nm). Emission spectrum (*c*) of the same solution after irradiation (350 nm, 3.33 mW cm^{-2}, 30 min).

The close proximity of nitro groups to the BODIPY skeleton is known to have a depressive effect on the quantum efficiency of the emission process.[42] Therefore, a photochemical conversion that leads to the removal of the nitro group from the proximity of a BODIPY chromophore can be exploited to activate its fluorescence. Based on this consideration, the photocleavable 2-nitrobenzyl appendage was connected to the *meso* position of a BODIPY chromophore through a 1-oxyphen-4-yl spacer in the shape of compound **21**. The corresponding absorption spectrum (*a* in Figure 5.5) shows the characteristic absorption of the BODIPY chromophore. In this instance, however,

excitation at a wavelength positioned within this band results in significant fluorescence (*b* in Figure 5.5). In addition, the emission spectrum of this system does not change upon ultraviolet irradiation (*c* in Figure 5.5), despite the photoinduced transformation of **21** into **22**. Thus, the removal of the nitro group from the environment surrounding the emissive chromophore has negligible influence on the excitation dynamics of this particular BODIPY derivative.

5.2.3. Ensemble Imaging

The enhancement in emission intensity associated with the photoinduced transformation of **20** into **19** is also evident from a fluorescence image (Figure 5.6) of the corresponding acetonitrile solution, recorded under simultaneous illumination with a pair of independent lasers. Specifically, the irradiation of an ellipsoidal area (*a* in Figure 5.6) within the imaging field at 476 nm results in negligible fluorescence. By contrast, the illumination of an identical and adjacent area (*b* in Figure 5.6) at 405 nm produces significant fluorescence. Indeed, the laser operating at 476 nm can only excite the resulting nonemissive BODIPY of **20**, while that at 405 nm can first cleave the 2-nitrobenzyl group of **20** and then excite the emissive BODIPY of **19**. Consistently, the ratio between the integrated emission intensities of the two areas indicates an eightfold enhancement in fluorescence with excitation at 405 nm, under these experimental conditions.
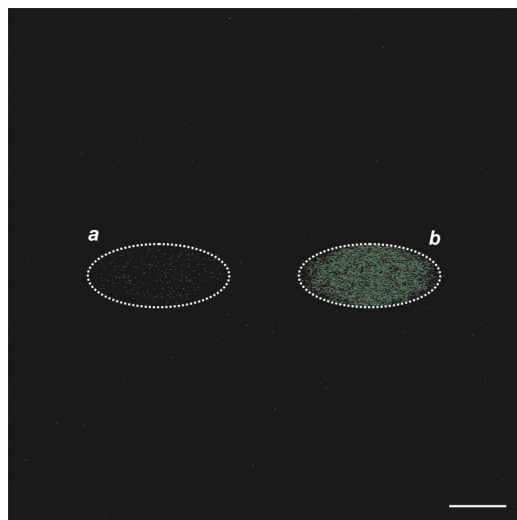
Figure 5.6. Confocal laser-scanning fluorescence image (λ_{Em} = 500–700 nm, scale bar = 100 µm) of a solution of the hexafluorophosphate salt of **20** (10 µM, MeCN, 25 °C) recorded upon exclusive illumination of two ellipsoidal areas within the imaging field at 476 (a) and 405 nm (b) respectively.

5.3. Conclusions

These results demonstrate that the attachment of a photocleavable quencher, in the form of a pyridinium cation, to the meso position of a BODIPY platform translates into the assembly of a photoactivatable fluorophore. Indeed, the photoinduced conversion of the pyridinium-4-yl quencher into a pyrid-4-yl appendage prevents the electron-transfer process responsible for quenching the BODIPY emission and, hence, activates fluorescence. As a result, these viable operating principles for the photochemical manipulation of excitation dynamics, coupled to the synthetic accessibility of such structural design, can lead to the development of an entire family of photoactivatable fluorophores based on the outstanding photophysical properties of BODIPY chromophores.

CHAPTER 6

FLUORESCENCE PHOTOACTIVATION BY LIGAND EXCHANGE AROUND THE BORON CENTER OF A BODIPY CHROMOPHORE

6.1. Overview

Fluorescence recovery after photobleaching[64] (FRAP) has been exploited successfully to probe the diffusion of molecules in biological specimens as well as to monitor the flow of liquids in microstructured channels. However, the implementation of FRAP schemes demands relatively high irradiation intensities to bleach the fluorescent species and turn their emission off. Instead, photoactivatable fluorophores can be switched on with moderate activation intensities and, therefore, are a valuable alternative to FRAP in the investigation of dynamics at the microscopic level.

The unique combination of photochemical and photophysical properties of photoactivatable fluorophores can also be exploited to overcome the limitations that diffraction imposes on the resolving power of fluorescence microscopes.[15,16,18-21] The prospects of monitoring dynamics and overcoming diffraction are stimulating the design of mechanisms to photoactivate fluorescence with the main families of organic fluorophores.[3,5-7,26,27] Generally, these operating principles rely on either the photoinduced cleavage of a protecting group from an emissive chromophore or a photochromic transformation. In both instances, significant fluorescence is observed only after the formation of the photochemical product. Indeed, several examples of photoactivatable coumarins,[30b,31b,32,33c] fluoresceins[38-45] and rhodamines[44,46,47,48d,49] have been developed already on the basis of these mechanisms. By contrast, only two strategies to photoactivate the emission of the BODIPY chromophore have been reported

so far and they are both based on the photoinduced cleavage of 2-nitrobenzyl quenchers.[29,138] The BODIPY skeleton, however, offers outstanding photophysical properties together with synthetic accessibility.[128-130,132] Therefore, the identification of structural designs to activate the fluorescence of this versatile organic chromophore can translate into the realization of valuable photoactivatable probes for a diversity of imaging applications. Indeed, this chapter reports the implementation of a mechanism for fluorescence activation based on the photoinduced exchange of the ligands connected to the BODIPY fluorophore.

6.2. Results and Discussion

6.2.1. Design and Synthesis

Spectroscopic data from our[139] and other[140] laboratories demonstrate that the replacement of the two fluorine ligands on the boron center of the BODIPY platform with a catecholate chelator suppresses fluorescence completely. These observations suggest that the manipulation of the groups attached to this particular atom can be exploited to regulate the emissive behavior of the overall chromophore and, possibly, activate fluorescence under optical control. Based on these considerations, I decided to synthesize compounds **23-25**. Treatment of **23** with sodium methoxide results in the displacement of the two fluoride ligands around the boron center with the formation of **24**.[141] Reaction of **23** with catechol, in the presence of aluminum chloride, also results in the displacement of the fluoride ligands around the boron center of the BODIPY platform to produce **25**.[139] X-Ray diffraction analysis (Table 6.1) of single crystals of the product reveals the

tetrahedral geometry of this particular atom with the coordination of a single catecholate

chelator (Figure 6.1).

Table 6.1. Crystallographic Data for **25**.

Empirical Formula	$C_{29}H_{31}N_2O_2B_1$
Formula Weight	450.37
Crystal System	Monoclinic
Lattice Parameters:	
a (Å)	11.3125(6)
b (Å)	9.5581(5)
c (Å)	12.1929(6)
α (°)	90
β (°)	111.4965(7)
γ (°)	90
V (Å^3)	1226.66(11)
Space Group	*Pc* (# 7)
Z Value	2
ρ_{calc} (g cm^{-3})	1.219
μ (Mo Kα) (mm^{-1})	0.076
T (K)	296
$2\Theta_{max}$ (°)	52.00
No. Obs. ($I > 2\sigma(I)$)	4214
No. Parameters	336
Goodness of Fit	1.062
Max. Shift in Cycle	0.004
Residuals*: R1; wR2	0.0393; 0.1052
Absorption Correction,	Multi-Scan
Max/min	0.7465 / 0.6734
Largest Peak in Final Diff. Map (e$^-$ Å^{-3})	0.142

* $R = \Sigma_{hkl}(\mid \mid F_{obs} \mid - \mid F_{calc} \mid \mid)/\Sigma_{hkl} \mid F_{obs} \mid$; $R_w = [\Sigma_{hkl}w(\mid F_{obs} \mid - \mid F_{calc} \mid)^2/\Sigma_{hkl}wF_{obs}^2]^{1/2}$,

$w = 1/\sigma^2(F_{obs})$; $GOF = [\Sigma_{hkl}w(\mid F_{obs} \mid - \mid F_{calc} \mid)^2/(n_{data} - n_{vari})]^{1/2}$.
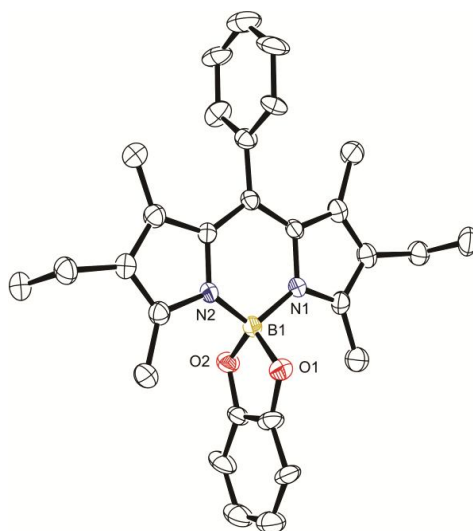
Figure 6.1. ORTEP representation of the geometry adopted by **25** in single crystals, showing 50% thermal ellipsoid probability.

Table 6.2 Absorption (λ_{Ab}) and Emission (λ_{Em}) wavelegnths as well as fluorescence quantum yields (ϕ) of **23-25** in MeCN at 25°C

	λ_{Ab} (nm)	λ_{Em} (nm)	ϕ
23	521	536	0.66
24	523	536	0.30
25	527	—	—

The corresponding absorption and emission spectra are included in Figures 6.2–6.4.
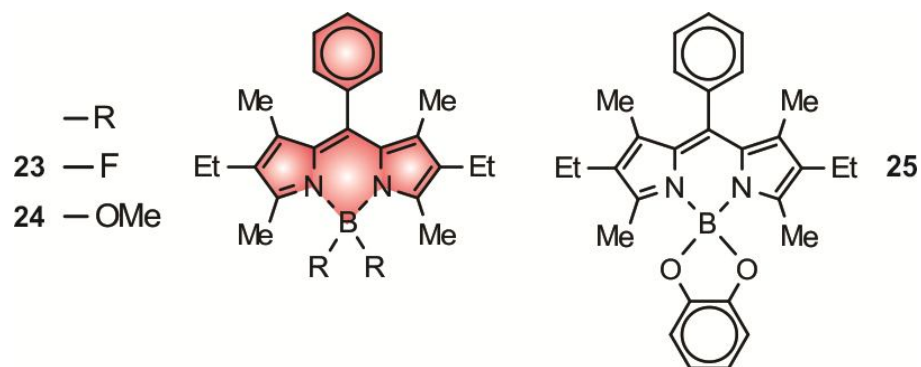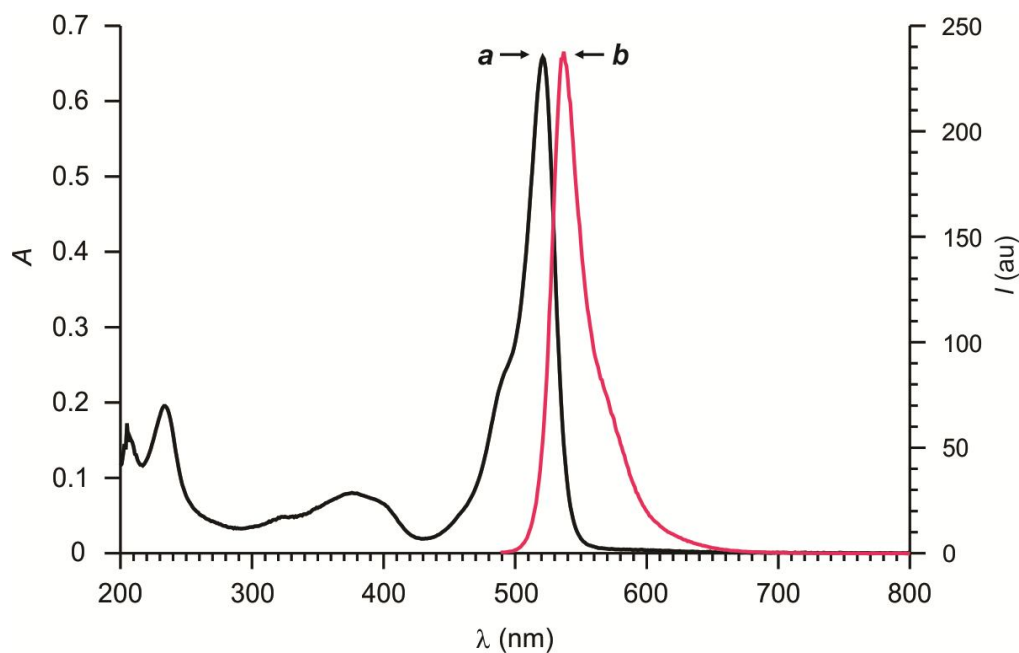
Figure 6.2. Absorption (*a*) and emission (*b*) spectra of **23** (10 μM, MeCN, 25 $^{\circ}$C, λ_{Ex} = 490 nm).
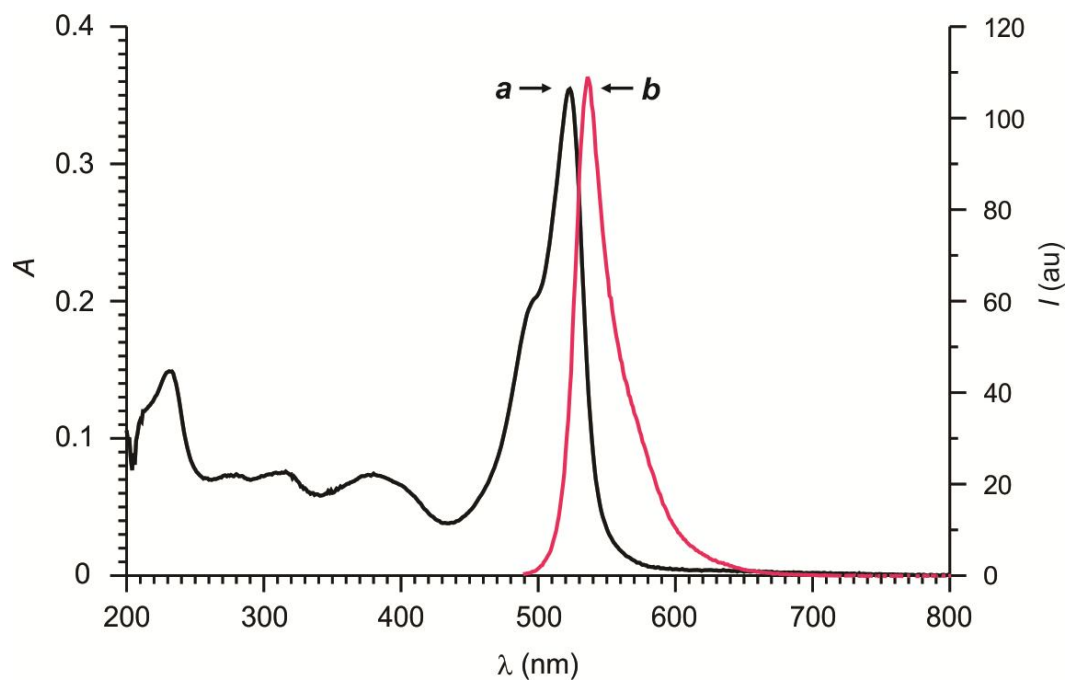
Figure 6.3. Absorption (*a*) and emission (*b*) spectra of **24** (10 μM, MeCN, 25 $^{\circ}$C, λ_{Ex} = 490 nm).

Table 6.3. Excitation energy (ΔE) and oscillator strength (*f*) of S_1 and ICT for **24** and **25** calculated ith the B3LYP and MPW1PW91 functionals.

		B3LYP		MPW1PW91	
		ΔE (eV)	*f*	ΔE (eV)	*f*
24	S_1	2.77	0.56	2.81	0.60
25	S_1	2.73	0.53	2.78	0.57
	ICT	2.36	—	2.53	—

6.2.2. Spectroscopy and Computational Studies

The absorption and emission spectra (Figure 6.2) of **23** show the characteristic bands of the BODIPY chromophore at 521 and 536 nm (λ_{Ab} and λ_{Em} in Table 6.2) respectively in acetonitrile with a fluorescence quantum yield (ϕ in Table 6.2) of 0.66 in agreement with literature data.[142] The conversion of **23** in to **24** has negligible influence on λ_{Ab} and λ_{Em} (Table 6.2 and Figure 6.3,) but lowers ϕ to 0.30. Similarly, the conversion of **23** in to **25** has negligible influence on λ_{Ab} (Table 6.2 and Figure 6.4), but suppresses completely the emission of the BODIPY chromophore. Presumably, the transfer of one electron from the catecholate chelator to the adjacent BODIPY platform, upon excitation, is responsible for fluorescence quenching. Indeed, time-dependent density-functional theory (TDDFT) supports this interpretation of the excitation dynamics of **25**. Specifically, TDDFT calculations with two different functionals (B3LYP and MPW1PW91), in combination with the 6-311+G(d,p) basis set and a solvation model for acetonitrile, assign the main absorption band of **24** and **25** in the visible region to the population of the first singlet excited state (S_1). The estimated excitation energy is *ca.* 2.7 eV (ΔE in Table 6.3) with

an oscillator strength of *ca.* 0.6 (*f* in Table 6.3).[143] The occupied and unoccupied

molecular orbitals mainly responsible for this electronic transition are both centered on

the BODIPY chromophore (Figure 6.5). In addition, these calculations indicate the

existence of an intramolecular charge-transfer (ICT) state exclusively in the case of **25**.

This state is positioned *ca.* 2.4 eV (Table 6.3) above the ground state (S_0) and its

population involves the formal transfer of one electron from an occupied molecular

orbital, localized on the catecholate ligand (Figure 6.5), to an unoccupied molecular

orbital, centered on the BODIPY platform. The ICT state of **25** is essentially forbidden,

but it can be accessed from S_1 after excitation (Figure 6.6). As a result, its presence

provides a nonradiative pathway for the deactivation of the excited state that is otherwise

responsible for the fluorescence of the BODIPY chromophore. Such pathway is not

available in **24** and, in fact, this compound reverts radiatively to S_0 after excitation to S_1

(Figure 6.6)
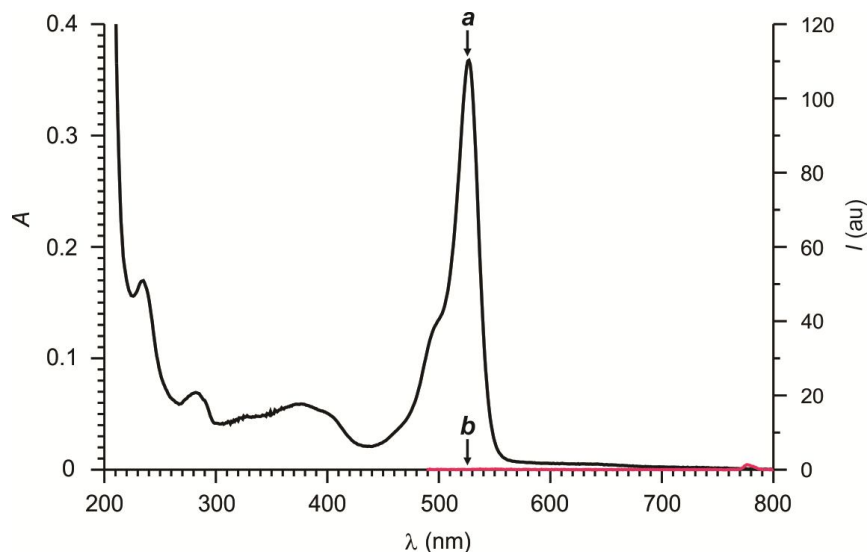
Figure 6.4. Absorption (*a*) and emission (*b*) spectra of **25** (10 μM, MeCN, 25 $^{\circ}$C, λ_{Ex} = 490 nm).

The spectroscopic behavior of **25** in methanol parallels that observed in acetonitrile. In particular, the absorption spectrum (***a*** in Figure 6.7) shows the characteristic band of the BODIPY chromophore at a λ_{Ab} of 528 nm, while the emission spectrum (***b*** in Figure 6.7) does not reveal any significant fluorescence. Upon addition of one equivalent of trifluoroacetic acid (TFA), however, an intense band appears at a λ_{Em} of 550 nm (***c*** in Figure 6.7).[144] By contrast, the very same treatment in acetonitrile does not cause any change to the emission spectrum. These observations suggest that the catecholate chelator of the nonemissive species **25** is replaced by two methoxide ligands to form the emissive BODIPY **24**, under acidic conditions in methanol.
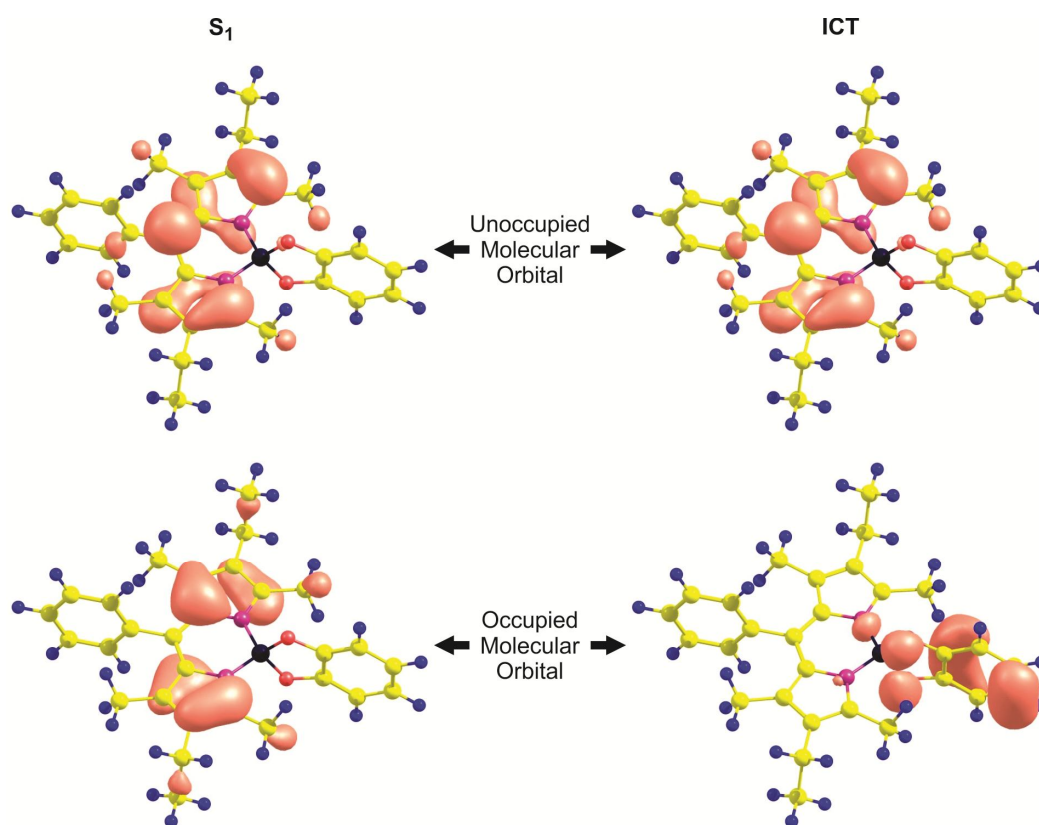
Figure 6.5. Isosurfaces of the main orbital pairs responsible for the population of S_1 and ICT computed with the B3LYP functional.
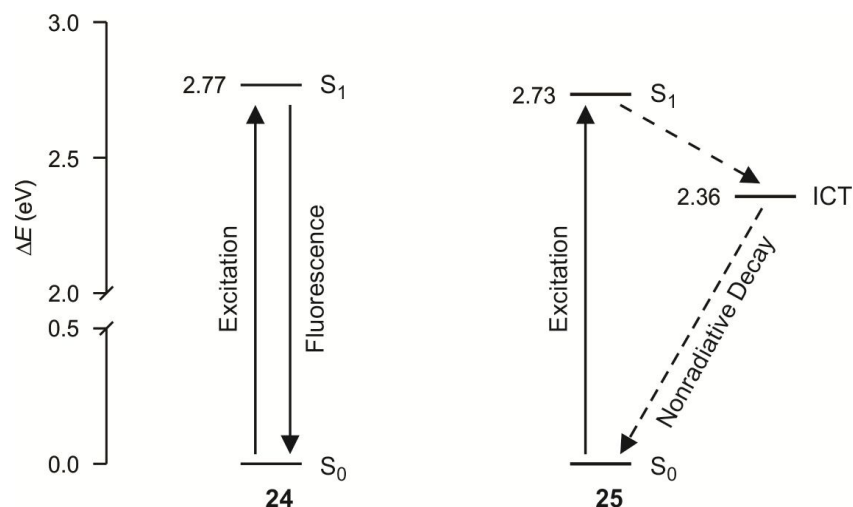
Figure 6.6. Excitation dynamics of **24** and **25** with B3LYP energies of the associated electronic states.

Indeed, the electrospray ionization mass spectra, recorded before and after this treatment, show the appearance of a peak for the molecular ion of **24**, upon acidification. Similarly, the ^{1}H nuclear magnetic resonance (NMR) spectra, recorded before and after the addition of acid in deuterated methanol, are also consistent with the transformation of **25** into **24**. In particular, the initial spectrum (*a* in Figure 6.8) shows a resonance centered at 6.75 ppm for the two pairs of homotopic protons (H^A and H^B) on the catecholate chelator of **25**. After acidification, this resonance splits into two sets of peaks centered at 6.74 and 6.66 ppm respectively (*b* in Figure 6.8). The very same peaks are also observed in the spectrum (*c* in Figure 6.8) of catechol, recorded under otherwise identical conditions. Instead, the resonances associated with the three sets of protons (H^C, H^D and H^E) on the phenyl ring, attached to the meso position of the BODIPY chromophore, remain essentially unaffected with the addition of acid (*a* and *b* in Figure 6.8).
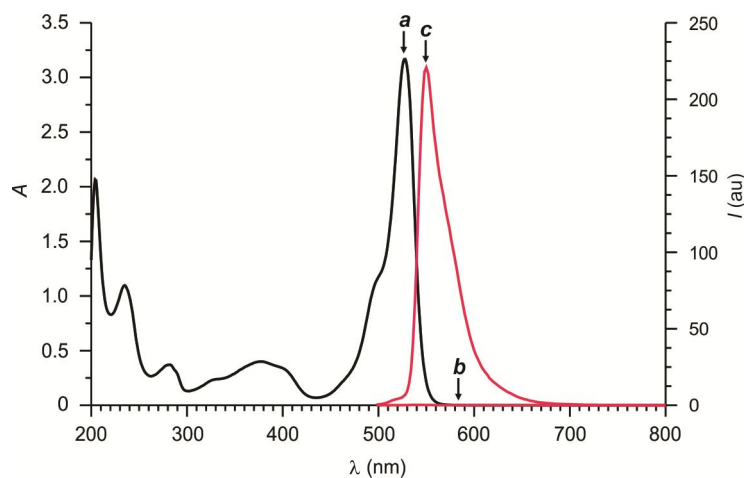
Figure 6.7. Absorption spectrum (*a*) of a MeOH solution (100 μM, 25 °C) of **25**. Emission spectra (λ_{Ex} = 490 nm) of a MeOH solution (10 μM, 25 °C) of **25**, recorded before (*b*) and (*c*) after the addition of TFA (1 equiv).

The exchange of the catecholate chelator of **25** with the two methoxide ligands of **24** can be achieved also under optical control with the aid of a photoacid generator. Specifically, the ultraviolet illumination of **8** (Figure 6.9) is known to encourage the release of hydrogen bromide with the concomitant formation of **9**.[33f] In turn, the photogenerated acid can promote the transformation of **25** into **24** in the presence of methanol. Indeed, the absorption spectra (*a* in Figure 6.9), recorded at regular intervals of time during the irradiation of an equimolar mixture of **25** and **8** in methanol, reveal the characteristic increase in absorbance at *ca.* 370 nm associated with the photoinduced formation of **9**. Instead, the absorption band in the visible region remains essentially unaffected, demonstrating that the BODIPY chromophore tolerates these irradiation conditions. In agreement with the formation of **9** and the concomitant release of acid, the corresponding emission spectra (*b* in Figure 6.9) show the growth of a band for the photogenerated fluorophore **24**. By contrast, no fluorescence can be detected under irradiation of **25** in the absence of **8**, under otherwise identical conditions, confirming that the photoacid generator is essential to activate emission.
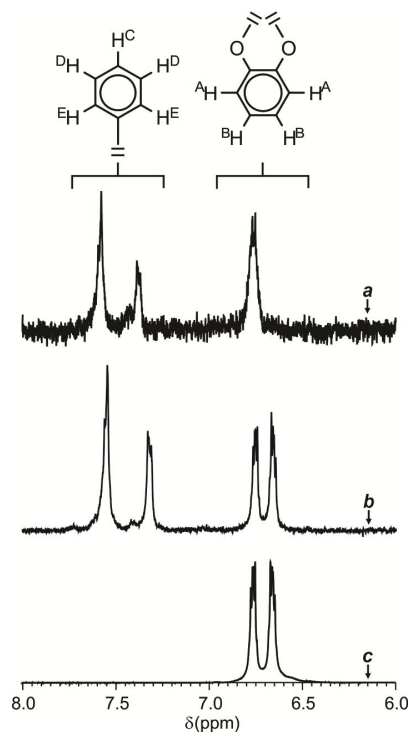
Figure 6.8. Partial ^{1}H NMR spectra (400 MHz) of CD$_3$OD solutions (10 mM, 25 °C) of **25**, recorded before (***a***) and after (***b***) the addition of TFA (1 equiv), and of catechol (***c***).
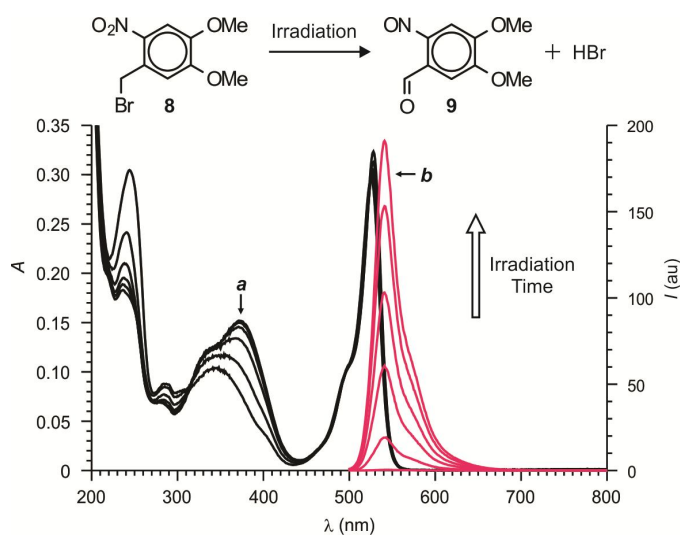
Figure 6.9. Absorption (***a***) and emission (***b***) spectra of equimolar MeOH solutions (10 μM, 25 °C, λ_{Ex} = 490 nm) of **25** and **8**, recorded before and during irradiation (350 nm, 3.33 mW cm^{-2}, 5 min) with intervals of 1 min.

6.3. Conclusions

These results demonstrate that the manipulation of the ligands around the boron center of the BODIPY platform can be exploited to activate emission under optical control. Indeed, the photoinduced generation of acid can mediate the exchange of a catecholate chelator with a pair of methoxide ligands and suppress the electron-transfer pathway that would otherwise be responsible for fluorescence quenching. Thus, these operating principles for fluorescence activation, coupled to the synthetic versatility of BODIPY chromophores and their outstanding photochemical and photophysical properties, can eventually lead to the development of valuable photoactivatable probes for a diversity of imaging applications.

CHAPTER 7

INTRACELLULAR GUEST EXCHANGE BETWEEN DYNAMIC SUPRAMOLECULAR HOSTS

7.1. Overview

Supramolecular constructs assemble spontaneously from complementary building blocks under the influence of noncovalent bonds.[145] A subtle balance of steric and electronic factors dictates the interaction mode and number of their constituent components to define ultimately the overall dimensions and shapes of the final assemblies. In addition, the moderate enthalpic contributions of noncovalent contacts, relative to their covalent counterparts, ensure reversibility and impose dynamic character on supramolecular systems. Indeed, the association and disassociation of noncovalent synthons can occur continuously on relatively short timescales, under appropriate experimental conditions, to exchange rapidly the building blocks of independent supramolecular assemblies. Thus, the reversibility of noncovalent interactions offers the attractive opportunity to engineer the controlled scrambling of simple molecular components within complex chemical ensembles that is difficult to replicate with the sole assistance of covalent bonds.[146-150]

Nanoparticles of amphiphilic polymers are a remarkable example of self-assembling supramolecular systems.[151-157] The hydrophilic and hydrophobic segments, integrated covalently within their macromolecular components, are responsible for their spontaneous assembly in aqueous environments. Specifically, noncovalent contacts bring the hydrophobic domains of distinct amphiphilic macromolecules together in order to minimize their direct exposure to water. In turn, the hydrophilic counterparts within the same macromolecular building blocks protrude into bulk solution and ensure optimal

solvation of the overall supramolecular constructs. In the process of assembling, these polymer nanoparticles can also capture multiple hydrophobic molecules and retain them in their hydrophobic interiors. In fact, the encapsulation of molecular guests within these supramolecular hosts ensures, once again, minimal exposure of the entrapped species to water. As a result, such polymer nanoparticles can be valuable vehicles to transfer molecules, which would otherwise be insoluble in water, across aqueous media. Indeed, these particular supramolecular nanocarriers can transport drugs through the blood stream as well as penetrate the membrane of living cells and deliver their cargo intracellularly.[158-167]

The ability of self-assembling nanoparticles of amphiphilic polymers to capture hydrophobic compounds can be exploited to entrap multiple chromophores within the same supramolecular container and impose photoresponsive character on the resulting construct.[168] In particular, this supramolecular strategy offers the opportunity to constrain complementary donors and acceptors in close proximity and promote the transfer of excitation energy from the former components to the latter. Such operating principles are especially valuable to engineer fluorescent materials with emissive behavior that would otherwise be impossible to achieve with their separate chromophoric components.[108,169-172] In addition, they also permit the assessment of the stability of the polymer nanocarriers under a broad range of experimental conditions.[173-184] Indeed, only if the supramolecular containers retain their integrity can the complementary donors and acceptors remain sufficiently close to each other and transfer energy efficiently upon excitation. Furthermore, the occurrence of energy transfer can also signal the exchange of molecular guests between independent nanostructured hosts.[173,176,177a,c,180] In fact, these

dynamic supramolecular assemblies can barter their macromolecular components and trade their entrapped cargo on relatively short timescales, under appropriate experimental conditions.

The unique properties of self-assembling nanoparticles of amphiphilic polymers suggest that strategies to bring complementary molecules in close proximity exclusively within the intracellular environment, and only then enforce their mutual interaction, can be implemented with the aid of such dynamic supramolecular containers. In principle, distinct hydrophobic guests can be transported sequentially across the membrane of the very same cell with independent nanoparticle hosts. Once internalized, the nanocarriers can exchange their components and, only then, permit the chemical reaction or photophysical interaction of their complementary cargos. For example, the intracellular conversion of a pro-drug into a drug, under the influence of an appropriate activator, can be envisaged on the basis of this general mechanism. This chapter demonstrates with a representative example of intracellular energy transfer that such operating principles to enforce interactions between complementary species exclusively inside living cells can, indeed, be implemented experimentally.

7.2. Results and Discussion

7.2.1. Energy Transfer between Guests Entrapped within Dynamic Supramolecular Hosts.

The pronounced hydrophobic character of **26** and **23** (Figure 7.1) translates into negligible aqueous solubility. In the presence of **10**, however, both molecules dissolve readily in neutral phosphate buffer saline (PBS). Indeed, the hydrophilic oligo(ethylene

glycol) and hydrophobic decyl chains of this particular amphiphilic polymer ensure the spontaneous assembly of nanocarriers capable of capturing either **26** or **23** in their interiors.[185] Consistently, dynamic light scattering measurements confirm the formation of particles with nanoscaled dimensions in both instances. Specifically, these analyses indicate that the hydrodynamic diameter of the nanocarriers is *ca.* 15 nm and that this value does not change significantly with the nature of the encapsulated guest and its amount relative to the polymer host (*a* and *b* in Figure 7.2).[186]
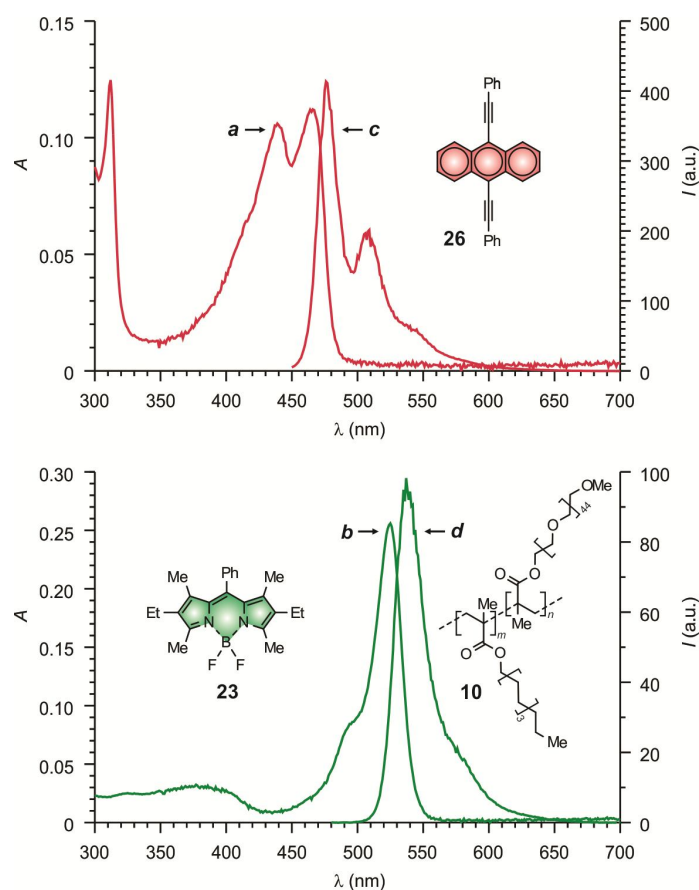
Figure 7.1. Absorption (*a* and *b*) and emission (*c* and *d*) spectra of nanoparticles of **10** (500 μg mL^{-1}), loaded with either **26** (*a* and *c*, 2 μg mL^{-1}, λ_{Ex} = 440 nm) or **23** (*b* and *d*, 2 μg mL^{-1}, λ_{Ex} = 470 nm), in PBS at 25 °C.

The absorption spectra of nanoparticles of **10** loaded with either **26** or **23** (*a* and *b* in Figure 7.1) in PBS reveal the characteristic bands of the anthracene or borondipyrromethene (BODIPY) chromophores respectively. These bands closely resemble those observed for **23** and **26** (*a–d* in Figure 7.3) in tetrahydrofuran (THF), but cannot be detected when these molecules are treated with PBS in the absence of **10**. Thus, the self-assembling nanocarriers are responsible for transferring significant amounts of **26** and **23** in the aqueous medium and, in doing so, these supramolecular containers provide an environment to the encapsulated chromophores similar to that experienced by both in THF. Furthermore, the absorption bands of the entrapped guests remain unchanged for hours, upon storage of the PBS dispersions in the dark at ambient temperature, indicating that the nanoparticles retain their integrity under these experimental conditions.
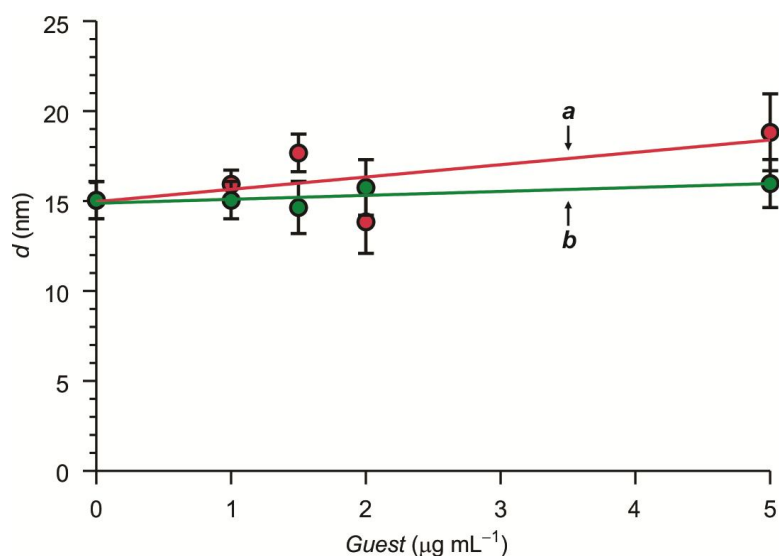
Figure 7.2. Plots of the hydrodynamic diameter of the nanocarriers, measured by dynamic light scattering, against the amount of either **26** (*a*) or **23** (*b*) relative to **10** (500 µg mL^{-1}) in PBS at 25 °C.
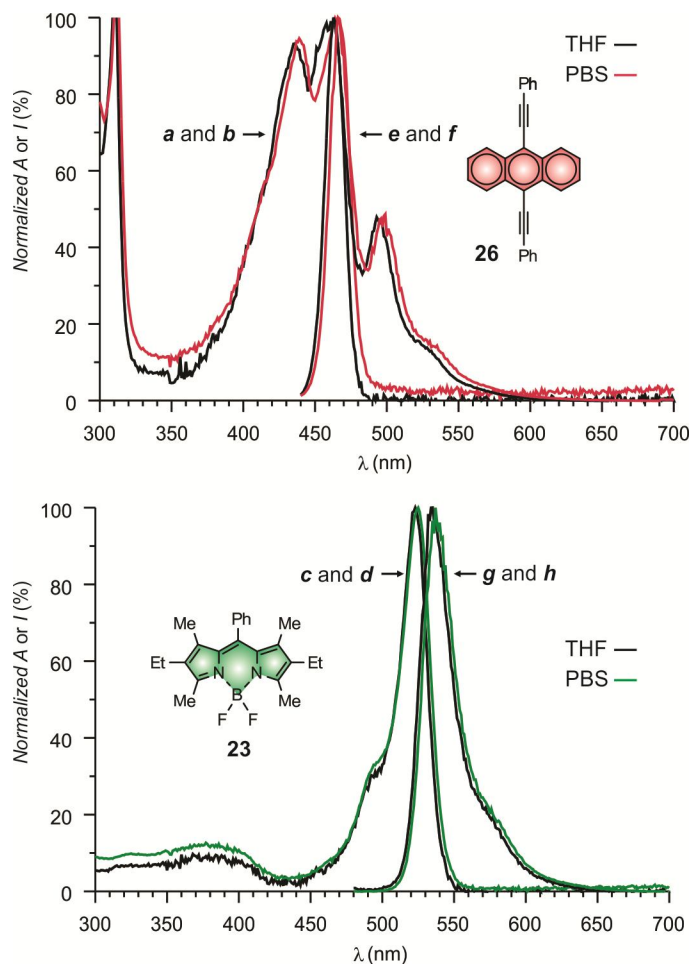
Figure 7.3. Absorption (*a–d*) and emission (*e–h*) spectra of **26** (*a* and *e*, 1 μM, λ_{Ex} = 440 nm) or **23** (*c* and *g*, 1 μM, λ_{Ex} = 470 nm) in THF and of nanoparticles of **10** (500 μg mL^{-1}), loaded with either **26** (*b* and *f*, 2 μg mL^{-1}, λ_{Ex} = 440 nm) or **23** (*d* and *h*, 2 μg mL^{-1}, λ_{Ex} = 470 nm), in PBS at 25 °C.

The corresponding emission spectra (*c* and *d* in Figure 7.1) also show the characteristic bands of the anthracene and BODIPY chromophores, enclosed within the nanocarriers, and do not change even after several hours of storage in the dark. Once again, these bands closely resemble those observed for **26** and **23** (*e–h* in Figure 7.3) in THF. The fluorescence quantum yield, however, decreases by *ca.* 30% in both instances with the encapsulation of the emissive guests in the nanostructured hosts. Specifically,

this parameter changes from 0.85 to 0.58 for **26** and from 0.72 to 0.51 for **23** with the transition from THF solution to the interior of the nanocarriers dispersed in PBS. Thus, the entrapment of these fluorophores within the nanocarriers has negligible influence on the emission wavelengths, but it has a moderate depressive effect on the efficiency of their radiative deactivation. Furthermore, the negligible solubility of **26** and **23** in aqueous media prevents the detection of their emission in the absence of **10**. Specifically, plots (*a* and *b* in Figure 7.4) of their emission intensities, measured in PBS dispersions containing increasing amounts of **10**, indicate that the polymer concentration must be greater than 10 μg mL^{-1} to encourage the transfer of significant amounts of either one of the two fluorophores in aqueous environments.[186]
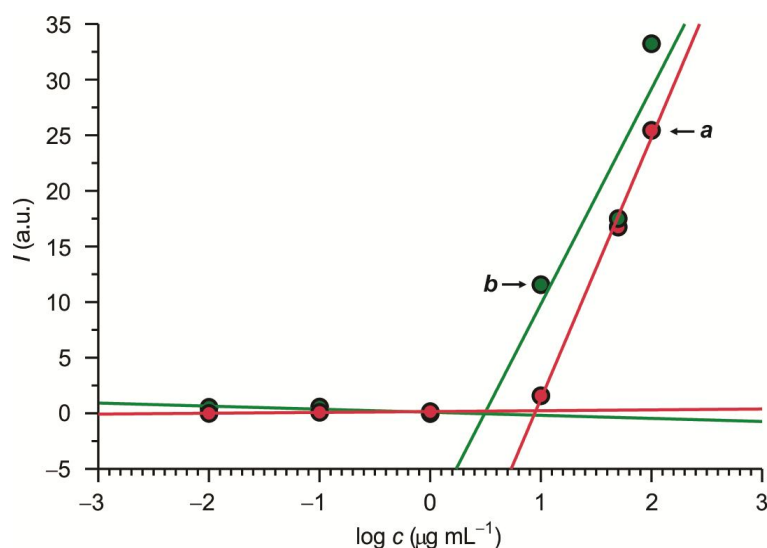
Figure 7.4. Plots of the emission intensity of either **26** (*a*, 1 μg mL^{-1}, λ_{Ex} = 440 nm, λ_{Em} = 476 nm) or **23** (*b*, 1 μg mL^{-1}, λ_{Ex} = 470 nm, λ_{Em} = 536 nm) against the concentration of **10** in PBS at 25 °C.

The emission band of **26** (*c* in Figure 7.1) is positioned within the same spectral window of the absorption band of **23** (*b* in Figure 7.1). Their overlap integral is 9.1×10^{-14} M^{-1} cm^3 and the corresponding Förster distance is 47 Å.[187] These values suggest that the co-entrapment of both chromophores within the same nanocarrier can result in the efficient transfer of energy from **26** to **23** upon excitation of the former. Indeed, a comparison of the emission spectra of nanoparticles containing exclusively either **26** or **23** (*a* and *b* in Figure 7.5) to that of nanocarriers loaded with both (*c* in Figure 7.5) clearly confirms the occurrence of energy transfer. Specifically, the emission intensity of the anthracene donors decreases significantly and that of the BODIPY acceptors increases dramatically, when both species are co-encapsulated in the same supramolecular container. The ratio between the emission intensity of the anthracene donors in the presence of the BODIPY acceptors and that in their absence indicates the efficiency of energy transfer to be 95%.
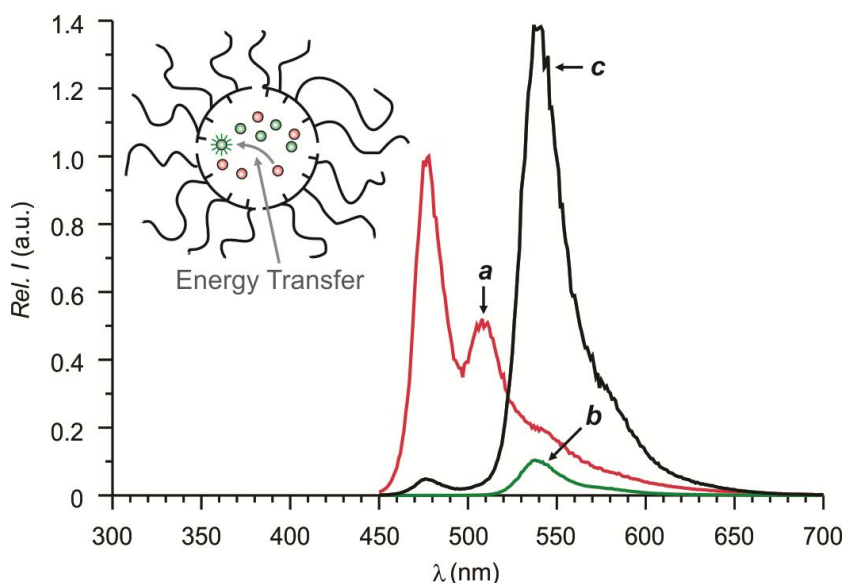
Figure 7.5. Emission spectra (λ_{Ex} = 430 nm) of nanoparticles of **10** (500 µg mL^{-1}), loaded with **26** (*a*, 5 µg mL^{-1}), **23** (*b*, 5 µg mL^{-1}) or both (*c*), in PBS at 25 °C.

The nanoparticles doped with both chromophores were prepared by co-dissolving **26**, **23** and **10** in chloroform and, after the evaporation of the organic solvent, dispersing the residue in PBS. This experimental protocol ensures the entrapment of both guests in the same supramolecular container and enables energy transfer. However, the very same result is also achieved if a PBS dispersion of nanoparticles loaded exclusively with **26** is mixed with one of nanocarriers doped independently with **23**. Upon mixing, these dynamic supramolecular assemblies exchange their components and, eventually, nanostructured containers with the two distinct chromophores in their interior are produced. Indeed, the emission spectrum (*a* in Figure 7.6), recorded immediately after mixing, closely resembles that (*c* in Figure 7.5) of nanoparticle pre-loaded with both guests. Once again, the emission of the anthracene donors is almost completely suppressed with a concomitant enhancement in the fluorescence of the BODIPY acceptors. Furthermore, the spectrum of the mixture does not change with time, indicating that the components of these supramolecular assemblies exchange with fast kinetics to establish thermodynamic equilibrium essentially upon mixing under the experimental conditions employed. In principle, two possible pathways can be envisaged for the rapid exchange of the chromophoric guests between independent nanoparticles. Specifically, a fraction of the encapsulated molecules can escape from one nanostructured container into bulk solution and then be captured by another. Alternatively, the collision of independent nanoparticles might result in the exchange of their macromolecular components together with part of their cargo. The former mechanism requires the hydrophobic guests to leak out into the aqueous environment, while the latter can occur with minimal exposure of the guests to water. The lack of any significant aqueous

solubility for both **26** and **23** (Figure 7.4) suggests that, presumably, the second pathway is mostly responsible for guest exchange.
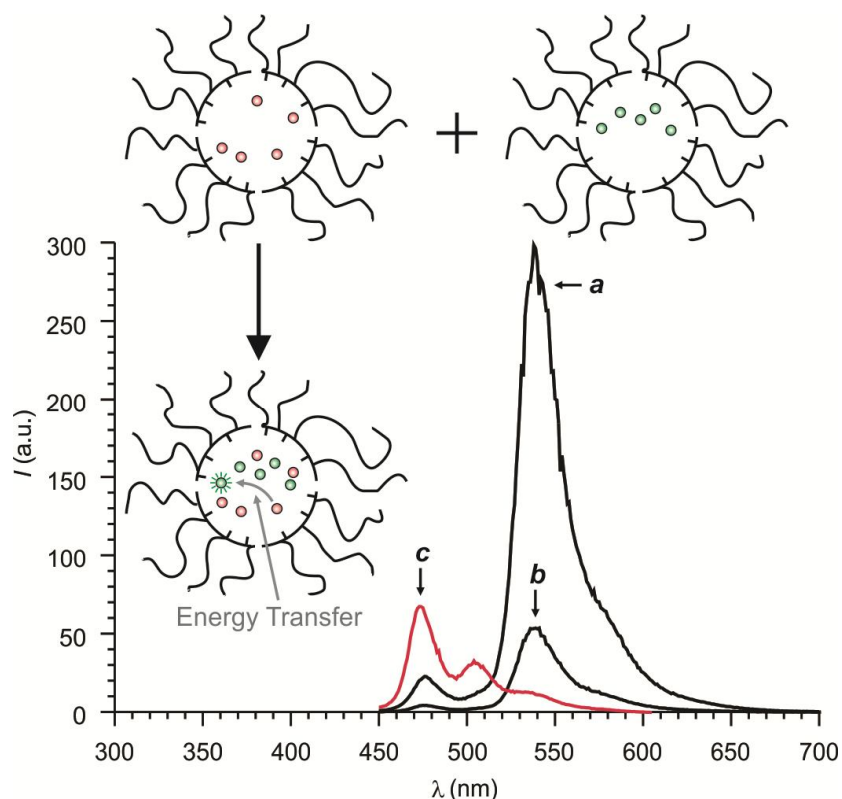
Figure 7.6. Emission spectra (λ_{Ex} = 430 nm) recorded at 25 °C after mixing identical volumes of two PBS dispersions of nanoparticles of **10** (500 µg mL^{-1}), loaded with **26** (5 µg mL^{-1}) or **23** (5 µg mL^{-1}) respectively, before (*a*) and after tenfold dilution with either PBS (*b*) or THF (*c*).

For the nanoparticles pre-loaded with both donors and acceptors as well as for those obtained after guest exchange, the energy-transfer efficiency remains unaltered even after a tenfold dilution with PBS. In fact, the resulting emission spectra (e.g., *b* in Figure 7.6) scale linearly with dilution. Instead, the transfer of energy is completely suppressed if the nanoparticles are diluted tenfold with THF. This organic solvent dismembers the supramolecular containers, separates the donors from the acceptors and prevents energy transfer. Consistently, the corresponding emission spectra (e.g., *c* in Figure 7.6) show

predominantly the donor emission. Thus, these observations demonstrate that the co-encapsulation of the complementary donors and acceptors within the same nanoparticles is essential for efficient energy transfer to occur and that independent nanocarriers exchange rapidly their cargo.

7.2.2. Intracellular Cargo Exchange between Dynamic Nanocarriers

The incubation of cervical cancer (HeLa) cells with nanoparticles of **10**, loaded with either **26** or **23**, results in the internalization of the supramolecular containers and their cargo. Fluorescence measurements (*a–d* in Figure 7.7), performed with a plate reader after washing the incubated cells, reveal the characteristic emission of the internalized fluorophores in both instances. Consistently, the acquisition of fluorescence images (*a* and *b* in Figure 7.8) of cells treated with nanocarriers containing either **26** or **23** show emission predominantly in the intracellular space. Both images were recorded by exciting the fluorophores at 458 nm, where the absorbance of **26** is significant and that of **23** is negligible (*a* and *b* in Figure 7.1), and collecting their fluorescence between 540 and 640 nm, where the emission of **26** is negligible and that of **23** is significant (*c* and *d* in Figure 7.1). As a result of this choice of wavelengths, the detected intracellular fluorescence is relatively weak in both instances. By contrast, an image (*c* and *d* in Figure 7.8) of cells, incubated with a mixture of two sets of nanoparticles loaded separately with **26** and **23**, clearly reveals intense fluorescence within the intracellular space, under otherwise identical experimental conditions.[188] The obvious increase in emission intensity indicates that energy is transferred between the internalized chromophores. Indeed, the predominant excitation of the anthracene donors at 458 nm is followed by the transfer of energy to the BODIPY acceptors with concomitant emission between 540 and 640 nm

(cf., *a* in Figure 7.6). Consistently, the emission intensities (bars in Figure 7.8), measured along lines drawn across cells in the three images, indicate five- or seven-fold fluorescence enhancements for the cells incubated with both chromophores, relative to those treated with only **26** or **23** respectively.[189] In addition, the localization of the nanocarriers within the intracellular space is further confirmed by the fluorescence evolution in the vertical direction evident in a stack of images (*a–e* in Figure 7.9) recorded by displacing stepwise the focal plane along the optic axis. Moreover, the intracellular localization of the supramolecular assemblies is in full agreement with published data on similar polymer nanoparticles.[190,191] These literature precedents suggest that the cellular uptake of the nanocarriers is mostly a consequence of clathrin- and caveolae-mediated endocytosis and, ultimately, results in their predominant localization within endosomes and lysosomes. In order to support this hypothesis, cells were incubated with nanoparticles of **10**, loaded with a mixture of **26** and **23**, and either chlorpromazine or genistein. These two compounds are known to inhibit clathrin- or caveolae-mediated endocytosis respectively.[192] Indeed, their presence reduced the intracellular fluorescence to 59 or 90% respectively (*a–c* Figure 7.10). These observations indicate that clathrin-mediated endocytosis is predominantly responsible for the cellular internalization of the nanoparticles.
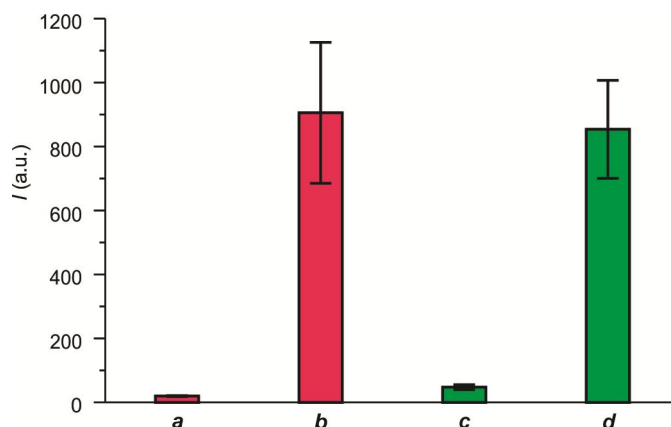
Figure 7.7. Emission intensities of HeLa cells recorded with a plate reader before (*a* and *c*) and after incubation with PBS dispersions of nanocarriers of **10** (125 µg mL^{-1}), loaded with either **26** (*b*, 1.25 µg mL^{-1}, λ_{Ex} = 430 nm, λ_{Em} = 470 nm) or **23** (*d*, 1.25 µg mL^{-1}, λ_{Ex} = 458 nm, λ_{Em} = 540 nm), for 3 hours and washing
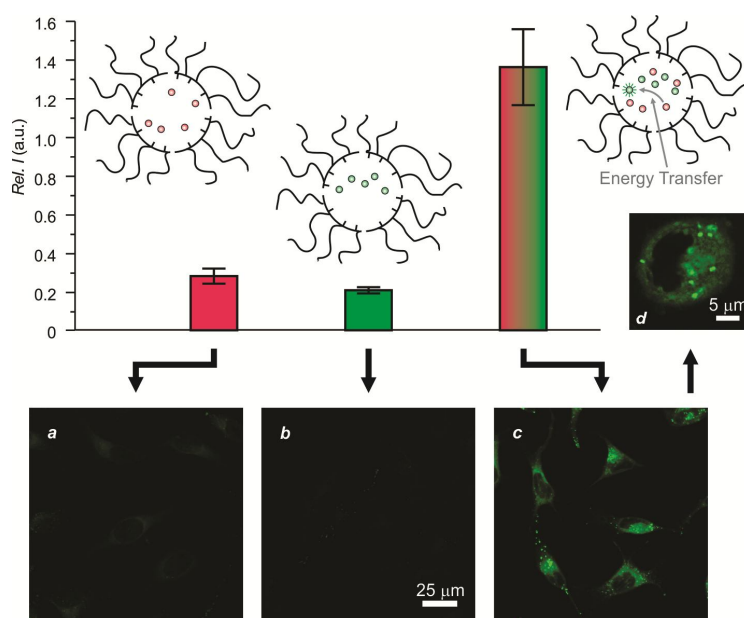
Figure 7.8. Fluorescence images (λ_{Ex} = 458 nm, λ_{Em} = 540–640 nm) of HeLa cells recorded after incubation with PBS dispersions of nanoparticles of **10** (125 µg mL^{-1}), loaded with either **26** (*a*, 1.25 µg mL^{-1}) or **23** (*b*, 1.25 µg mL^{-1}), or after incubation with a mixture (1:1, v/v) of both dispersions (*c* and *d*) for 3 hours and washing together with the corresponding emission intensities measured along lines drawn across individual cells and reported relative to that of an indocyanine green standard (50 µM, λ_{Ex} = 628 nm, λ_{Em} = 780–800 nm) added 30 min prior to termination of incubation.
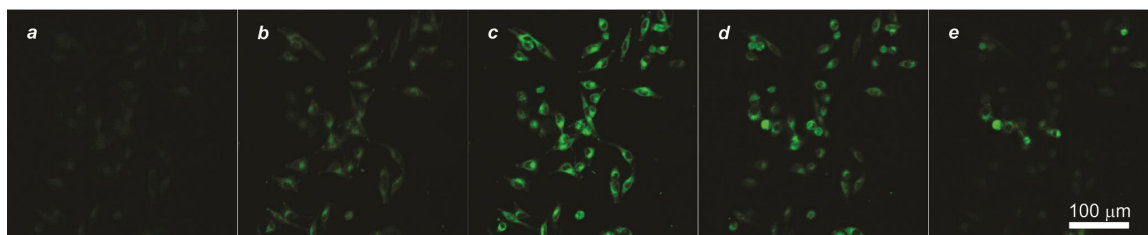
Figure 7.9. Fluorescence images (λ_{Ex} = 458 nm, λ_{Em} = 540–640 nm) of HeLa cells recorded by translating the focal plane vertically in steps of 5 μm (*a → e*) after incubation with a mixture (1:1, v/v) of two PBS dispersions of nanoparticles of **10** (125 μg mL^{-1}), loaded with **26** (1.25 μg mL^{-1}) and **23** (1.25 μg mL^{-1}) respectively, for 3 hours and washing.

The intracellular transfer of energy, evident in the corresponding fluorescence image (*c* and *d* in Figure 7.8), is achieved by allowing the nanocarriers to exchange their guests in the extracellular space and then transport mixtures of co-encapsulated donors and acceptor to the cytosol. Alternatively, the complementary chromophoric species can be delivered sequentially to the cytosol by incubating the very same cells with nanoparticles containing the acceptors first and then nanocarriers loaded with the donors or vice versa. Under these conditions, the two sets of internalized supramolecular hosts can exchange their guests and enable energy transfer. In particular, comparison of the emission intensities, recorded at 540 nm, where the fluorescence of the BODIPY chromophores is centered (*d* in Figure 7.1), for HeLa cells before (*a* in Figure 7.11) and after incubation with nanoparticles containing **23** (*b* in Figure 7.11), confirms the intracellular loading of the fluorescent species. These measurements were performed with a plate reader operating at an excitation wavelength of 430 nm, where the absorbance of the BODIPY acceptors is negligible (*b* in Figure 7.1) but that of the anthracene donors is significant (*a* in Figure 7.1). As a result, the further incubation of the very same cells with nanoparticles containing **26** translates into a dramatic fluorescence enhancement (*c* in Figure 7.11).

Thus, the sequential treatment of the cells with the two sets of nanocarriers ultimately positions donors and acceptors in close proximity within the intracellular space and permits the efficient transfer of energy between them. In agreement with this interpretation, the emission intensity (*d* in Figure 7.11) measured for cells incubated only with nanoparticles containing **26**, under otherwise identical conditions, is approximately a third of that detected after sequential incubation. Therefore, the presence of both chromophores is essential for a pronounced fluorescence increase to be observed. Furthermore, intracellular energy transfer is established also if the order of the two incubation steps is inverted. In fact, images (*a* and *b* in Figure 7.12) of cells treated with one set of nanoparticles first and then the other or *vice versa* reveal essentially the same emission intensity. In both instances, the dynamic character of the supramolecular hosts permits the co-localization of the complementary guests and enables energy transfer in the intracellular space.
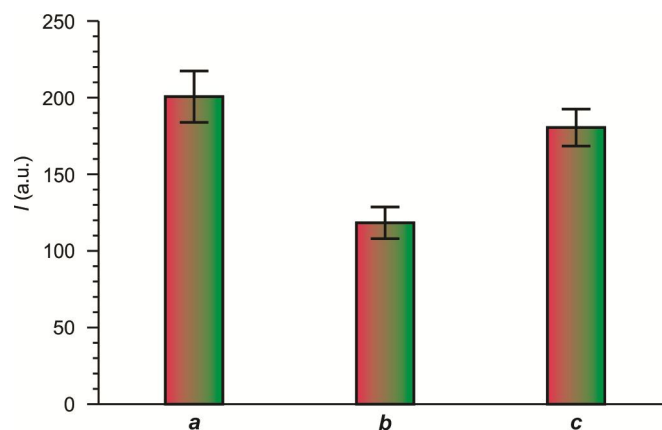
Figure 7.10. Emission intensities (λ_{Ex} = 458 nm, λ_{Em} = 540 nm) of HeLa cells recorded with a plate reader after incubation with a mixture (1:1, v/v) of two PBS dispersions of nanoparticles of **10** (125 µg mL^{-1}), loaded with **26** (1.25 µg mL^{-1}) and **23** (1.25 µg mL^{-1}) respectively, for 3 hours in the absence (*a*) and presence of either chlorpromazine (*b*, 30 µM) or genistein (*c*, 150 µM) and washing.
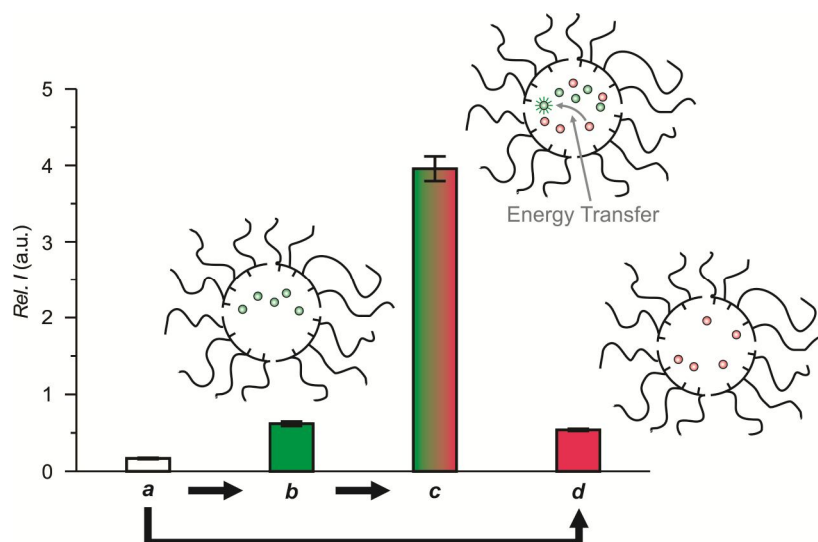
Figure 7.11. Emission intensities (λ_{Ex} = 430 nm, λ_{Em} = 540 nm), reported relative to that of an indocyanine green standard (50 µM, λ_{Ex} = 730 nm, λ_{Em} = 780 nm) added 30 min prior to termination of incubation, recorded with a plate reader before (***a***) and after incubation of HeLa cells with a PBS dispersion of nanoparticles of **10** (125 µg mL^{-1}), containing **23** (1.25 µg mL^{-1}), for 3 hours and washing (***b***) and subsequent incubation with a PBS dispersion of nanocarriers of **10** (125 µg mL^{-1}), containing **26** (1.25 µg mL^{-1}), for a further 3 hours and washing (***c***) or after incubation with the same dispersion of nanoparticles, containing **26**, for 3 hours and washing (***d***).
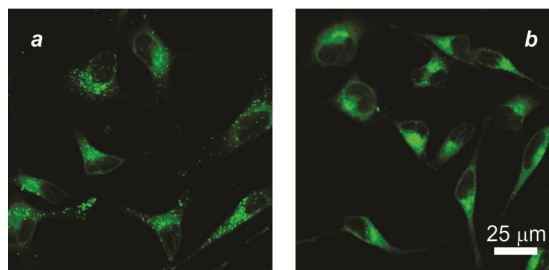
Figure 7.12. Fluorescence images (λ_{Ex} = 458 nm, λ_{Em} = 540–640 nm) of HeLa cells recorded after incubation with a PBS dispersion of nanoparticles of **10** (125 µg mL^{-1}), containing **23** (1.25 µg mL^{-1}), for 3 hours, washing and subsequent incubation with a PBS dispersion of nanocarriers of **10** (125 µg mL^{-1}), containing **26** (1.25 µg mL^{-1}), and washing (***a***) or after the same treatment but inverting the order of addition of the two components (***b***).
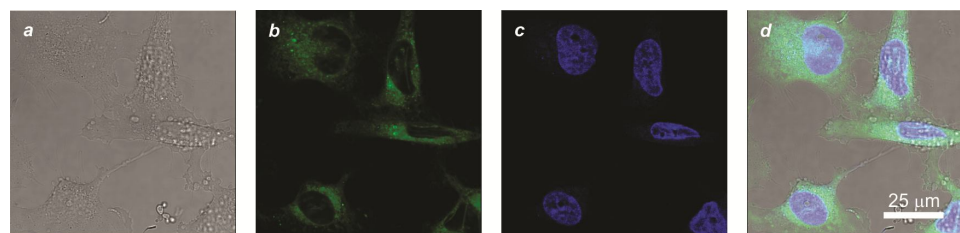
Figure 7.13. Brightfield (*a*) and fluorescence (*b*–*d*) images of HeLa cells recorded after incubation with a mixture (1:1, v/v) of two PBS dispersions of nanoparticles of **10** (125 µg mL^{-1}), loaded with **26** (1.25 µg mL^{-1}) and **23** (1.25 µg mL^{-1}) respectively, for 3 hours, addition of Hoechst 33342 (25 µM) 30 min prior to termination of incubation and washing. Image *b* was acquired with one-photon excitation at 458 nm and detection at 540–640 nm. Image *c* was recorded with two-photon excitation at 720 nm and detection at 420–450 nm. Image *d* is an overlay of images *b* and *c*.

Figure 7.14. Brightfield (*a*) and fluorescence (*b*–*d*) images of HeLa cells recorded after incubation with a PBS dispersions of nanoparticles of **10** (125 µg mL^{-1}), loaded with **26** (1.25 µg mL^{-1}), for 3 hours, addition of indocyanine green (50 µM) 30 min prior to termination of incubation and washing. Image *b* was acquired with excitation at 458 nm and detection at 540–640 nm. Image *c* was recorded with excitation at 628 nm and detection at 780–800 nm. Image *d* is an overlay of images *b* and *c*.

Figure 7.15. Brightfield (*a*) and fluorescence (*b*–*d*) images of HeLa cells recorded after incubation with a PBS dispersions of nanoparticles of **10** (125 µg mL^{-1}), loaded with **23** (1.25 µg mL^{-1}), for 3 hours, addition of indocyanine green (50 µM) 30 min prior to termination of incubation and washing. Image *b* was acquired with excitation at 458 nm and detection at 540–640 nm. Image *c* was recorded with excitation at 628 nm and detection at 780–800 nm. Image *d* is an overlay of images *b* and *c*.

Figure 7.16. Brightfield (*a*) and fluorescence (*b*–*d*) images of HeLa cells recorded after incubation with a mixture (1:1, v/v) of two PBS dispersions of nanoparticles of **10** (125 µg mL^{-1}), loaded with **26** (1.25 µg mL^{-1}) and **23** (1.25 µg mL^{-1}) respectively, for 3 hours, addition of indocyanine green (50 µM) 30 min prior to termination of incubation and washing. Image *b* was acquired with excitation at 458 nm and detection at 540–640 nm. Image *c* was recorded with excitation at 628 nm and detection at 780–800 nm. Image *d* is an overlay of images *b* and *c*.

7.3. Conclusions

Self-assembling nanoparticles of amphiphilic polymers can capture mixtures of complementary energy donors and acceptors in their hydrophobic interiors. The spectral overlap of the encapsulated chromophores and their close proximity within the supramolecular containers ensure energy transfer with essentially unitary efficiency. Furthermore, the dynamic character of these self-assembling nanocarriers translates into the rapid equilibration of their constituent components at ambient temperature in neutral buffer. As a result, pairs of nanoparticles, loaded independently with donors and acceptors respectively, can exchange their cargo upon mixing and enable energy transfer. In addition, the nanocarriers can cross the membrane of living cells and transport their fluorescent cargo to the intracellular space. In fact, intracellular energy transfer is clearly detected when the cells are incubated with two sets of self-assembling nanoparticles pre-loaded independently with acceptors and donors. Under these conditions, the dynamic supramolecular hosts exchange their guests and then shuttle co-encapsulated donors and

acceptors to the intracellular space. Alternatively, two consecutive incubation steps can be exploited to transport the complementary chromophoric components to the cytosol in sequence. After the second step, the internalized nanoparticles exchange their complementary guests in the cytosol to bring them in close proximity and allow energy transfer. Thus, the dynamic character of such self-assembling nanocarriers coupled to their ability to cross the cell membrane translates into an attractive supramolecular strategy to transport complementary species inside cells allow their mutual interactions exclusively within the intracellular space.

CHAPTER 8

EXPERIMENTAL PROCEDURES

8.1. Materials and Methods

Chemicals were purchased from commercial sources and used as received with the exception of MeCN, which was distilled over CaH_2, and THF, which was distilled over Na and Ph_2CO. Compounds **4a**, **10, 17, 19, 23-25** were prepared according to literature procedures.[33a,108,193,133c,142,141,139] All reactions were monitored by thin-layer chromatography, using aluminum sheets coated with silica (60, F_{254}). Electrospray ionization mass spectra (ESIMS) were recorded with a Bruker micrOTO-Q II spectrometer. Nuclear magnetic resonance (NMR) spectra were recorded with a Bruker Avance 400. Dynamic light scattering measurements were performed with a Malvern ZEN1600 apparatus. HPLC traces were acquired with a Varian ProStar system, equipped with a ProStar 330 photodiode array detector, using an Agilent Microsorb 100-5 BDS column (4.6 × 250 mm). Square wave voltammograms were recorded with a CH Instruments 610A electrochemical analyzer in MeCN under Ar, using a three-electrode cell. The reference was a Ag/Ag^+ electrode (1 mM $AgNO_3$ in MeCN). The counter and working were a platinum wire and a glassy-carbon electrode respectively. The supporting electrolyte was tetrabutylammonium hexafluorophosphate (0.1 M). The scan rate and pulse amplitude were 50 mV·s^{-1} and 50 mV respectively.

8.2. Absorption and Emission Spectroscopies

Absorption spectra were recorded with a Varian Cary 100 Bio spectrometer, using quartz cells with a path length of 0.5 or 1.0 cm. Emission spectra were recorded with a Varian

Cary Eclipse spectrometer in aerated solutions. Custom-built sample holders were used to record the absorption and emissions spectra of the polymer films. Irradiations at 365 nm (0.4 mW cm^{-2}) were carried out with a Mineralight UVGL–25 lamp. Irradiations at 350 nm (3.33 or 4.88 mW cm^{-2}) were carried out within the chamber of a Luzchem Research LZC–4V photoreactor. The fluorescence quantum yields were measured with a fluorescein standard, following a literature protocol.[28] The quantum yields for the photochemical conversions were determined with a potassium ferrioxalate actinometer, according to an established procedure.[137] Doped polymer films were prepared by spin coating CH$_2$Cl$_2$ solutions of PBMA (M_W = 337 × 10^3, 156 mg mL^{-1}) and **4a** (3.0 mg mL^{-1}) with and without **8** (1.5 mg mL^{-1}) with a Chemat Technologies KW-4A spin coater at 390 rpm for 18 s and then at 790 rpm for 60 s on quartz disks for the spectroscopic measurements and on glass coverslips for the imaging experiments. The thickness of the polymer films (<10 μm) was measured with a Mitutoyo digital micrometer.

8.3. Ensemble and Single Molecule Imaging

Ensemble fluorescence images were recorded with a Leica SP5 confocal laser-scanning microscope. The fluorescence image of **20** was obtained by placing the imaged solution between two glass slides separated by a Teflon ring with a thickness of 0.44 mm. Single-molecule fluorescence images were recorded with a custom-built wide-field epi-fluorescence microscope. Excitation was performed with a continuous-wave (CW) diode-pumped solid-state Shanghai Dream Lasers Technology Co. SDL-532-LM-200-T laser operating at a 532 nm with an intensity of 7 kW cm^{-2} calculated at the focal plane. Activation was performed with a CW diode Shanghai Dream Lasers Technology Co.

SDL-405-LM-20-T laser operating at 405 nm with an intensity lower than 100 W cm^{-2}. While the excitation laser was continuously running, the activation laser was switched on for short periods during camera read-out. The duration of the activation pulse was changed from 50 to 500 μs and, therefore, the longest pulses had some overlap with the frame recording. Nevertheless, no increase in background signal was observed because of the low activation intensity. The lasers were combined in one beam with a Chroma Technology Corp. ZT405rdc dichroic mirror and illumination was performed in wide-field mode by focusing both lasers in the back focal plane of a 63× oil-immersion Olympus objective lens with a numerical aperture of 1.25. The fluorescence signal was collected by the same objective, separated from activation and excitation light by a Chroma Technology Corp. ZT532rdc dichroic mirror, further cleaned with a Semrock Inc. NF01-532U-25 notch filter and a Semrock Inc. FF01-640/40 bandpass filter and then detected by an Andor Technology IXON-DU-897 EMCCD camera. Localization of single-molecule events and image reconstruction were performed as previously described.[202]

8.4. Intracellular Fluorescence Imaging

Plate readings were performed with a Flex station at 540 nm, using an excitation wavelength of either 430 or 458 nm. The emission intensities of the bars in Figures 7.7 and 7.10 are absolute values. Those in Figure 7.11 are reported relative to that of an indocyanine green standard. The fluorescence of the standard was recorded at 780 nm with an excitation at 730 nm. Fluorescence images were recorded with a Leica SP5 confocal laser-scanning multiphoton microscope, equipped with an incubator maintained

at 37 °C in O_2/CO_2/air (20:5:75, v/v/v). The emission intensity was recorded between 540 and 640 nm, using an excitation wavelength of 458 nm, and it is reported relative to that of an indocyanine green standard in the corresponding bar charts. Specifically, the emission intensities of fluorescent guests and standard were measured along four lines drawn across cells and the ratio between the two is quoted. The fluorescence of the standard was recorded between 780 and 800 nm with an excitation wavelength of 628 nm. The fluorescence of Hoechst 33342 was recorded between 420 and 450 nm with two-photon excitation at 720 nm.

8.5. Polymer Nanoparticles

Polymer micelles were prepared by combining $CHCl_3$ solutions of **4a** (0.1 mg mL^{-1}, 50 μL), **8** (0.1 mg mL^{-1}, 50 μL) and **10** (2.5 mg mL^{-1}, 200 μL) and by combining $CHCl_3$ solutions of **23** (0.1 mg mL^{-1}, 0-50 μL), **26** (0.1 mg mL^{-1}, 0-50 μL) and **10** (2.5 mg mL^{-1}, 200 μL) and heating the resulting mixture at 40 °C in an open vial. After the evaporation of the solvent, the residue was purged with air and dispersed in phosphate buffer saline (PBS, 1 mL, pH = 7.0). After vigorous shaking, the dispersion was filtered and the filtrate was either spin coated at 1,000 rpm for 20 s with a Laurell Tech. Corp. WS-400B-6NPP/lite spin coater on glass coverslips that were previously cleaned with O_3 for 20 min using a Jelight Company Inc. UVO Cleaner 42 for single molecule fluorescence imaging or used without further purification for spectroscopic and imaging experiments inside HeLa cells.

8.6. Cells

HeLa cells were cultured in Dulbecco's modified Eagle's media, supplemented with foetal bovine serum (10%, v/v), penicillin (200 U mL^{-1}), streptomycin (200 μg mL^{-1}), non-essential amino acids (0.1 mM) and incubated at 37 °C in O_2/CO_2/air (20:5:75, v/v/v). The cells were seeded in 384-well glass-bottom plates at a density of 5×10^4 cells mL^{-1} and incubated overnight at 37 °C in O_2/CO_2/air (20:5:75, v/v/v). The cultured cells were incubated further with PBS dispersions (25%, v/v) of nanoparticles of **10** (125 μg mL^{-1}) loaded with either **26** (1.25 μg mL^{-1}) or **23** (1.25 μg mL^{-1}) or with a mixture (1:1, v/v) of both dispersions for 3 hours and then washed three times with PBS (80 μL). Alternatively, they were incubated with nanoparticles containing either one of the two guests for 3 hours, washed three times, incubated with nanoparticles loaded with the other for a further 3 hours and washed three more times. Internal standard indocyanine green (50 μM) was added to all wells 30 min prior to termination of incubation with nanoparticles. Inhibition experiments were performed by adding either chlorpromazine (30 μM) or genistein (150 μM) to the cells 30 min prior to incubation with nanoparticles pre-loaded with a mixture of **26** and **23**. Nuclear staining experiments were performed by adding Hoechst 33342 (25 μM) to the cells 30 min prior to termination of incubation with nanoparticles.

BHK (Baby Hamster Kidney) cells were cultured in 10 cm plastic dishes in complete medium: DMEM (Dulbecco's Modified Eagle Medium) supplemented with 10% v/v fetal bovine serum and penicillin/streptomycin (200 U mL^{-1} and 200 μg mL^{-1} respectively), at 37 °C and 5% CO_2. For the micelles incorporation experiments, the cells were splitted

and plated onto glass coverslips. After removing the culture medium, they were briefly starved with PBS (Phosphate Buffered Saline) for 1 h, and then incubated overnight in complete medium containing a 10% v/v of the micelle dispersion prepared as described elsewhere.[108] The samples were finally washed with PBS to remove unincorporated micelles, fixed with MeOH (10 min at -20 °C), and mounted in Mowiol® for subsequent imaging.

8.7. Crystallographic Analysis

The data crystal of **25** and **11** were glued onto the end of a thin glass fiber. X-ray intensity data were measured with a Bruker SMART APEX2 CCD-based diffractometer, using Mo Kα radiation (λ = 0.71073 Å).[194] The raw data frames were integrated with the SAINT+ program by using a narrow-frame integration algorithm. Corrections for Lorentz and polarization effects were also applied with SAINT+. An empirical absorption correction based on the multiple measurement of equivalent reflections was applied using the program SADABS. The structure was solved by a combination of direct methods and difference Fourier syntheses and refined by full-matrix least-squares on F^2 with the SHELXTL software package.[195] Hydrogen atoms were placed in geometrically-idealized positions and included, as standard riding atoms, during the least-squares refinements. Crystal data, data collection parameters and results of the analyses for **11** and **25** are listed in Tables 4.1 and 6.1 respectively.

Single crystals of **11** were obtained after maintaining an acetonitrile solution of the compound at ambient temperature in a sealed tube. Compound **11** crystallized in the monoclinic crystal system. The systematic absences in the intensity data identified the

unique space group $P2_1/n$. Red single crystals (monoclinic) of **25** suitable for X-ray diffraction analysis were obtained from a CHCl$_3$/hexane solution, after the evaporation of the solvent at ambient pressure and temperature. Based on the systematic absences in the intensity data, the space group Pc was chosen and confirmed by the successful refinement of the structure. The entire molecule is disordered over two orientations and the refinement was constrained to sum to unity. Both disorder components were located from the difference map and were modeled using SHELX: AFIX and EADP instructions. The final refined occupancies ratio are 0.723(3) / 0.277(3). Several attempts were made to crystallize this compound from different solvent mixtures, under various crystallization conditions. However, red single crystals were always obtained with the same unit cell dimensions. Furthermore, disorder could not be avoided even by collecting data at 100 K.

8.8. Computational Protocol

The geometries of **24** and **25** were optimized with the restricted B3LYP[196,197] and MPW1PW91[198,199] functionals implemented in Gaussian 09,[200] using the 6-311+G(d,p) basis set and the polarizable continuum model for acetonitrile with the integral equation formalism variant.[201] The frequencies, molecular orbitals and the energies of the first ten singlet excited states associated with the optimized geometries were computed at the same level of theory. No imaginary frequencies were found in both instances.

8.9. Experimental Procedures

Synthesis of 11

A solution of **12** (549 mg, 3.4 mmol) and **15** (800 mg, 3.4 mmol) in MeCN (10 mL) was heated for 12 hours under reflux and Ar. After cooling down to ambient temperature, the solvent was distilled off under reduced pressure. The residue was dissolved in CH_2Cl_2 (50 mL) and washed with H_2O (20 mL). The organic layer was dried over Na_2SO_4 and the solvent was distilled off under reduced pressure. The residue was purified by column chromatography [SiO_2, hexanes/AcOEt (95:5, v/v)] to give **11** (150 mg**,** 14%) as a yellow solid.   ESIMS: m/z = 311.1401 $[M + H]^+$ (m/z calcd. for $C_{18}H_{19}N_2O_3$ = 311.1390); ^1H NMR (CD_3CN): δ = 1.17 (3H, s), 1.53 (3H, s), 1.60 (3H, s), 4.86 (1H, d, 16 Hz), 5.04 (1H, d, 16 Hz), 6.66 (1H, d, 8 Hz), 6.79–6.83 (1H, m), 6.98–7.05 (2H, m), 7.17 (1H, d, 8 Hz), 7.28 (1H, t, 8 Hz), 7.67 (1H, d, 8 Hz); ^{13}C NMR ($CDCl_3$): δ = 16.1, 18.8, 25.8, 38.9, 47.8, 100.6, 108.3, 116.0, 117.1, 120.3, 122.4, 123.9, 127.6, 137.9, 146.8, 147.7, 154.7.

Synthesis of 14

A solution of 2-methyl-3-methoxynitrobenzene (1.0 g, 6.0 mmol), azobisisobutyronitrile (98 mg, 0.1 mmol) and *N*-bromosuccinimide (1.3 g, 1.2 mmol) in CCl_4 (15 mL) was heated for 14 hours under reflux and Ar. After cooling down to ambient temperature, the reaction mixture was diluted with CH_2Cl_2 (30 mL) and was washed with H_2O (20 mL). The organic layer was dried over Na_2SO_4 and the solvent was distilled off under reduced pressure to give **14** (1.2 g, 82%) as a white solid. ESIMS: m/z = 245.9760 $[M + H]^+$ (m/z calcd. for $C_8H_9BrNO_3$ = 245.9760); ^1H NMR ($CDCl_3$): δ = 4.00 (3H, s), 4.84 (2H, s),

7.18 (1H, bs), 7.45 (1H, d, 8Hz), 7.55 (1H, d, 8 Hz); ^{13}C NMR (CDCl$_3$): δ = 22.0, 57.4, 115.6, 117.1, 121.6, 130.0, 149.8, 158.5.

Synthesis of 15

A solution of BBr$_3$ in CH$_2$Cl$_2$ (1 M, 12.7 mL) was added dropwise to a solution of **14** (1.2 g, 4.9 mmol) in CH$_2$Cl$_2$ (10 mL) maintained at −78 °C under inert atmosphere. The reaction mixture was allowed to warm up to ambient temperature and stirred for a further 12 hours, poured into H$_2$O (10 mL) and extracted with CH$_2$Cl$_2$ (30 mL). The organic layer was dried over Na$_2$SO$_4$ and the solvent was distilled off under reduced pressure. The residue was dissolved in AcOEt (10 mL) and filtered through a silica plug, which was washed thoroughly with AcOEt. The solvent was distilled off under reduced pressure to give **15** (800 mg, 71%) as a brown solid. ESIMS: m/z = 231.9604 [M + H]$^+$ (m/z calcd. for C$_7$H$_7$BrNO$_3$ = 231.9604); ^{1}H NMR (CD$_3$CN): δ = 4.78 (2H, s), 7.23 (1H, d, 8 Hz), 7.39 (1H, t, 8 Hz), 7.49 (1H, d, 8 Hz); ^{13}C NMR (CD$_3$OD): δ 21.7, 115.6, 119.3, 120.0, 129.7, 150.1, 157.2.

Synthesis of 16

A solution of **11** (100 mg, 0.32 mmol), **17** (79 mg, 0.32 mmol) and TFA (0.16 mL, 6.5 mmol) in MeCN (10 mL) was heated under reflux for 24 hours. After cooling down to ambient temperature, the solvent was distilled off under reduced pressure and the residue was dissolved in CH$_2$Cl$_2$ (5 mL). The addition of hexane (50 mL) caused the precipitation of a solid, which was filtered off, dissolved in CH$_2$Cl$_2$ (20 mL) and washed with H$_2$O (20 mL). The organic phase was dried over Na$_2$SO$_4$ and the solvent was distilled off under reduced pressure. The residue was purified by preparative thin-layer chromatography

[SiO$_2$: (CH$_2$Cl$_2$)] to give **16** (30 mg, 17.4%). ESIMS: *m/z* = 538.2338 [M + H]$^+$ (*m/z* calcd. for C$_{32}$H$_{32}$N$_3$O$_5$ = 538.2336); ^{1}H NMR [(CD$_3$)$_2$CO]: δ = 1.21 (9H, bs), 1.54 (3H, s), 3.51-3.53 (4H, q, 8 Hz), 4.81-5.14 (2H, s), 6.51 (1H, s,) 6.72-6.75 (1H, d, 12 Hz), 6.82–6.85 (3H, m, 12 Hz), 6.94–6.98 (1H, d, 16 Hz), 7.03-7.07 (1H, t, 16 Hz), 7.18–7.21 (2H, t, 12 Hz), 7.36-7.41 (2H, m, 20 Hz), 7.64–7.66 (1H, d, 8 Hz), 7.93 (1H,s). ^{13}CNMR [(CD$_3$)$_2$CO]: δ = 12.3, 17.7, 25.9, 39.0, 44.6, 49.4, 96.3, 102.3, 108.7, 115.0, 116.5, 120.0, 122.9 125.0, 127.3, 129.4, 130.8, 138.3, 141.0, 146.8, 148.1, 150.8, 154.8, 155.8, 159.8.

Synthesis of 20

A mixture of **19** (56 mg, 0.2 mmol) and (1-bromomethyl)-4,5-dimethoxy-2-nitrobenzene (59 mg, 0.3 mmol) in MeCN (10 mL) was heated under reflux for 12 hours. After cooling down to ambient temperature, the solvent was removed under reduced pressure. The residue was suspended in EtOAc (50 mL), washed with H$_2$O (2 × 20 mL) and brine (20 mL) and dried over Na$_2$SO$_4$. The solvent was distilled off under reduced pressure and the residue was purified by column chromatography [Al$_2$O$_3$ (activated, neutral), CH$_2$Cl$_2$/MeOH (100:0 → 95:5, v/v)]. The resulting solid was dissolved in CH$_2$Cl$_2$ (2 mL). The addition of hexane (10 mL) caused the formation of a precipitate, which was filtered off and dissolved in Me$_2$CO (5 mL). After the addition of a saturated aqueous solution of NH$_4$PF$_6$ (5 mL), the mixture was concentrated under reduced pressure to half of its original volume and the resulting precipitate was filtered off to give the hexafluorophosphate salt of **20** (20 mg, 17%) as a red powder. ESIMS: *m/z* = 577.2830 [M]$^+$ (*m/z* calcd. for C$_{31}$H$_{36}$BF$_2$N$_4$O$_4$ = 577.2798); ^{1}H NMR (CDCl$_3$): δ = 0.96 (6H, t, 8

Hz), 1.33 (6H, s), 2.30 (4H, q, 8 Hz), 2.55 (6H, s), 4.04 (3H, s), 4.18 (3H, s), 6.15 (2 H, s), 7.72 (1 H, s), 7.84 (1H, s), 7.97 (2H, d, 8 Hz), 8.73 (2H, d, 8 Hz); ^{13}C NMR (CDCl$_3$);

δ = 11.8, 12.0, 13.4, 13.8, 16.5, 22.4, 29.0, 31.2, 56.3, 56.4, 62.5, 109.3, 116.5, 119.7, 128.8, 132.5, 134.3, 138.2, 141.1, 145.4, 150.7, 153.8, 154.1, 156.0.

Synthesis of 21

K$_2$CO$_3$ (52 mg, 0.3 mmol) was added to a solution of **22** (70 mg, 0.2 mmol) and (1-bromomethyl)-4,5-dimethoxy-2-nitrobenzene (59 mg, 0.3 mmol) in Me$_2$CO (10 mL) and the mixture was heated under reflux for 12 hours. After cooling down to ambient temperature, the solvent was removed under reduced pressure. The residue was suspended in EtOAc (50 mL), washed with aqueous citric acid (10% v/v, 2 × 20 mL), saturated aqueous NaHCO$_3$ (2 × 20 mL) and brine (20 mL) and dried over Na$_2$SO$_4$. The solvent was distilled off under reduced pressure and the residue was purified by column chromatography [SiO$_2$, CH$_2$Cl$_2$/hexane (2:1, v/v)] to afford **3** (60 mg, 60%) as a pink solid. ESIMS: m/z = 591.2732 [M]$^+$ (m/z calcd. for C$_{32}$H$_{36}$BF$_2$N$_3$O$_5$ = 591.2716); ^{1}H NMR (CDCl$_3$): δ = 1.00 (6H, t, 8 Hz), 1.34 (6H, s), 2.30 (4H, q, 8 Hz), 2.47 (6H, s), 3.98 (3H, s), 4.02 (3H, s), 5.6 (2 H, s), 7.13 (1 H, d, 9 Hz), 7.24 (1 H, d, 9 Hz), 7.37 (1 H, s), 7.82 (1 H, s); ^{13}C NMR (CDCl$_3$): δ = 12.2, 12.8, 15.0, 17.4, 49.9, 50.1, 50.3, 56.8, 57.4, 67.5, 107.4, 108.5, 109.7, 115.9, 129.2, 129.3, 130.1, 131.5, 138.7, 139.5, 140.2, 148.3, 154.1, 154.4, 158.8.

References and Notes

1. Krafft, G. A.; Cummings, R. T.; Dizio, J. P.; Furukawa, R. H.; Brvenik, L. J.; Sutton, W. R.; War, B. R. in *Nucleocytoplasmic Transport*; Peters, R.; Trendelenburg, M., (Eds.); Springer-Verlag: Berlin, Germany, 1986, 35–52.

2. Adams, S. R.; Tsien, R. Y. *Ann. Rev. Phys.* **1993**, *55*, 755–784.

3. Mitchison, T. J.; Sawin, K. E.; Theriot, J. A.; Gee, K.; Mallavarapu, A. *Methods Enzymol.* **1998**, *291*, 63–78.

4. Politz, J. C. *Trends Cell Biol.* **1999**, *9*, 284–287.

5. Wysocki, L. M.; Davis, L. D. *Curr. Opin. Chem. Biol.* **2011**, *15*, 752–759.

6. Puliti, D.; Warther, D.; Orange, C.; Specht, A.; Goeldner, M. *Bioorg. Med. Chem.* **2011**, *19*, 1023–1029.

7. Li, W.-H.; Zheng, G. *Photochem. Photobiol. Sci.* **2012**, *11*, 460–471.

8. Ware, B. R.; Brvenik, L. J.; Cummings, R. T.; Furukawa, R. H.; Krafft, G. A. in *Applications of Fluorescence in the Biomedical Sciences.* Taylor, D. L.; Waggoner, A. S.; Murphy, R. F.; Lanni, F.; Birge, R. B., (Eds.), Liss: New York, 1986, 141–157.

9. Kao, J. P. Y.; Adams, S. R. in Optical Microscopy: *Emerging Methods and Applications*, Herman, B.; Lemasters, J. J., (Eds.); Academic Press: San Diego, 1993, 27–85.

10. Dirks, R. W.; Molenaar, C.; Tanke, H. J. *Histochem. Cell Biol.* **2001**, *115*, 3–11.

11. Goeldner, M.; Givens, R. (Eds.) *Dynamic Studies in Biology: Phototriggers, Photoswitches and Caged Biomolecules*; Wiley–VCH: Weinheim, Germany, 2005.

12. Ellis-Davies, G. C. *Nat. Methods* **2007**, *4*, 619–628.

13. Xu, Y.; Melia, T. J.; Toomre, D. T. *Curr. Opin. Chem. Biol.* **2011**, *15*, 822–830.

14. Fernández-Suárez, M.; Ting, A. Y. *Nat. Rev. Mol. Cell. Biol.* **2008**, *9*, 929–943.

15. Huang, B.; Bates, M.; Zhuang, X. *Annu. Rev. Biochem.* **2009**, *78*, 993–1016

16. Hell, S. W. *Nat. Methods* **2009**, *6*, 24–32.

17. Toomre, D.; Bewersdorf, J. *Ann. Rev. Cell Develop. Biol.* **2010**, *26*, 285–314.

18. van de Linde, S.; Heilemann, M.; Sauer, M. *Annu. Rev. Phys. Chem.* **2012**, *63*, 519–540.

19. Ha, T.; Tinnefeld, P. *Annu. Rev. Phys. Chem.* **2012**, *63*, 595–617.

20. Moerner, W. E. *J. Microsc.* **2012**, *246*, 213–220.

21. Raymo, F. M. *J. Phys. Chem. Lett.* **2012**, 3, 2379–2385.

22. (a) Lippincott-Schwartz, J.; Altan-Bonnet, N.; Patterson, G. H. *Nat. Cell. Biol.* **2003**, *5*, S7–S14. (b) Lippincott-Schwartz, J.; Patterson, G. H. *Science* **2003**, 300, 87–91. (c) Shaner, N. C.; Patterson, G. H.; Davidson, M. W. *J. Cell Sci.* **2007**, *120*, 4247–4260. (d) Manley, S.; Gillette, J. M.; Lippincott-Schwartz, J. *Methods Enzymol.* **2010**, *475*, 109–120. (e) Lippincott-Schwartz, J. *Dev. Cell.* **2011**, *21*, 5–10. (f) Patterson, G. H. *J. Microscopy* **2011**, *243*, 1–7.

23. (a) Verkhusha, V. V.; Lukyanov, K. A. *Nat. Biotechnol.* **2004**, *22*, 289–296. (b) Stepanenko, O. V.; Stepanenko, O. V.; Shcherbakova, D. M.; Kutznetsova, I. M.; Turoverov, K. K.; Verkhusha, V. V. *Biotechniques* **2011**, *51*, 313–327. (c) Shcherbakova, D. M.; Subach, O. M.; Verkhusha, V. V. *Angew. Chem. Int. Ed.* **2012**, *51*, 10724–10738. (d) Subach, F. V.; Verkhusha, V. V. *Chem. Rev.* **2012**, *112*, 4308–4327.

24. Wiedenmann, J.; Gayda, S.; Adam, V.; Oswald, F.; Nienhaus, K; Bourgeois, D.; Nienhaus, G. U. *J. Biophotonics* **2011**, *4*, 377–390.

25. Dedecker, P.; De Schryver, F. C.; Hofkens, J. *J. Am. Chem. Soc.* **2013**, *135*, 2387–2402.

26. Raymo, F. M. *ISRN Phys. Chem.* **2012**, 619251-1-15

27. Klán, P.; Šolomek, T.; Bochet, C. G.; Blanc, A.; Givens, R.; Rubina, M.; Popik, V.; Kostikov A.; Wirz, J.; *Chem. Rev.* **2013**, *113*, 119−191.

28. Lakowicz, J. R. *Principles of Fluorescence Spectroscopy*; Springer: New York, 2006.

29. Kobayashi, T.; Komatsu, T.; Kamiya, M.; Campos, C.; González-Gaitán, M.; Terai, T.; Hanaoka, K.; Nagano, T.; Urano, Y. *J. Am. Chem. Soc.* **2012**, *134*, 11153−11160.

30. (a) Zhao, Y.; Zheng, Q.; Dakin, K.; Xu, K.; Martinez, M. L.; Li, W.-H. *J. Am. Chem. Soc.* **2004**, *126*, 4653–4663. (b) Zheng, G.; Cochella, L.; Liu, J.; Hobert, O.; Li, W.-H. *ACS Chem. Biol.* **2011**, *6*, 1332–1338.

31. (a) Gagey, N.; Neveu, P.; Jullien, L. *Angew. Chem. Int. Ed.* **2007**, *46*, 2467–2469. (b) Gagey, N.; Emond, M.; Neveu, P.; Benbrahim, C.; Goetz, B.; Aujard, I.; Baudin, J.-B.; Jullien, L. *Org. Lett.* **2008**, *10*, 2341–2344.

32. Orange, C.; Specht, A.; Puliti, D.; Sakr, E.; Furuta, T.; Winsor, B.; Goeldner, M. *Chem. Commun.* **2008**, 1217–1219.

33. (a) Deniz, E.; Sortino, S.; Raymo, F. M. *J. Phys. Chem. Lett.* **2010**, *1*, 3506–3509.   (b) Deniz, E.; Tomasulo, M.; Cusido, J.; Sortino, S.; Raymo, F. M. *Langmuir* **2011**, *27*, 11773–11783. (c) Deniz, E.; Tomasulo, M.; Cusido, J.; Yildiz, I.; Petriella, M.; Bossi, M. L.; Sortino, S.; Raymo, F. M. *J. Phys. Chem. C* **2012**, *116*, 6058−6068. (d) Cusido, J.; Battal, M.; Deniz, E.; Yildiz, I.; Sortino, S.; Raymo, F. M. *Chem. Eur. J.* **2012**, *18*, 10399–10407. (e) Deniz, E.; Kandoth, N.; Fraix, A.; Cardile, V.; Graziano, A. C. E.; Lo Furno, D.; Gref, R.; Raymo, F. M.; Sortino, S. *Chem. Eur. J.* **2012**, *18*, 15782–15787. (f) Swaminathan, S.; Petriella, M.; Deniz, E.; Cusido, J.; Baker, J. D.; Bossi, M. L.; Raymo, F. M. *J. Phys. Chem. A* **2012**, *116*, 9928–9933.

34. Duan, X.-Y.; Zhai, B.-C.; Song, Q.-H. *Photochem. Photobiol. Sci.* **2012**, *11*, 593–598.

35. (a) Jeong, Y.-C.; Yang, S. I.; Ahn, K.-H.; Kim, E. *Chem. Commun.* **2005**, 2503–2505. (b) Jeong, Y.-C.; Yang, S. I.; Kim, E.; Ahn, K.-H. *Tetrahedron* **2006**, *62*, 5855–5861.

36. Uno, K.; Niikura, H.; Morimoto, M.; Ishibashi, Y.; Miyasaka, H.; Irie, M. *J. Am. Chem. Soc.* **2011**, *133*, 13558–13564.

37. (a) Lord, S. J.; Conley, N. R.; Lee, H. D.; Samuel, R.; Liu, N.; Twieg, R. J.; Moerner, W. E. *J. Am. Chem. Soc.* **2008**, *130*, 9204–9205. (b) Lord, S. J.; Conley, N. R.; Lee, H. D.; Nishimura, S. Y.; Pomerantz, A. K.; Willets, K. A.; Lu, Z.; Wang, H.; Liu, N.; Samuel, R.; Weber, R.; Semyonov, A.; He, M.; Twieg, R. J.; Moerner, W. E. *ChemPhysChem* **2009**, *10*, 55–65. (c) Lee, H. D.; Lord, S. J.; Iwanaga, S.; Zhan, K.; Xie, H.; Williams, J. C.; Wang, H.; Bowman, G. R.; Goley, E. D.; Shapiro, L.; Twieg, R. J.; Rao, J.; Moerner, E. W. *J. Am. Chem. Soc.* **2010**, *132*, 15099–15101. (d) Lord, S. J.; Lee, H. D.; Samuel, R.; Weber, R.; Liu, N.; Conley, N. R.; Thompson, M. A.; Twieg, R. J.; Moerner, W. E. *J. Phys. Chem. B* **2010**, *114*, 14157–14167.

38. Krafft, G. A.; Sutton, W. R.; Cummings, R. T. *J. Am. Chem. Soc.* **1988**, *110*, 301–303.

39. Mitchison, T. J. *J. Cell Biol.* **1989**, *109*, 637–652.

40. Vincent, J. P.; O'Farrell, P. H. *Cell* **1992**, *68*, 923–931.

41. Pellois, J.-P.; Hahn, M. E.; Muir, T. W. *J. Am. Chem. Soc.* **2004**, *126*, 7170–7171.

42. Kobayashi, T.; Urano, Y.; Kamiya, M.; Ueno, T.; Kojima, H.; Nagano, T. *J. Am. Chem. Soc.* **2007**, *129*, 6696–6697.

43. Zheng, G.; Guo, Y.-M.; Li, W.-H. *J. Am. Chem. Soc.* **2007**, *129*, 10616–10617.

44. Maurel, D.; Banala, S.; Laroche, T.; Johnsson, K. *ACS Chem. Biol.* **2010**, *5*, 507–516.

45. Yuan, L.; Lin, W.; Cao, Z.; Long, L.; Song, J. *Chem. Eur. J.* **2011**, *17*, 689–696.

46. Ottl, J.; Gabriel, D.; Marriott, G. *Bioconjugate Chem.* **1998**, *9*, 143–151.

47. Gee, K. R.; Weinberg, E. S.; Kozlowski, D. *J. Bioorg. Med. Chem. Lett.* **2001**, *11*, 2181–2183.

48. (a) Fölling, J.; Belov, V. N.; Kunetsky, R.; Medda, R.; Schönle, A.; Egner, A.; Eggeling, C.; Bossi, M.; Hell, S. W. *Angew. Chem. Int. Ed.* **2007**, *46*, 6266–6270. (b) Fölling, J.; Belov, V. N.; Riedel, D.; Schönle, A.; Egner, A.; Eggeling, C.; Bossi, M.; Hell, S. W. *ChemPhysChem* **2008**, *9*, 321–326. (c) Testa, I.; Schönle, A.; von Middendorf, C.; Geisler, C.; Medda, R.; Wurm, C. A.; Stiel, A. C.; Jakobs, S.; Bossi, M. L.; Eggeling, C.; Hell, S. W.; Egner, A. *Opt. Express* **2008**, *16*, 21093–21104. (d) Belov, V. N.; Bossi, M. L.; Fölling, J.; Boyarskiy, V. P.; Hell, S. W. *Chem. Eur. J.* **2009**, *15*, 10762–10776. (e) Belov, V. N.; Wurm, C. A.; Boyarskiy, V. P.; Jakobs S.; Hell, S. W. *Angew. Chem. Int. Ed.* **2010**, *49*,

3520–3523. (f) Kolmakov, K.; Wurm, C.; Sednev, M. V.; Bossi, M. L.; Belov, V. N.; Hell, S. W. *Photochem. Photobiol. Sci.* **2012**, *11*, 522–532. (g) Montenegro, H.; Paolo, M. D.; Capdevila, D.; Aramendía, P.F.; Bossi, M. L. *Photochem. Photobiol. Sci.* **2012**, *11*, 1081–1086.

49. Wysocki, L. M.; Grimm, J. B.; Tkachuk, A. N.; Brown, T. A.; Betzig, E.; Lavis, L. D. *Angew. Chem. Int. Ed.* **2011**, *50*, 11206–11209.

50. (a) Hu, D.; Tian, Z.; Wu, W.; Wan, W.; Li, A. D. Q. *J. Am. Chem. Soc.* **2008**, *130*, 15279–15281. (b) Tian, Z.; Li, A. D. Q.; Hu, D. *Chem. Commun.* **2011**, 1258–1260.

51. Dorion, G. H.; Wiebe, A. F.; *Photochromism*, Focal Press, New York, 1970.

52. Brown, G. H. (Ed.), *Photochromism*, Wiley, New York, 1971.

53. El'tsov, A. V. (Ed.), *Organic Photochromes*, Consultants Bureau, New York, 1990.

54. Bouas-Laurent, H.; Dürr, H. (Eds.), *Photochromism: Molecules and Systems,* Elsevier, Amsterdam, 1990.

55. Crano, J. C.; Guglielmetti, R.; (Eds.), *Organic Photochromic and Thermochromic Compounds,* Plenum Press, New York, 1999.

56. Irie, M. (Ed.), *Chem. Rev.* **2000**, *100*, 1683–1890.

57. Bassani, D.; Hofkens, J.; Pozzo, J. L. (Eds.), *Photochem. Photobiol. Sci.* **2010**, *9*, 117–264.

58. Favaro, G.; Irie, M. (Eds.), *J. Photochem. Photobiol. C* **2011**, *12*, 71–236.

59. Gust, D.; Raymo F. M. (Eds.), *Isr. J. Chem.* **2013**, *53*, 235.

60. Kuz'min, M. G.; Koz'menko, M. V.; *Organic Photochromes*, El'tsov, A. V.; (Ed.), Consultants Bureau, New York, 1990, 245–265.

61. (a) Raymo, F. M.; Tomasulo, M. *Chem. Soc. Rev.* **2005**, *34*, 327–336. (b) Raymo, F. M.; Tomasulo, M. *J. Phys. Chem. A* **2005**, *109*, 7343–7352. (c) Cusido, J.; Deniz, E.; Raymo, F. M. *Eur. J. Org. Chem.* **2009**, 2031–2045. (d) Yildiz, I.; Deniz, E.; Raymo, F. M. *Chem. Soc. Rev.* **2009**, *38*, 1859–1867. (e) Cusido, J.; Deniz, E.; Raymo, F. M. *Curr. Phys. Chem.* **2011**, *1*, 232–241.

62. Yun, C.; You, J.; Kim, J.; Huh, J.; Kim, E. *J. Photochem. Photobiol. C* **2009**, *10*, 111–129.

63. Fukaminato, T. *J. Photochem. Photobiol. C* **2011**, *12*, 177–208.

64. Ishikawa-Ankerhold, H. C.; Ankerhold, R.; Drummen, G. P. C. *Molecules* **2012**, *17*, 4047–4132.

65. (a) Theriot, J. A.; Mitchison, T. J. *Nature* **1991**, *352*, 126–131. (b) Cramer, L.; Mitchison, T. J. *J. Cell Biol.* **1993**, *122*, 833–843.

66. Rodionov, V. I.; Lim, S. S.; Gelfand, V. I.; Borisy, G. G. *J. Cell Biol.* **1994**, *126*, 1455–1464.

67. (a) Dakin, K.; Zhao, Y. R.; Li, W. H. *Nat. Methods* **2005**, *2*, 55–62. (b) Dakin, K.; Li, W. H. *Nat. Methods* **2006**, *3*, 959. (c) Guo, Y. M.; Chen, S.; Shetty, P.; Zheng, G.; Lin, R.; Li, W. H. *Nat. Methods* **2008**, *5*, 835–841.

68. Politz, J. C. R.; Tuft, R. A.; Prasanth, K. V.; Baudendistel, N.; Fogarty, K. E. ; Lifshitz, L. M.; Langowski, J.; Spector, D. L.; Pederson, T. *Mol. Biol. Cell* **2006**, *17*, 1239–1249.

69. Shestopalov, I. A.; Pitt, C. L. W.; Chen, J. K. *Nat. Chem. Biol.,* **2012**, *8*, 270–276.

70. Lempert, W. R.; Magee, K.; Ronney, P.; Gee, K. R.; Haugland, R. P. *Exp. Fluids* **1995**, *18*, 249–257.

71. (a) Guilkey, J. E.; Gee, K. R.; McMurtry, P. A.; Klewicki, J. C. *Exp. Fluids* **1996**, *21*, 237–242. (b) Guilkey, J. E.; Kerstein, A. R.; McMurtry, P. A.; Klewicki, J. C. *Phys. Fluids* **1997**, *9*, 717–723.

72. Paul, P. H.; Garguilo, M. G.; Rakestraw, D. J. *Anal. Chem.* **2000**, *70*, 2459–2467.

73. (a) Barker, S. L.; Ross, D.; Tarlov, M. J.; Gaitan, M.; Locascio, L. E. *Anal. Chem.* **2000**, *72*, 5925–5929. (b) Johnson, T. J.; Ross, D.; Gaitan, M.; Locascio, L. E. *Anal. Chem.* **2001**, *73*, 3656–3661. (c) Ross, D.; Locascio, L. E. *Anal. Chem.* **2003**, *75*, 1218–1220.

74. Shelby, J. P.; Chiu, D. T. *Anal. Chem.* **2003**, *75*, 1387–1392.

75. Rondelez, Y.; Tresset, G.; Tabata, K. V.; Arata, H.; Fujita, H.; Takeuchi, S.; Noji, H. *Nat. Biotechnol.* **2005**, *23*, 361–365.

76. Murphy, D. B. *Fundamentals of Light Microscopy and Electronic Imaging*; Wiley-Liss: New York, 2001.

77. Cusido, J.; Impellizzeri, S.; Raymo, F. M. *Nanoscale* **2011**, *3*, 59–70.

78. (a) Hell, S. W. *Nat. Biotechnol.* **2003**, *21*, 1347–1355. (b) Hell, S. W. *Science* **2007**, *316*, 1153–1158.

79. (a) Bossi, M.; Fölling, J.; Belov, V. N.; Boyarskiy, V. P.; Medda, R.; Egner, A.; Eggeling, C;. Schönle, A.; Hell, S. W. *Nano Lett.* **2008**, *8*, 2463–2468. (b) Aquino, D.; Schönle, A.; Geisler, C.; Middendorf, C. v.; Wurn, C. A.; Okamura, Y.; Lang, T.; Hell, S. W.; Egner, A. *Nat. Methods* **2011**, *8*, 353–359.

80. Juette, M. F.; Gould, T. J.; Lessard, M. D.; Mlodzianoski, M. J.; Nagpure, B. S.; Bennet, B. T.; Hess, S. T.; Bewersdorf, J. *Nat. Methods* **2008**, *5*, 527–529.

81. Pavani, S. R. P.; Thompson, M. A.; Biteen, J. S. Lord, S. J.; Liu, N.; Twieg, R. J.; Piestum, R.; Moerner, E. W. *Proc. Natl. Acad. Sci. USA* **2009**, *106*, 2995–2999.

82. Cella Zanacchi, F.; Lavagnino, Z.; Perrone Donnorso, M.; Del Bue, A.; Furia, L.; Faretta, M.; Diaspro, A. *Nat. Methods* **2011**, *8*, 1047–1049.

83. Roberti, M. J.; Fölling, F.; Celej, M. S.; Bossi, M. L.; Jovin, T. M.; Jares-Erijman, E. A. *Biophys. J.* **2012**, *102*, 1598–1607.

84. Aoki, H.; Mori, K.; Ito, S. *Soft Matter* **2012**, *8*, 4390–4395.

85. Hess, S. T.; Girirajan, T. P. K.; Mason, M. D. *Biophys. J.* **2006**, *91*, 4258–4272.

86.   Rust, M. J.; Bates, M.; Zhuang, X. *Nat. Methods* **2006**, *3*, 793–796.

87.   Betzig, E.; Patterson, G. H.; Sougrat, R.; Lindwasser, O. W.; Olenych, S.; Bonifacino, J. S.; Davidson, M. W.; Lippincott-Schwartz, J.; Hess, H. F. *Science* **2006**, *313*, 1642–1645.

88.   (a) Rust, M. J.; Bates, M.; Zhuang, *Nat. Methods* **2006**, *3*, 793–795. (b) Bates, M.; Huang, B.; Dempsey, G. T.; Zhuang, X. *Science* **2007**, *317*, 1749–1753. (c) Huang, B.; Jones, S. A.; Brandenburg, B.; Zhuang, X. *Nat. Methods* **2008**, *5*, 1047–1052. (d) Huang, B.; Wang, W.; Bates, M.; Zhuang, X. *Science* **2008**, *319*, 810–813. (e) Jones, S. A.; Shim, S.-H.; He, S.; Zhuang, X. *Nat. Methods* **2011**, *8*, 499–505. (f) Dempsey, G. T.; Vaughan, J. C.; Chen, K. H.; Bates, M.; Zhuang, X. *Nat. Methods* **2011**, *8*, 1027–1036. (g) Vaughan, J. C.; Jia, S.; Zhuang, X. W. *Nat. Methods* **2012**, *9*, 1181–1184. (h) Shim, S.-H.; Xia, C.; Zhong, G.; Babcock, H. P.; Vaughan, J. C.; Huang, B.; Wang, X.;. Xu, C.; Bi, G.-Q.; Zhuang, X. *Proc. Natl. Acad. Sci. USA* **2012**, *109*, 13978–13983.

89.   (a) Heilemann, M.; van de Linde, S.; Schüttpelz, M.; Kasper, R.; Seefeldts, B.; Mukherjee, A.; Tinnefeld, P.; Sauer, M. *Angew. Chem. Int. Ed.* **2008**, *47*, 6172–6176. (b) van de Linde, S.; Kasper, R.; Heilemann, M.; Sauer, M. *Appl. Phys. B* **2008**, *93*, 725–731. (c) van de Linde, S.; Sauer, M.; Heilemann, M. *J. Struct. Biol.* **2008**, *164*, 250–254. (d) Heilemann, M.; van de Linde, S.; Mukherjee, S.; Sauer, M. *Angew. Chem. Int. Ed.* **2009**, *48*, 6903–6908. (e) van de Linde, S.; Endesfelder, U.; Mukherjee, A.; Schüttpelz, M.; Wiebusch, G.; Wolter, S.; Heileman, M.; Sauer, M. *Photochem. Photobiol. Sci.* **2009**, *8*, 465–469. (f) Endesfelder, U.; van de Linde, S.; Wolter, S.; Sauer, M.; Heilemann, M. *ChemPhysChem* **2010**, *11*, 836–840. (g) van de Linde, S.; Wolter, S.; Heileman, M.; Sauer, M. *J. Biotechnol.* **2010**, *149*, 260–266. (h) Wolter, S.; Schuttpelz, M.; Tscherepanow, M.; van de Linde, S.; Heilemann, M.; Sauer, M. *J. Microsc.* **2010**, *237*, 12–22. (i) Wombacher, R.; Heidbreder, M.; van de Linde, S.; Sheetz, M. P.; Heileman, M.; Cornish, V. W.; Sauer, M. *Nat. Methods* **2010**, *7*, 717–719. (j) Schüttpelz, M.; Wolter, S.; van de Linde, S.; Heilemann, M.; Sauer, M. *Proc. SPIE* **2010**, *7571*, 75710V-1–7. (k) Klein, T.; Löschberger, A.; Proppert, S.; Wolter, S.; van de Linde, S.; Sauer, M. *Nat. Methods* **2011**, *8*, 7–9. (l) van de Linde, S.; Loeschberger, A.; Klein, T.; Heidbreder, M.; Wolter, S.; Heileman, M.; Sauer, M. *Nat. Protocols* **2011**, *6*, 991–1009. (m) van de Linde, S.; Krstić, I.; Prisner, T.; Doose, S.; Heilemann, M.; Sauer, M. *Photochem. Photobiol. Sci.* **2011**, *10*, 499–500.

90.   (a) Steinhauer, C.; Forthmann, C.; Vogelsang, J.; Tinnefeld, P. *J. Am. Chem. Soc.* **2008**, *130*, 16840–16841. (b) Steinhauer, C.; Jungmann, R. Sobey, T. L.; Simmel, F. C.; Tinnefeld, P. *Angew. Chem. Int. Ed.* **2009**, *48*, 8870–8873. (c) Vogelsang, J.; Cordes, T.; Forthmann, C.; Steinhauser, C; Tinnefeld, P. *Proc. Natl. Acad. Sci. USA* **2009**, *106*, 8107–8112. (d) Cordes, T.; Strackharn, M.; Stahl, S. W.; Summerer, W.; Steinhauer, C.; Forthmann, C.; Puchner, E. M.; Vogelsang, J.; Gaub, H.E.; Tinnefeld, P. *Nano Lett.* **2010**, *10*, 645–651. (e) Vogelsang, J.; Cordes, T.; Forthmann, C.; Steinhauer, C.; Tinnefeld, P. *Nano Lett.* **2010**, *10*, 672–679. (f) Cordes, T.; Maiser, A.; Steinhauser, C.; Scermelleh, L.; Tinnefeld, P. *Phys. Chem. Chem. Phys.* **2011**, *13*, 6699–6709. (g) Stein, I. H.;

Capone, S.; Smit, J. H.; Baumann, F.; Cordes, T.; Tinnefeld, P. *ChemPhysChem* **2012**, *13*, 931–937. (h) Tinnefeld, P.; Cordes, T. *Nat. Methods* **2012**, *9*, 426–427.

91. (a) Baddeley, D.; Jayasinghe, I. D.; Cremer, C.; Cannell, M. B.; Soeller, C. *Biophys. J.* **2009**, *96*, L22–L24. (b) Lemmer, R.; Gunkel, M.; Weiland, Y.; Müller, P.; Baddeley, D.; Kaufmann, R.; Urich, A.; Eipel, H.; Amberger, R.; Hausmann, M.; Cremer, C. *J. Microsc.* **2009**, *235*, 163–171. (c) Baddeley, D.; Crossman, D.; Rossberger, S.; Cheyne, J. E.; Montgomery, J. M.; Jayasinghe, I. D.; Cremer, C.; Cannell, M. B.; Soeller, C. *PLoS ONE,* **2011**, *6*, e20645-1–10.

92. (a) Flors, C.; Ravarani, C. N. J.; Dryden, D. T. F. *ChemPhysChem* **2009**, *10*, 2201–2204. (b) Flors, C. *Photochem. Photobiol. Sci.* **2010**, *9*, 643–648.

93. Neely, R. K.; Dedecker, P.; Hotta, J.; Urbanaviciute, G.; Klimasauskas, S.; Hofkens, J. *Chem. Sci.* **2010**, *1*, 453–460.

94. Schwering, M.; Kiel, A.; Kurz, A.; Lymperopoulos, A.; Sprödefeld, A.; Krämer, R.; Herten, D.-P. *Angew. Chem. Int. Ed.* **2011**, *50*, 2940–2945.

95. Shtengel, G.; Galbraith, J. A.; Galbraith, C. G.; Lippincott-Schwartz, J.; Gillette, J. M.; Manley, S.; Sougrat, R.; Waterman, C. M.; Kanchanawong, P.; Davidson, M. W.; Fetter, R. D.; Hess, H. F. *Proc. Natl. Acad. Sci. USA* **2009**, *106*, 3125–3130.

96. (a) Pavani, S. R. P.; Thompson, M. A.; Biteen, J. S.; Lord, S. J.; Liu, N.; Twieg, R. J.; Piestum, R.; Moerner, E. W.; *Proc. Natl. Acad. Sci. USA* **2009**, *106*, 2995–2999. (b) Backlund, M. P.; Lew, M. D.; Backer, A. S.; Sahl, S. J.; Grover, G.; Agrawal, A.; Piestun, R.; Moerner, W. E. *Proc. Natl. Acad. Sci. USA* **2012**, *109*, 19087–19092.

97. Pellicciioli, A. P.; Wirz, J. *Photochem. Photobiol. Sci.* **2002**, *1*, 441–458.

98. Johnson, I.; Spence, M. T. Z. *The Molecular Probes Handbook — A Guide to Fluorescent Probes and Labeling Technologies*: *11th Edition*; Life Technologies: Carlsbad, CA, 2010.

99. (a) Sauer, M. Proc. Natl. Acad. Sci. USA **2005**, 105, 9433–9434. (b) van de Linde, S.; Wolter, S.; Sauer, M. *Aust. J. Chem.* **2011**, *64*, 503–511.

100. (a) Bates, M.; Huang, B.; Zhuang, X. *Curr. Op. Chem. Biol.* 2008, 12, 505–514. (b) Huang, B.; Bates, M.; Zhuang, X. *Ann. Rev. Biochem.* **2009**, *78*, 993–1016.

101. (a) Hess, S. T.; Gould, T. J.; Gunewardene, M.; Bewersdorf, J.; Mason, M. D. *Methods Mol. Biol.* **2009**, 2009, 483–522. (b) Toomre, D.; Bewersdorf, J. *Annu. Rev. Cell Dev. Biol.* **2010**, *26*, 285–314.

102. (a) Vogelsang, J.; Steinhauer, C.; Forthmann, C.; Stein, I. H.; Person-Skergo, B.; Cordes, T.; Tinnefeld, P. *ChemPhysChem* **2010**, *11*, 2475–2490. (b) Ha, T.; Tinnefeld, P. *Ann. Rev. Phys. Chem.* **2012**, *63*, 595–617.

103. (a) Thompson, M. A.; Biteen, J. S.; Lord, S. J.; Conley, N.; Moerner, W. E., *Methods Enzymol.* **2010**, *475*, 27–59.

104. (a) Raymo, F. M.; Giordani, S. *Org. Lett.* **2001**, *3*, 3475–3478. (b) Raymo, F. M.; Alvarado, R. J.; Giordani, S.; Cejas, M. A. *J. Am. Chem. Soc.* **2003**, *125*, 2361–2364. (c) Giordani, S.; Cejas, M. A.; Raymo, F. M. *Tetrahedron* **2004**, *60*, 10973–10981. (d) Silvi, S.; Arduini, A.; Pochini, A.; Secchi, A.; Tomasulo, M.; Raymo, F. M.; Baroncini, M.; Credi, A. *J. Am. Chem. Soc.* **2007**, *129*, 13378–13379. (e) Silvi, S.; Constable, E. C.; Housecroft, C. E.; Beves, J. E.; Dunphy, E. L.; Tomasulo, M.; Raymo, F. M.; Credi, A. *Chem. Eur. J.* **2009**, *15*, 178–185. (f) Silvi, S.; Constable, E. C.; Housecroft, C. E.; Beves, J. E.; Dunphy, E. L.; Tomasulo, M.; Raymo, F. M.; Credi, A. *Chem. Commun.* **2009**, *12*, 1484–1486.

105. Houlihan, M.; Shugard, A.; Gooden, R.; Reichmanis, E. *Macromolecules* **1988**, *21*, 2001–2006.

106. The absorption spectra of **4a** in acetonitrile and PBMA do not change upon irradiation at λ_{Ac} in the absence of **8**, under otherwise identical conditions.

107. The illumination of a PBMA film doped with **4a** only does not reveal any fluorescence activation, under otherwise identical conditions.

108. Yildiz, I.; Impellizzeri, S.; Deniz, E.; McCaughan, B.; Callan, J. F.; Raymo, F. M. *J. Am. Chem. Soc.* **2011**, *133*, 871–879.

109. Hell, S.W.; Wichmann, J. *Opt.Lett.* **1994**, *19*, 780-782.

110. Fölling, J.; Bossi, M.; Bock, H.; Medda, R.; Wurm, A.; Hein, B.; Jakobs, S.; Eggeling, C.; Hell, S. W. *Nat. Methods.* **2008**, *5*, 943–945.

111. Klar, T. A.; Jakobs, S.; Dyba, M.; Egner, A.; Hell, S. W. *Proc.Natl.Sci. U. S. A.* **2000**, *97*, 8206-8210.

112. Thompson, R. E.; Larson, D. R.; Webb, W. W. *Biophys. J.* **2002**, *82*, 2775-2783.

113. Heilemann, M.; Dedecker, P.; Hofkens, J.; Sauer, M. *Laser & Photon Rev.* **2009**, *3*, 180–202.

114. Andresen, M.; Stiel, A. C.; Fölling, J.; Wenzel, D.; Schönle, A.; Egner, A.; Eggeling, C.; Hell, S. W.; Jakobs, S. *Nature Biotech.* **2008**, *26*, 1035–1040.

115. Zhang, L. W.; Monteiro-Riviere, N. A. *Toxicol. Sci.* **2009**, *110*, 138–155.

116. Feringa, B.L.; Browne, W. R. (Eds.) *Molecular Switches,* Wiley-VCH: Weinheim, 2011.

117. Balzani, V.; Venturi, M.; Credi, A. *Molecular Devices and Machines: Concepts and Perspectives for the Nanoworld,* Wiley-VCH: Weinheim, 2008.

118. Matsuda, K.; Irie, M. *J. Photochem. Photobiol. C* **2004**, *5*, 169–182.

119. Tian, H.; Yang, S. J. *Chem. Soc. Rev.* **2004**, *33*, 85–97.

120. Gust, D.; Moore, T. A.; Moore, A. L. *Chem. Commun.* **2006**, 1169–1178.

121. (a) Raymo, F. M. *Angew. Chem. Int. Ed.* **2006**, *45*, 5249–5251. (b) Raymo, F. M.; Tomasulo, M. *Chem. Eur. J.* **2006**, *12*, 3186–3193.

122. Tomasulo, M.; Sortino, S.; Raymo, F. M. *Org. Lett.* **2005**, *7*, 1109–1112.

123. Tomasulo, M.; Sortino, S.; White, A. J. P.; Raymo, F. M. *J. Org. Chem.* **2005**, *70*, 8180–8189.

124. Steudel, E.; Posdorfer, J.; Schindler, R. N. *Electrochimica Acta,* **1995**, *40,* 1587-1594.

125. Núñez-Vergara, L. J.; Squella, J. A.; Olea-Azar, C.; Bollo, S.; Navarrete-Encina, P. A.; Sturm, J. C.; *Electrochimica Acta,* **2000**, *45,* 3555-3561.

126. Smith, W. H.; Bard, A. J. *J. Am. Chem. Soc.* **1975**, *97*, 5203−5210.

127. Armstrong, N. R.; Quinn, R. K.; Vanderborgh, N. E.; *Anal. Chem.* **1974**, 46, 1759-1764.

128. (a) Loudet, A.; Burgess, K. *Chem. Rev.* **2007**, *107*, 4891−4932. (b) Kamkaew, A.; Lim, S. H.; Lee, H. B.; Kiew, L. V.; Chung L. Y.; Burgess, K. *Chem. Soc. Rev.* **2013**, *42*, 77–88.

129. (a) Ziessel, R.; Ulrich, G.; Harriman, A. *New J. Chem.* **2007**, *31*, 496–501. (b) Ulrich, G.; Ziessel, R.; Harriman, A. *Angew. Chem. Int. Ed.* **2008**, *47*, 1184–1201.

130. Benstead, M.; Mehl, G.; H.; Boyle, R. W. *Tetrahedron* **2011**, *67*, 3573–3601.

131. Nepomnyashchii, A. B.; Bard, A. J. *Acc. Chem. Res.* **2012**, *45*, 1844–1853.

132. Boens, N.; Leen, V.; Dehaen, W. *Chem. Soc. Rev.* **2012**, *41*, 1130–1172.

133. (a) Ulrich, G.; Ziessel, R. *J. Org. Chem.* **2004**, *69*, 2070–2083. (b) Harriman, A.; Mallon, L. J.; Ulrich, G.; Ziessel, R. *ChemPhysChem* **2007**, *8*, 1207–1214. (c) Alamiry, M. A. H.; Harriman, A.; Mallon, L. J.; Ulrich, G.; Ziessel, R. *Eur. J. Org. Chem.* **2008**, *16*, 2774–2782.

134. Wang, D.; Miyamoto, R.; Shiraishi, Y.; Hirai, T. *Langmuir* **2009**, *25*, 13176–13182.

135. Exposure of a solution of **20** to ambient light does not result in any detectable change in fluorescence even after 48 hours.

136. The fluorescene quantum yield of **19** does not change in the presence of one equivalent of tetrabutylammonium hydroxide.

137. Scaiano, J. C. *Handbook of Organic Photochemistry*; CRC Press: Florida, 1989.

138. Shaban Ragab, S.; Swaminathan, S.; Baker, J. D.; Raymo, F. M. *Phys. Chem. Chem. Phys.* **2013**, *15*, 14851-14855.

139. Deniz, E.; Battal, M.; Cusido, J.; Sortino, S.; Raymo, F. M. *Phys. Chem. Chem. Phys.* **2012**, *14*, 10300–10307.

140. Tahtaoui, C.; Thomas, C.; Rohmer, F.; Klotz, P.; Duportail, G.; Mely, Y.; Bonnet, D.; Hibert, M. *J. Org. Chem.* **2007**, *72*, 269–272.

141. Lundrigan, T.; Crawford, S. M.; Cameron, T. S.; Thompson, A. *Chem. Commun.* **2012**, *48*, 1003–1005.

142. Gabe, Y.; Urano, Y.; Kikuchi, K.; Kojima, H.; Nagano, T. *J. Am. Chem. Soc.* **2004**, *126*, 3357–3367.

143. TDDFT calculations are known to overestimate the excitation energy of BODIPY chromophores (Nithya, R.; Kolandaivel, P.; Senthilkumar, K. *Mol. Phys.* **2012**, *110*, 445–456). In fact, the absorption spectra of **24** and **25** (Figures 6.3 and 6.4) indicate the excitation energy to be ca. 2.4 eV for both compounds. This experimental value is ca. 0.3 eV lower than those calculated for **24** and **25** (Table 6.3) with the B3LYP and MPW1PW91 functionals at the 6-311+G(d,p) level.

144. The addition of TFA has negligible influence on the absorption spectrum in methanol as well as in acetonitrile.

145. (a) Lehn, J.-M. *Proc. Natl. Acad. Sci. U.S.A.* **2002**, *99*, 4763–4768. (b) Lehn, J.-M. *Science* **2002**, *295*, 2400–2403.

146. (a) Lehn, J.-M. *Chem. Eur. J.* **1999**, *5*, 2455–2463. (b) Lehn, J.-M. *Chem. Eur. J.* **2000**, *12*, 2097–2102. (c) Lehn, J.-M. *Chem. Soc. Rev.* **2007**, *36*, 151–160. (d) Lehn, J.-M. *Top. Curr. Chem.* **2012**, *322*, 1–32. (e) Lehn, J.-M. *Angew. Chem. Int. Ed.* **2013**, *52*, 2836–2850.

147. (a) Rowan, S. J.; Cantrill, S. J.; Cousins, G. R. L.; Sanders, J. K. M.; Stoddart, J. F. *Angew. Chem. Int. Ed.* **2002**, *41*, 899–958. (b) Belowich, M.; Stoddart, J. F. *Chem. Soc. Rev.* **2012**, *41*, 2003–2024. (c) Stoddart, J. F. *Angew. Chem. Int. Ed.* **2012**, *51*, 12902–12903.

148. Cheeseman, J. D.; Corbett, A. D.; Gleason, J. L.; Kazlauskas, R. J. *Chem. Eur. J.* **2005**, *11*, 1708–1716.

149. (a) Corbett, P. T.; Leclaire, J.; Vial, L.; West, K. R.; Wietor, J.-L.; Sanders, J. K. M.; Otto, S. *Chem. Rev.* **2006**, *106*, 3652–3711. (b) Cougnon, F. B. L.; Sanders, J. K. M. *Acc. Chem. Res.* **2012**, *45*, 2211–2221.

150. Ladame, S. *Org. Biomol. Chem.* **2008**, *6*, 219–226.

151. (a) Halperin, A.; Tirrell, M.; Lodge, T. P. *Adv. Polym. Sci.* **1992**, *100*, 31–71. (b) Lodge, T. P. *Macromol. Chem. Phys.* **2003**, *204*, 265–273. (c) Moughton, A. O.; Hillmyer, M. A.; Lodge, T. P. *Macromolecules* **2012**, *45*, 2–19.

152. (a) Moffitt, M.; Khougaz, K.; Eisenberg, A. *Acc. Chem. Res.* **1996**, *29*, 95–102. (b) Cameron, N. S.; Corbierre, K. M.; Eisenberg, A. *Can. J. Chem.* **1999**, *77*, 1311–1326.

153. Webber, S. E. *J. Phys. Chem. B* **1998**, *102*, 2618–2626.

154. Riess, G. *Prog. Polym. Sci.* **2003**, *28*, 1107–1170.

155. Okhapkin, I. M.; Makhaeva, E. E.; Khokhlov, A. R. *Adv. Polym. Sci.* **2006**, *195*, 177–210.

156. Kale, T. S.; Klaikherd, A.; Popere, B.; Thayumanavan, S. *Langmuir* **2009**, *25*, 9660−9670.

157. Owen, S. C.; Chan, D. P. Y.; Shoichet, M. S. *Nano Today* **2012**, *7*, 53–65.

158. Bader, H.; Ringsdorf, H.; Schmidt, B. *Angew. Makromol. Chem.* **1984**, *123*, 457–485.

159. Kataoka, K.; Kwon, G. S.; Yokoyama, M.; Okano, T.; Sakurai, Y. *J. Control Release* **1993**, *24*, 119–132.

160. Jones, M.-C.; Leroux, J.-C. *Eur. J. Pharm. Biopharm.* **1999**, *48*, 101–111.

161. Torchilin, V. P. *J. Control Release* **2001**, *73*, 137–172.

162. Adams, M. L.; Lavasanifar, A.; Kwon, G. S. *J. Pharm. Sci.* **2003**, *92*, 1343–1355.

163. Husseini, A. G.; Pitt, W. G. *Adv. Drug Deliv. Rev.* **2008**, *60*, 1137–1152.

164. Mondon, K.; Gurny, R.; Moller, M. *Chimia* **2008**, *62*, 832–840.

165. Park, J. H.; Lee, S.; Kim, J. H.; Park, K.; Kim, K.; Kwon, I. C. *Prog. Polym. Sci.* **2008**, *33*, 113–137.

166. Kim, S.; Shi, Y.; Kim, J. Y.; Park, K.; Cheng, J.-X. *Expert Opin. Drug. Deliv.* **2010**, *7*, 49–62.

167. Nicolas, J.; Mura, S.; Brambilla, D.; Mackiewicz, N.; Couvreur, P. *Chem. Soc. Rev.* **2013**, *42*, 1147–1235.

168. Swaminathan, S.; Garcia-Amorós, J.; Fraix, A.; Kandoth, N.; Sortino, S.; Raymo, F. M. *Chem. Soc. Rev.* **2014**, *43*, 4167-4178.

169. (a) Yoo, S. I.; An, S. J.; Choi, G. H.; Kim, K. S.; Yi, G.-C.; Zin, W.-C.; Jung, J. C.; Sohn, B.-H. *Adv. Mater.* **2007**, *19*, 1594–1596. (b) Yoo, S. I.; Lee, J.-H.; Sohn, B.-H.; Eom, I.; Joo, T.; An, S. J.; Yi, G.-C. *Adv. Funct. Mater.* **2008**, *18*, 2984–2989.

170. Wu, W.-C.; Chen, C.-Y.; Tian, Y.; Jang, S.-H.; Hong, Y.; Liu, Y.; Hu, R.; Tang, B. Z.; Lee, Y.-T.; Chen, C.-T.; Chen, W.-C.; Jen, A. K.-Y. *Adv. Funct. Mater.* **2010**, *29*, 1413–1423.

171. Wang, R.; Peng, J.; Qiu, F.; Yang, Y. *Chem. Commun.* **2011**, *47*, 2787–2789.

172. Wagh, A.; Qian, S. Y.; Law, B. *Bioconjugate Chem.* **2012**, *23*, 981–992.

173. (a) Cao, T.; Munk, P.; Ramireddy, C.; Tuzar, Z.; Webber, S. E. *Macromolecules* **1991**, *24*, 6300–6305. (b) Stepanek, M.; Krijtova, K.; Prochazka, K.; Teng, Y.; Webber, S. E.; Munk, P. *Acta Polym.* **1998**, *49*, 96–102.

174. Hu, Y.; Kramer, M. C.; Boudreaux, C. J.; McCormick, C. L. *Macromolecules* **1995**, *28*, 7100–7106.

175. (a) Chen, H.; Kim, S.; He, W.; Wang, H.; Low, P. S.; Park, K.; Cheng, J. X. *Langmuir* **2008**, *24*, 5213−5217. (b) Chen, H. T.; Kim, S. W.; Li, L.; Wang, S. Y.; Park, K.; Cheng, J. X. *Proc. Natl. Acad. Sci. USA* **2008**, *105*, 6596–6601. (c) Lee, S.-Y.; Tyler, J. Y.; Kim, S.; Park, K.; Cheng, J.-X. *Mol. Pharmaceutics* **2013**, *10*, 3497−3506.

176. Njikang, G. N.; Gauthier, M.; Li, J. M. *Polymer* **2008**, *49*, 5474−5481.

177. (a) Jiwpanich, S.; Ryu, J. H.; Bickerton, S.; Thayumanavan, S. *J. Am. Chem. Soc.*

2010, *132*, 10683−10685. (b) Ryu, J. H.; Chacko, R. T.; Jiwpanich, S.; Bickerton, S.; Babu, R. P.; Thayumanavan, S. *J. Am. Chem. Soc.* **2010**, *132*, 17227−17235. (c) Bickerton, S.; Jiwpanich, S.; Thayumanavan, S. *Mol. Pharmaceutics* **2012**, *9*, 3569−3578.

178.   Chen, K. J.; Chiu, Y. L.; Chen, Y. M.; Ho, Y. C.; Sung, H. W. *Biomaterials* **2011**, *32*, 2586–2592.

179.   Lu, J.; Owen, S. C.; Shoichet, M. S. *Macromolecules* **2011**, *44*, 6002–6008.

180.   Hua, P.; Tirelli, N. *React. Funct. Polym.* **2011**, *71*, 303–314.

181.   McDonald, T. O.; Martin, P.; Patterson, J. P.; Smith, D.; Giardiello, M.; Marcello, M.; See, V.; O'Reilly, R. K.; Owen, A.; Rannard, S. *Adv. Funct. Mater.* **2012**, *22*, 2469–2478.

182.   (a) Li, Y. P.; Budamagunta, M. S.; Luo, J. T.; Xiao, W. W.; Voss, J. C.; Lam, K. S. *ACS Nano* **2012**, *6*, 9485–9495. (b) Li, Y. P.; Xiao, W. W.; Xiao, K.; Berti, L.; Luo, J. T.; Tseng, H. P.; Fung, G.; Lam, K. S. *Angew. Chem. Int. Ed.* **2012**, *51*, 2864–2869.

183.   Javali, N. M.; Raj, A.; Saraf, P.; Li, X.; Jasti, B. *Pharm. Res.* **2012**, *29*, 3347–3361.

184.   Klymchenko, A. S.; Roger, E.; Anton, N.; Anton, H.; Shulov, I.; Vermot, J.; Mely, Y.; Vandamme, T. F. *RSC Advances* **2012**, *2*, 11876–11886.

185.   The ^{1}H NMR spectrum (400 MHz, CDCl$_3$) of **10** indicates the ratio between the hydrophobic and hydrophilic segments to be 2.5. This value was estimated from the integrals of the resonances associated with the methyl protons at the termini of the decyl and oligo(ethylene glycol) chains.

186.   The amphiphilic character of the polymer controls its ability to form nanostructured particles. As a result, the ratio between its hydrophilic and hydrophobic segments (see ref 175) can, presumably, affect the hydrodynamic diameter of the nanoparticles as well as the critical polymer concentration required for their assembly.

187.   The overlap integral (*J*) and Förster distance (R_0) were calculated with equations (3) and (4) respectively (Lakowicz, J. R. *Principles of Fluorescence Spectroscopy*; Springer: New York, 2006). The emission intensity (I_D) of the anthracene donor and the molar extinction coefficient (ε_A) of the BODIPY acceptor at a given wavelength (λ) were determined from the corresponding emission and absorption spectra respectively (*c* and *b* in Figure 7.1). The orientation factor (κ^2), fluorescence quantum yield (ϕ_D) of the donor and refractive index (*n*) of the solvent are 2/3, 0.61 and 1.33 respectively.

$$J = \frac{\int_0^\infty I_D \varepsilon_A \lambda^4 \, d\lambda}{\int_0^\infty I_D \, d\lambda} \qquad\qquad (3)$$

$$R_0 = \sqrt[6]{\frac{9000\ (\ln 10)\ \kappa^2 \phi_{\mathrm{D}} J}{128 \pi^5 N n^4}} \qquad (4)$$

188. Fluorescence images (*a–c* in Figure 7.13), recorded after incubation of the cells with the two sets of nanoparticles and Hoechst 33342, clearly show that the nanocarriers do not co-localize with this particular dye in the nucleus.

189. The emission intensities of the bars in Figure 7.8 are reported relative to that of an indocyanine green standard. This compound was added to the cells 30 min prior to termination of incubation with the nanoparticles and its fluorescence was recorded between 780 and 800 nm with excitation at 628 nm. The corresponding images are shown in the Figures 7.14–7.16 (*a–d*).

190. Sahay, G.; Batrakova, E. V.; Kabanov, A. V. *Bioconjug. Chem.* **2008**, *19*, 2023–2029.

191. Sakai-Kato, K.; Un, K.; Nanjo, K.; Nishiyama, N.; Kusuhara, H.; Kataoka, K.; Kawanishi, T.; Goda, Y.; Okud, H. *Biomaterials* **2014**, *35*, 1347–1358.

192. Rejman, J.; Bragonzi, A.; Conese, M. *Mol. Ther.* **2005**, *12*, 468–474.

193. Wu, J.-S.; Liu, W.-M.; Zhuang, X.-Q.; Wang, F.;Wang, P.-F.; Tao, S.-L.; Zhang, X.-H.; Wu, S.-K.; Lee, S.-T. *Org. Lett.* **2007**, *9*, 33−36

194. Apex2 Version 2.2-0 and SAINT+ Version 7.46A; Bruker Analytical X-ray System, Inc., Madison, Wisconsin, USA, 2007.

195. (a) Sheldrick, G. M. SHELXTL Version 6.1; Bruker Analytical X-ray Systems, Inc., Madison, Wisconsin, USA, 2000. (b) Sheldrick, G. M. *Acta Cryst.* **2008**, *A64*, 112–122.

196. Becke, A. D. *Phys. Rev. A* **1988**, *38*, 3098–3100.

197. Lee, C.; Yang, W.; Parr, R. G. *Phys. Rev. B* **1988**, *37*, 785–789.

198. Perdew, J. P.; Chevary, J. A.; Vosko, S. H.; Jackson, K. A.; Pederson, M. R.; Singh, D. J.;Fiolhais, C. *Phys. Rev. B* **1992**, *46*, 6671–6687.

199. Adamo, C.; Barone, V. *J. Chem. Phys.* **1998**, *108*, 664–675.

200. Gaussian 09, Revision A.02, Frisch, M. J.; Trucks, G. W.; Schlegel, H. B.; Scuseria, G. E.; Robb,M. A.; Cheeseman, J. R.; Scalmani, G.; Barone, V.; Mennucci, B.; Petersson, G. A.; Nakatsuji, H.; Caricato, M.; Li, X.; Hratchian, H. P.; Izmaylov, A. F.; Bloino, J.; Zheng, G.; Sonnenberg,J.L.; Hada, M.; Ehara, M.; Toyota, K.; Fukuda, R.; Hasegawa, J.; Ishida, M.; Nakajima, T.; Honda, Y.; Kitao, O.; Nakai, H.; Vreven, T.; Montgomery, Jr., J. A.; Peralta, J. E.; Ogliaro, F.; Bearpark, M.; Heyd, J. J.; Brothers, E.; Kudin, K. N.; Staroverov, V. N.; Kobayashi, R.; Normand, J.; Raghavachari, K.; Rendell, A.; Burant, J. C.; Iyengar, S. S.; Tomasi, J.; Cossi, M.; Rega, N.; Millam, J. M.; Klene, M.; Knox, J. E.; Cross, J. B.; Bakken, V.; Adamo, C.; Jaramillo, J.; Gomperts, R.; Stratmann, R. E.; Yazyev, O.; Austin, A. J.; Cammi, R.; Pomelli, C.; Ochterski, J. W.; Martin, R. L.; Morokuma, K.; Zakrzewski, V. G.; Voth, G. A.; Salvador, P.;

Dannenberg, J. J.; Dapprich, S.; Daniels, A. D.; Farkas, Ö.; Foresman, J. B.; Ortiz, J. V.; Cioslowski, J.; Fox, D. J. Gaussian, Inc., Wallingford CT, 2009.

201. Tomasi, J.; Mennucci, B.; Cammi, R. *Chem. Rev.* **2005**, *105*, 2999–3093.

202. Egner, A.; Geisler, C.; von Middendorf, C.; Bock, H.; Wenzel, D.; Medda, R.; Andresen, M.; Stiel, A. C.; Jakobs, S.; Eggeling, C. *et al. Biophys. J.* **2007**, *93*, 3285–3290.